A PRELIMINARY STUDY TO ASSESS MODEL UNCERTAINTIES IN FLUID FLOWS

A Thesis

by

MARC OLIVIER DELCHINI

Submitted to the Office of Graduate Studies of
Texas A&M University
in partial fulfillment of the requirements for the degree of

MASTER OF SCIENCE

May 2010

Major Subject: Nuclear Engineering

A PRELIMINARY STUDY TO ASSESS MODEL UNCERTAINTIES IN FLUID FLOWS

A Thesis

by

MARC OLIVIER DELCHINI

Submitted to the Office of Graduate Studies of
Texas A&M University
in partial fulfillment of the requirements for the degree of

MASTER OF SCIENCE

Approved by:

Chair of Committee,	Jean C. Ragusa
Committee Members,	Jim E. Morel
	Victor Ugaz
	Vincent Mousseau
Head of Department,	Raymond J. Juzaitis

May 2010

Major Subject: Nuclear Engineering

ABSTRACT

A Preliminary Study to Assess

Model Uncertainties in Fluid Flows. (May 2010)

Marc Olivier Delchini, M.S., National School of Physics of Grenoble

Chair of Advisory Committee: Dr. Jean C. Ragusa

In this study, the impact of various flow models is assessed under free and forced convection: compressible versus incompressible models for a Pressurized Water Reactor, and Darcy's law vs full momentum equation for High Temperature Gas Reactor. Euler equations with friction forces and a momentum and energy source/sink are used. The geometric model consists of a one-dimensional rectangular loop system. The fluid is heated up and cooled down along the vertical legs. A pressurizer and a pump are included along the horizontal legs. The compressible model is assumed to be the most accurate model in this study.

Simulations show that under forced convection compressible and incompressible models yield the same transient and steady-state. As free convection is studied, compressible and incompressible models have different transient but the same final steady-state. As Darcy's law is used, pressure and velocity steady-state profiles yield some differences compared to the compressible model both under free and forced convections. It is also noted some differences in the transient.

To My Family

ACKNOWLEDGMENTS

I would like to thank my committee chair, Dr. Ragusa, and my mentor at Idaho National Laboratory, Dr. Mousseau, for their guidance and support throughout the course of this research.

Thanks also to my friends and colleagues and the department faculty and staff for making my time at Texas A&M University a great experience.

Finally thanks to my mother and father for their encouragement.

TABLE OF CONTENTS

CHAPTER Page

CHAPTER Page

LIST OF TABLES

LIST OF FIGURES

FIGURE Page

FIGURE Page

CHAPTER I

INTRODUCTION

The goal of this study is to assess the impact of various flow models for a simplified primary coolant loop of a light water nuclear reactor. The various fluid flow models are based on the Euler equations with an additional friction term, a gravity term, a momentum source, and an energy source. The geometric model is purposefully chosen simple and consists of a one-dimensional (1D) loop system in order to focus the study on the validity of various fluid flow approximations. The 1D loop system is represented by a rectangle; the fluid is heated up along one of the vertical legs and cooled down along the opposite leg. A pressurizer and a pump are included in the horizontal legs. The amount of energy transferred and removed from the system is equal in absolute value along the two vertical legs. The various fluid flow approximations to be studied are compressible vs. incompressible, and complete momentum equation vs. Darcy's approximation. The ultimate goal is to compute the fluid flow models' uncertainties and, if possible, to generate validity ranges for these models when applied to reactor analysis. We also limit this study to single phase flows with low-Mach numbers. As a result, sound waves carry a very small amount of energy in this particular case. A standard finite volume method is used for the spatial discretization of the system, and Backward Euler (BE) is used for time stepping.

The journal model is *Nuclear Science and Engineering*.

CHAPTER II

SOME EXAMPLES OF PRIOR WORK RELATED TO FLUID MODEL COMPARISON

Several models have been developed to simulate fluid flows at low Mach numbers in reactors. Some are more intricate than others. For instance, compressible and incompressible models are two models commonly used. A question raises from this state: how complex should a model be in order to obtain an accurate numerical solution? Comparative studies were performed in the past to analyze the output quantities of interest between physical models by comparing numerical solutions from different codes. For instance, such analysis was done for compressible and incompressible flows in the case of Nitrogen by using a 3D continuum model [1]. In this study, the numerical solution of a compressible solver ($PCICE - FEM$ [2], [3], [4]) and an incompressible ($STAR - CCM+$) solver were compared to available experimental and numerical results. Since two different codes are employed, the numerical solution algorithm is not identical nor are the meshes. It is mentioned that the mesh is refined enough in order to obtain an accurate numerical solution. However, the models solved are obviously different in their assumptions and approximations. From this study, a range of validity is deducted as a function of the hydraulic diameter and the pressure ratio (ratio of the pressure to the critical pressure). For instance, the incompressible model is no longer accurate as the hydraulic diameter is smaller than $60\mu m$.

Some studies were also performed related to the Boussinesq approximation in order to test its accuracy under stratified compressible flows for the compressible and incompressible models [5]. It is shown that by adding some anealistic continuity equations to the Boussinesq approximation in some given cases, numerical solutions

and experimental data match within a good tolerance.

A comparative study was carried out on weakly compressible and incompressible flows in [6]. An incompressible flow code is used and some compressible considerations are incorporated in order to study their effect. The conclusion of this study is that a Taylor-Galerkin/pressure correction algorithm is required to accommodate incompressible and weakly compressible flows.

All of these studies show that simpler models such as the incompressible model can be used under some conditions or by adding correcting terms. A range of validity can be generated in order to give a guideline for some future studies.

In this work, we propose to analyze the measurable output quantities of interest between two models by strictly using the same solution algorithm. In this case, the numerical solver and the mesh will be the same. It is then possible to analyze the output quantities and determine a range of validity, for instance where the compressible and incompressible models can be used without any distinction.

CHAPTER III

GEOMETRICAL AND MATHEMATICAL MODELS

The test-bed code developed in this work aims at studying the primary cooling of a nuclear reactor, either a Pressurized Water Reactor, or a Hight Temperature Gas Reactor. Some simplifying assumptions are made: 1D geometry and single-phase low-Mach flow. Within this model, various fluid flows approximations are assessed. We present here the geometry utilized, the assumptions made, the various flow approximations, and the numerics employed to solve in space/time the equations obtained.

A. Model geometry

The 1D loop system is represented by a rectangle, shown in Fig. III-1. The fluid is heated up along the left vertical legs of length L_1 and cooled down along the opposite leg. The cooling process is to mimic the presence of steam generators. A pressurizer is present on the top horizontal length of length L_2 and a pump is included in the lower horizontal leg. These two components are smeared over a certain portion of the leg length in order to avoid making the pressurizer and the pump action grid size dependent.

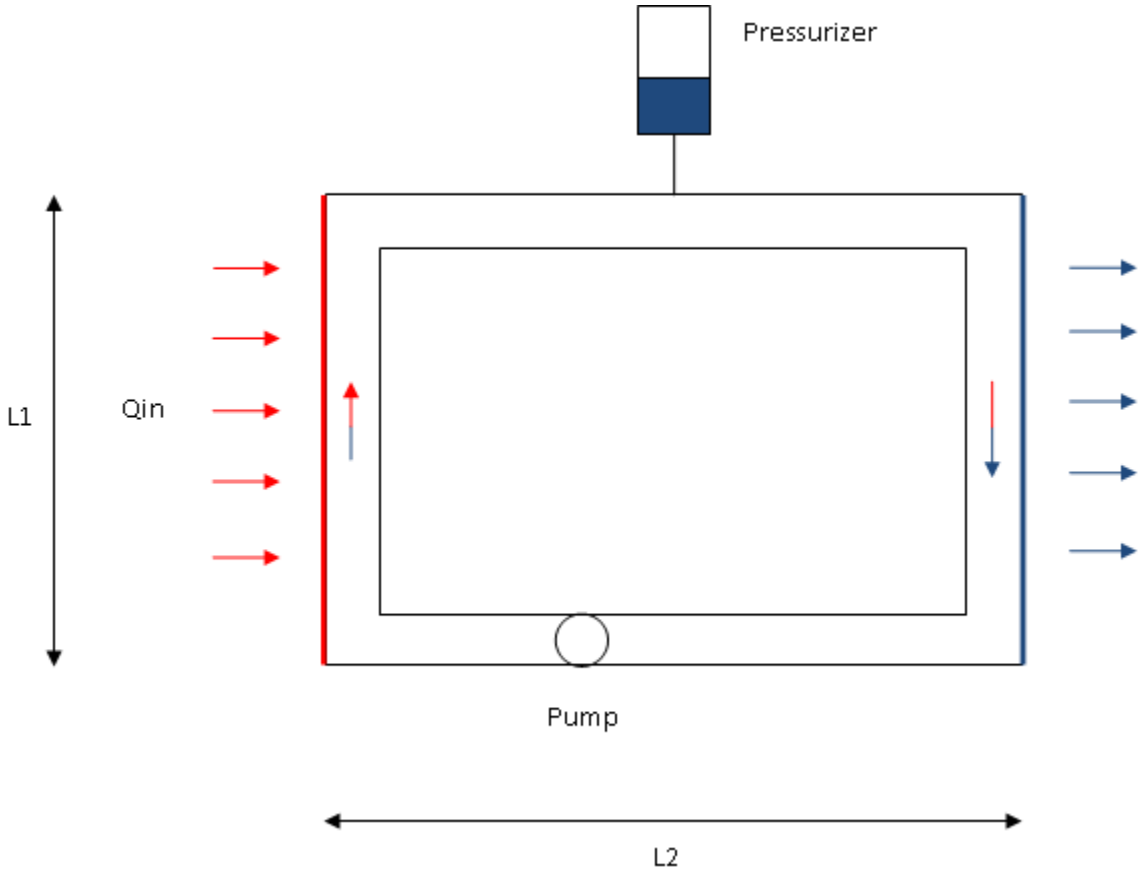

Fig. III-1. The 1D loop geometry.

B. Assumptions

The following assumptions are made for this 1D model and are detailed in this section:

- The heat source and sink are expressed in term of the heat transfer coefficient and the fluid temperature as follows:

$$Q = \pm hA(T_w - T_f), \tag{3.1}$$

where h is the heat transfer coefficient, A is the exchange area between the wall and the fluid and is a given, and, T_f and T_w are the fluid and wall temperature,

respectively. In the left vertical leg, this source term is positive (heat is applied) and in the opposite leg, it is negative (heat sink). Heat and sink source terms are distributed over the entire length L_1 of these two legs.

- The heat transfer coefficient h is constant and is taken to be the same for forced convection and natural convection processes. In practice, two different correlations should be employed since the physics are different in these two cases. T_w is a given constant equal to T_{wcore} in the heated leg, and equal to T_{wsg} in the cooled leg, where T_{wcore} and T_{wsg} are reactor-dependent.

- The heat capacity C_v is temperature- and pressure-independent. This is a good assumption for some fluids, such as water, for a range of temperature and pressure. For other coolants, such as gas, this approximation is not representative of the real behavior of the fluid.

- The sound speed, c, is assumed to be constant even if it usually depends on the temperature and the pressure. This is a good approximation for liquids but not for gases. The sound speed is reactor-dependent.

- The Equation Of State (EOS) is linear in temperature and pressure as follows:

$$\rho = \rho_0 + \left.\frac{\partial \rho}{\partial P}\right|_0 (P - P_0) + \left.\frac{\partial \rho}{\partial T}\right|_0 (T - T_0)\,, \tag{3.2}$$

  where ρ, T and P are the density, the temperature and the pressure of the fluid, respectively, and ρ_0, T_0 and P_0 are the fluid proprieties at a particular reference point (the linearization point). $\frac{\partial \rho}{\partial P}$ and $\frac{\partial \rho}{\partial T}$ are defined as the variation of the density relative to the pressure and the temperature, respectively.

  - $\frac{\partial \rho}{\partial T}$ is the dilatation of the density due to the temperature. This parameter is assumed constant in this model.

  - $\frac{\partial \rho}{\partial P}$ is the dilatation of the density due to the pressure. This parameter is also assumed constant but is different for different sound speeds. Its expression is as follows:

$$\frac{\partial \rho}{\partial P} = \frac{1}{c^2} \tag{3.3}$$

- Friction forces are taken account into this model. The wall friction parameter, f_w, is a function of the Reynolds number and depend on the laminar vs turbulent nature of the flow. Its expression is given in a subsequent section.

Different flow models are implemented:

1. compressible flow,
2. incompressible flow with Boussinesq correction,
3. Darcy's law in the compressible setting.

A solution algorithm (and thus a single code) is written, where binary (0/1) parameter values are changed in the discretized equations themselves to turn on or off any of these three flow models seamlessly. Section C gives the equations used and the different approximations related to each model.

1. Compressible and incompressible flows

A flow is defined as compressible when its density can change with respect to pressure. In general, this is the case when the Mach number of the flow exceeds 0.3. To account of the pressure effect, a linearized Equation Of State (EOS) is used and defined as follows:

$$\rho(P,T) = \rho_0(P_0,T_0) + \left.\frac{\partial \rho}{\partial P}\right|_0 (P - P_0) + \left.\frac{\partial \rho}{\partial T}\right|_0 (T - T_0), \tag{3.4}$$

where $\rho(P,T)$ is the density function of the pressure P and temperature T, $\frac{\partial \rho}{\partial P}$ is defined as the inverse of the sound speed square in the fluid (see Eq. (3.3)), P_0 and T_0

are the pressure and temperature at the point of linearization respectively and $\frac{\partial \rho}{\partial T}$ is the change in density due to the temperature. In this study, the parameter $\frac{\partial \rho}{\partial P}$ is held constant for a given fluid. This EOS is derived from a Taylor series development at the point of pressure P_0 and is a good approximation since there is no phase change in our model.

In the case of incompressible flows, the term $\frac{\partial \rho}{\partial P}$ is equal to zero, which is equivalent to setting the sound speed to infinity. In other terms, the sound waves travel through the entire domain with an infinite velocity and the density is constant and equals to ρ_0. It has to be noted that a change in temperature can lead to changes in the density. The Boussinesq correction accounts for this effect and is described next.

2. Boussinesq correction

For non-isothermal fluids, density can vary with temperature. The Boussinesq correction can be employed to allow the density to be temperature-dependent. This assumption is necessary to account for buoyancy forces.

$$\rho(T) = \rho_0(T_0) + \left.\frac{\partial \rho}{\partial T}\right|_0 (T - T_0), \tag{3.5}$$

where $\rho(T)$ is a temperature-dependent density function, ρ_0 is the density value at the temperature T_0, $\frac{\partial \rho}{\partial T}$ is the changes in density due to the temperature (this value is generally negative), and T_0 is the temperature value at the linearization point. Variations of density with respect to temperature are very important because they give rise to buoyancy forces and, thus, to natural convection.

To summarize, in the case of *compressible* flow, the EOS is modified as follows:

$$\rho(P,T) = \rho_0(P_0,T_0) + \left.\frac{\partial \rho}{\partial P}\right|_0 (P - P_0) + \left.\frac{\partial \rho}{\partial T}\right|_0 (T - T_0). \tag{3.6}$$

Compressible flows will always be treated employing Eq. (3.6) and, hence, density is both pressure- and temperature-dependent.

For *incompressible* flows, the pressure-dependent term of the EOS is removed and thus the density is only temperature-dependent. Two incompressible cases are distinguished according to their speed:

1. In the case of low speed flows, the density can only be temperature-dependent in the buoyancy term of the momentum equation (denoted by the use of $\hat{\rho}$ in later sections) and is held constant in all other terms of the mass, momentum, and energy equations. The essence of the Boussinesq correction is that gravity is sufficiently strong to make the fluid specific weight appreciably different between two fluid positions. In this case, the acceleration term $\frac{Dv}{Dt}$ is small when compared to the gravity term. This case is the purpose of this study.

2. In the case of high speed flows, the density has to be computed with the EOS in all terms of the momentum equation. The acceleration term can be large enough to compensate for the gravity effects.

In the case of our study (low Mach number), the Boussinesq correction is used in order to account for buoyancy forces in the momentum equation only.

C. Fluid flow equations with wall friction, gravity, pump and external energy source terms

Modified Euler Equations, coupled with an equation of state relation, are employed to solve the 1D loop system described above. The Euler equations are used as a starting point and are modified in the sense that (1) the effect of viscosity has been added and modeled as wall friction, and, (2) gravity is accounted for. Friction forces and gravity forces are the only external forces considered. An energy source term, denoted by

Q, is also present in the energy equation to model the heat source/sink due to the nuclear core/steam generator, respectively. In order to account for the pump in the model, a momentum source term, F_{pump}, is added. With these modifications, the fluid equations are:

$$\partial_t \rho + \partial_x(\rho u) = 0 \tag{3.7}$$

$$\partial_t(\rho u) + \partial_x(\rho u^2) + \partial_x P + \rho\ \vec{g} \cdot \vec{u} + f_w \frac{\rho}{D_h} |u|\, u = F_{pump} \tag{3.8}$$

$$\partial_t(\rho e + \frac{\rho u^2}{2}) + \partial_x \left((\rho e + \frac{\rho u^2}{2}) u \right) + \partial_x(uP) = Q(x,t) + \mathcal{P}_g + \mathcal{P}_f + \mathcal{P}_{pump} \tag{3.9}$$

with $\vec{u} = u\ \vec{e_x}$ and $\vec{e_x}$ is the upward vector in the core.

The Equation Of State is:

$$\rho = \rho_0 + \left.\frac{\partial \rho}{\partial P}\right|_0 (P - P_0) + \left.\frac{\partial \rho}{\partial T}\right|_0 (T - T_0) \tag{3.10}$$

In the above equations, t the time variable, x the spatial coordinate, u the fluid velocity, g the gravity, F_{pump} the pump force, e the internal energy, D_h the hydraulic diameter, and, ρ_0, P_0 and e_0 the fluid density, pressure and internal energy, respectively, at a given pressure and temperature. $\mathcal{P}_g$, $\mathcal{P}_{pump}$ and $\mathcal{P}_f$ are the powers of the gravity, pump and friction forces, respectively. The gravity is taken to be in opposite direction of the upward vector in the left leg of the loop. The energy source term Q is given by Eq. (3.1) in which the wall temperature and the heat transfer are constant. There is no mass source in the continuity equation since it is a closed loop (this assumption is not correct for the cells linked to the pressurizer). All variables depend on space and time.

These equations correspond to the conservative form of Euler Equations with a non-zero right-hand-side and can be written in the general form as follows:

$$\partial_t U + \partial_x F(U) = S \tag{3.11}$$

where S is a source vector that will be described later. U and $F(U)$ are as follows:

$$U = \begin{bmatrix} \rho \\ \rho u \\ \rho e + \frac{1}{2}\rho u^2 \end{bmatrix} \text{ and } F(U) = \begin{bmatrix} \rho u \\ \rho u^2 + P \\ u\left(\rho e + \frac{1}{2}\rho u^2\right) + uP \end{bmatrix} \tag{3.12}$$

U is the vector of conservative variables: density, momentum, and total energy. The source term is:

$$S = \begin{bmatrix} 0 \\ -\rho\ \vec{g} \cdot \vec{u} - f_w \frac{\rho}{D_h} |u|\, u + F_{pump}(x,t) \\ Q(x,t) + \mathcal{P}_g + \mathcal{P}_f + \mathcal{P}_{pump} \end{bmatrix} \tag{3.13}$$

1. Primitive variables

Usually, one solves the Euler Equations in term of conservative variables: density, momentum, and total energy. However, in reactor safety codes, the solution variables are typically density, velocity and temperature. Therefore, we need to convert the above system of equations in terms of these primitive variables. This will yield the so-called non-conservative form of the fluid equations. The following section is dedicated to deriving the non-conservative equations expressed in terms of the primitive variables.

2. The continuity equation and momentum equation

The continuity equation is unchanged :

$$\partial_t \rho + \partial_x(\rho u) = 0. \tag{3.14}$$

The momentum equation is modified as follows. The partial derivatives are expanded for each variable. The assumption required is that the physical variables (velocity, temperature and pressure) are smooth. In the following, all forces (pressure, grav-

ity and friction forces) appearing in the momentum equation are denoted by F for conciseness. Using the product rule of differentiation the momentum equation yields:

$$\begin{aligned} \partial_t(\rho u) + \partial_x(\rho u^2) &= \rho\partial_t u + u\partial_t\rho + \rho u\partial_x u + u\partial_x(\rho u) \\ &= \rho\partial_t u + \rho u\partial_x u + u\left(\partial_t\rho + \partial_x(\rho u)\right) \\ &= F + F_{pump}, \end{aligned} \tag{3.15}$$

where F_{pump} is the pump force. By using the continuity equation, Eq. (3.15) can be further simplified:

$$\rho\partial_t u + \rho u\partial_x u = F + F_{pump}. \tag{3.16}$$

This is the non-conservative form of the momentum equation. The non-conservative denomination is due to the fact that (1) a flux value can no longer be defined as in the case of the conservative form and (2) the velocity is not a conservative variable.

3. The energy equation

Let us recall the energy equation in its conservative form:

$$\partial_t(\rho E) + \partial_x(\rho E u) + \partial_x(up) = Q + \mathcal{P}_g + \mathcal{P}_f + \mathcal{P}_{pump}, \tag{3.17}$$

where E, ρ, u are the total energy per unit mass and volume, the density and the velocity respectively. Q is the heat source or sink in the system. $\mathcal{P}_g$, $\mathcal{P}_{pump}$ and $\mathcal{P}_f$ are the gravity, pump and friction powers. As before, we expand the partial derivatives using the product rule for differentiation:

$$\begin{aligned} \rho\partial_t E &+ E\partial_t\rho + \rho u\partial_x E + E\partial_x(\rho u) + \partial_x(up) \\ &= E\left(\partial_t\rho + \partial_x(\rho u)\right) + \rho\partial_t E + \rho u\partial_x E \\ &= Q + \mathcal{P}_g + \mathcal{P}_f + \mathcal{P}_{pump}. \end{aligned} \tag{3.18}$$

Employing the continuity equation to simplify the equation above yields:

$$\rho\partial_t E + \rho u\partial_x E = Q + \mathcal{P}_g + \mathcal{P}_f + \mathcal{P}_{pump}. \tag{3.19}$$

The last step to obtain the non-conservative form of the equation consists in replacing the total energy E by the sum of the internal and kinetic energies, e and $\frac{1}{2}u^2$:

$$E = e + \frac{1}{2}u^2. \tag{3.20}$$

Since we are interested in solving the energy equation for temperature, the internal energy e is expressed as a function of the temperature T and the heat capacity C_v as follows:

$$e = C_v T. \tag{3.21}$$

The heat capacity C_v is constant in this model as stated in the model assumptions. Then, Eq. (3.19) yields:

$$\begin{aligned}
&\rho\ C_v\partial_t T + \rho\partial_t\frac{u^2}{2} + \rho u C_v\partial_x T + \rho u\partial_x\frac{u^2}{2} + u\partial_x P + P\partial_x u \\
&\quad = \rho\ C_v\partial_t T + \rho u C_v\partial_x T + P\partial_x u + u\left(\rho\partial_t u + \rho u\partial_x u + \partial_x P\right) \\
&\quad = Q + \mathcal{P}_g + \mathcal{P}_f + \mathcal{P}_{pump}
\end{aligned} \tag{3.22}$$

Finally, using the non-conservative momentum expression of Eq. (3.16), Eq. (3.22) becomes:

$$\rho\ C_v\partial_t T + \rho u C_v\partial_x T + P\partial_x u + u\left(F_g + F_f + F_{pump}\right) = Q + \mathcal{P}_g + \mathcal{P}_f + \mathcal{P}_{pump} \tag{3.23}$$

To further simplify this equation, we recall the definition of the power: a force multiply by the velocity. As a result, in the left-hand-side of the equation, the friction, pump and gravity power are recognized, so that the non-conservative form of the energy

equation finally is:

$$\rho\, C_v \partial_t T + \rho u C_v \partial_x T + P \partial_x u = Q. \tag{3.24}$$

Using the non-conservative form of fluid flow equations along with the EOS, the system can be solved in term of primitive variables. These equations cannot be used for the cells linked to the pressurizer since a mass source is required as explained in section 2.

D. Pump and pressurizer models

1. Pump model

The pump is implemented as a gravity force since it introduces artificial gravity in the system.

$$F_{pump} = \rho g s_p, \tag{3.25}$$

where F_{pump} is the pump force in the momentum equation, ρ and g are the density and the gravity acceleration, respectively, and s_p is the pump strength. The value of s_p is selected in order to obtain a fluid velocity representative of the reactor systems modeled. The pump is uniformly distributed over a given length (user-defined input value) so that the pump is independent of the grid size. A ramp can also be set in the code in order to study pump transients (e.g., pump coast down).

2. Pressurizer model

The purpose of the pressurizer is to set the pressure at a given point in the system. In our simplified model, we are not interested in keeping track of the fluid level in the pressurizer. However, some fluid is exchanged between the loop and the pressurizer in order to maintain the pressure at a given value set by the operator. The pressurizer temperature is set equal to the temperature of the cell linked to it. Since the fluid

can flow in and out of the loop into the pressurizer, a pressurizer velocity u_p has to be computed. As a result, a momentum equation is added to the nonlinear residual vector of the discretized equations for each cell linked to the pressurizer.It is given in Eq. (3.26).

$$\rho_p \partial_t u_p + \rho_p u_p \partial_x u_p = F, \tag{3.26}$$

where u_p is the pressurizer velocity and ρ_p is the pressurizer density (this is the only equation solved for the pressurizer; ρ_p is determined from the EOS knowing (i) the temperature of the cells linked to the pressurizer and (ii) the pressurizer pressure which is a given and reactor-dependent).

In addition, the pressurizer behaves either as a heat sink or source so that its presence requires an additional term in the continuity and energy equations in the cells concerned (a mass and energy source or sink respectively):

$$m_{source} = \frac{(\widetilde{\rho} u_p)}{\Delta x} \tag{3.27}$$

$$e_{source} = C_v \frac{\left(\widetilde{\rho T} u_p\right)}{\Delta x} \tag{3.28}$$

where Δx is the grid size. $(\widetilde{\rho} u_p)$ and $\left(\widetilde{\rho T} u\right)$ are numerical fluxes obtained by applying a simple upwind scheme. The numerical scheme is further discussed in Section F. As in the case of the pump, the pressurizer model is independent of the space grid size in order to avoid having strong pressure discontinuities in the system.

E. Fluid flow models

1. Laminar and turbulent flows

Laminar and turbulent flows correlations are both implemented for the friction term, depending on the Reynolds number. But only the laminar flows correlation is used in this thesis. The correlations presented here are used for transient and steady-state

runs. In the case of laminar flows, the friction factor f_w is a function of the Reynold number Re as follows:

$$f_w = \frac{64}{Re} \tag{3.29}$$

Th expression Eq. (3.29) is known as the Darcy–Weisbach factor [7]. For turbulent flows, the Blasius correlation is used and given below:

$$f_w = 0.079 Re^{-0.25} \tag{3.30}$$

The Blasius correlation can be used under some particular conditions: it is applicable well for liquid water but requires either some modifications or the use of another correlation in the case of gases. The Reynold number is a function of velocity u, hydraulic diameter D_h, viscosity μ, and density ρ, and is given as follows:

$$Re = \frac{\rho D_h \left|u\right|}{\mu} \tag{3.31}$$

2. Darcy's law

Darcy's law can be used to model flows in porous media. For reactor applications, this could be, for instance, fluid flow a pebble bed gas reactor. Darcy's law assumes a porous medium and a laminar flow and is obtained from the momentum equation by setting the time dependent term and the convection term to zero in Eq. (3.16) (for both compressible and incompressible flows).

$$\rho g + f_w \frac{\rho}{D_h} u \left|u\right| + \partial_x P = 0 \tag{3.32}$$

Assuming a laminar flow, the friction force F_f appearing the momentum equation can be expressed as follows:

$$\begin{aligned} F_f &= f_w \frac{\rho}{D_h} u\,|u| \\ &= \frac{64}{Re} \frac{\rho}{D_h} u\,|u| \\ &= \frac{64}{D_h^2} \mu u \end{aligned} \tag{3.33}$$

where Eq. (3.29) and Eq. (3.31) were employed. Hence, the velocity can be given by a linear equation:

$$u = -\left(\frac{\partial P}{\partial x} + \rho g\right) \frac{D_h^2}{64\mu} \tag{3.34}$$

F. Final forms of the equations

The fluid flow models (compressible, incompressible, with or without Boussinesq correction, with or without Darcy's law approximation) can be written in a generic form in which each model can be turned on and off using some binary α parameters. Hence, a single code and solution algorithm is employed to assess in a consistent fashion the effects of the various models. The generic form of the equations with the α parameters are given:

$$\partial_t \rho + \partial_x(\rho u) = 0 \tag{3.35}$$

$$\alpha_4 \left(\rho \partial_t u + \rho u \partial_x u\right) + \hat{\rho} g (1 - s_p) + f_w \frac{\rho}{D_h} |u|\, u + \partial_x P = 0 \tag{3.36}$$

$$\rho\ C_v \partial_t T + \rho u C_v \partial_x T + P \partial_x u = Q \tag{3.37}$$

$$\rho = \rho_0 + \alpha_1 \left.\frac{\partial \rho}{\partial P}\right|_0 (P - P_0) + \alpha_2 \left.\frac{\partial \rho}{\partial T}\right|_0 (T - T_0) \tag{3.38}$$

$$\hat{\rho} = \rho_0 + \alpha_1 \left.\frac{\partial \rho}{\partial P}\right|_0 (P - P_0) + \alpha_3 \left.\frac{\partial \rho}{\partial T}\right|_0 (T - T_0) \tag{3.39}$$

The different combinations of α_i are summarized in Table III-I. Note that the incom-

pressible flow model without the Boussinesq correction is not employed here (natural convection cannot occur under this assumption). Only four cases are presented in this thesis: compressible and incompressible flow models with Boussinesq correction for the PWR, and Darcy's law and compressible model for the HTGR.

Table III-I. Alpha combinations

Flow option	α_1	α_2	α_3	α_4
Compressible	1	1	1	1
Incompressible without Boussinesq	0	0	0	1
Incompressible with Boussinesq	0	0	1	1
Compressible Darcy	1	1	1	0

CHAPTER IV

DISCRETIZATION, SCALING, AND SOLUTION METHOD

This section describes the numerical method used in the pilot code. After giving the implicit and explicit forms of the Euler equations, the Jacobian-free-Newton-Krylov method (solution method) is explained. The other sections deal with numerical techniques used such as scaling, preconditioner, convergence criteria and numerical fluxes.

A. Discretized fluid flow equations

A standard finite volume (FV) spatial discretization based on staggered grids is employed and recalled below. The stored variables are the temperature, the pressure, and the velocity (density depends on temperature and pressure through the EOS and hence is not stored). In a staggered grid technique, two grids are employed; there is an offset of half a cell in between the grids so that the cell edges of the first grid corresponds to the cell centers of the second grid. This method makes the FV stable and numerical fluxes can be easily computed for each equation. Only the continuity, momentum, and energy equations are discretized using the grids shown in Fig. IV-1. The EOS does not need to be discretized. Two temporal discretizations are employed, the implicit and semi-implicit methods. These schemes are described next.

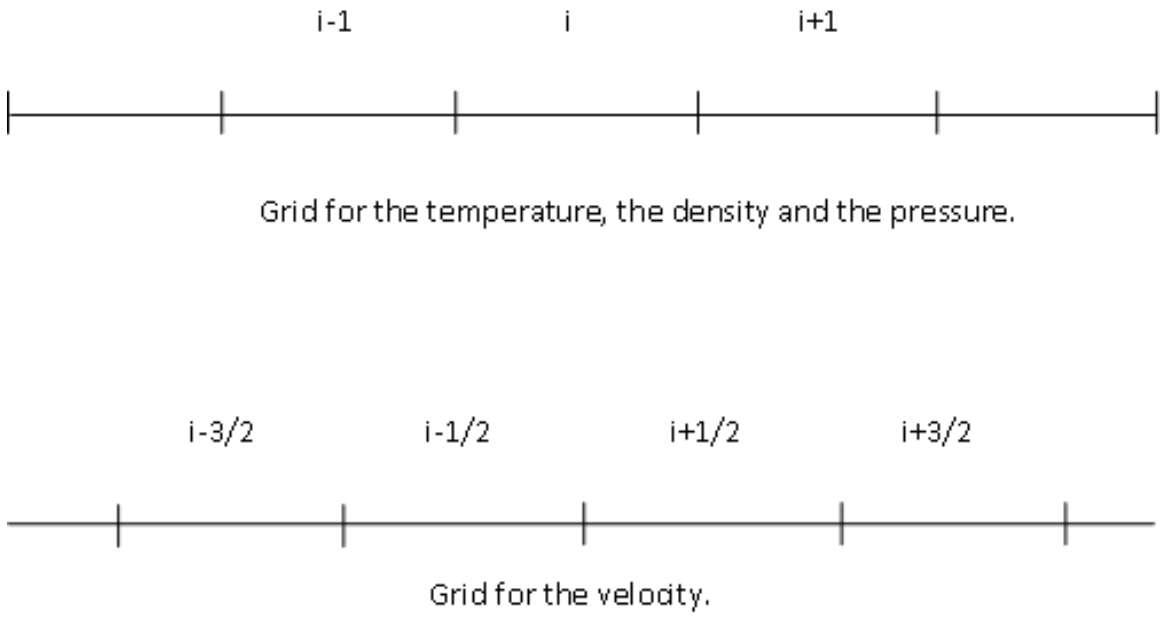

Fig. IV-1. Staggered grids for the FV spatial discretization. Top: grid for T, ρ, and P; Bottom: grid for u.

B. Time implicit method

Backward (implicit) Euler time integration of the Finite Volume equations yields the following discretized equations.

Integrating the continuity expression, Eq. (3.14), over spatial cell i yields:

$$\frac{\rho_i^{n+1} - \rho_i^n}{\Delta t} + \frac{(\widetilde{\rho} u)_{i+\frac{1}{2}}^{n+1} - (\widetilde{\rho} u)_{i-\frac{1}{2}}^{n+1}}{\Delta x} = 0 \tag{4.1}$$

Integrating the momentum expression, Eq. (3.16), over spatial cell $i+\frac{1}{2}$ yields:

$$\overline{\rho}_{i+\frac{1}{2}}^{n+1}\frac{u_{i+\frac{1}{2}}^{n+1}-u_{i+\frac{1}{2}}^{n}}{\Delta t}+\overline{\rho}_{i+\frac{1}{2}}^{n+1}u_{i+\frac{1}{2}}^{n+1}\frac{\widetilde{u}_{i+1}^{n+1}-\widetilde{u}_{i}^{n+1}}{\Delta x} + \frac{P_{i+1}^{n+1}-P_{i}^{n+1}}{\Delta x}+\overline{\hat{\rho}}_{i+\frac{1}{2}}^{n+1}g+ \tag{4.2}$$

$$f_w\frac{\rho_{i+\frac{1}{2}}^{n+1}}{D_h}\left|u\right|_{i+\frac{1}{2}}^{n+1}u_{i+\frac{1}{2}}^{n+1}=F_{pump,i+\frac{1}{2}}^{n+1} \tag{4.3}$$

Integrating the energy expression, Eq. (3.24), over spatial cell i yields:

$$C_v\frac{(\rho T)_i^{n+1}-(\rho T)_i^{n}}{\Delta t}+C_v\frac{(\widetilde{\rho T}u)_{i+\frac{1}{2}}^{n+1}-(\widetilde{\rho T}u)_{i-\frac{1}{2}}^{n+1}}{\Delta x} + P_i^{n+1}\frac{\widetilde{u}_{i+\frac{1}{2}}^{n+1}-\widetilde{u}_{i-\frac{1}{2}}^{n+1}}{\Delta x}=Q_i^{n+1} \tag{4.4}$$

where Δt and Δx are the temporal and spatial discretization grid sizes, n and i are temporal and spatial indices, respectively. The variable $\hat{\rho}$ can be different from the density variable ρ when the Boussinesq correction is applied: for compressible fluids, the two variables are identical; for incompressible flows with the Boussinesq correction, $\hat{\rho}$ depends on temperature through the EOS, whereas ρ is constant. The notation $\overline{\rho}_{i+\frac{1}{2}}^{n+1}$ denotes the average density on cells i and $i+1$ at time $n+1$. The notation $\overline{u}_i^{n+1}$ denotes the average velocity on edges $i+\frac{1}{2}$ and $i-\frac{1}{2}$ at time $n+1$.

$$\overline{\rho}_{i+\frac{1}{2}}^{n+1}=\frac{\rho_{i+1}^{n+1}+\rho_i^{n+1}}{2} \tag{4.5}$$

$$\overline{u}_i^{n+1}=\frac{u_{i+\frac{1}{2}}^{n+1}+u_{i-\frac{1}{2}}^{n+1}}{2} \tag{4.6}$$

The notation $(\widetilde{\rho}u)_{i+\frac{1}{2}}^{n+1}$ denotes the numerical flux of ρu on the right edge of cell i at time $n+1$ and is computed using the upwind scheme (see section F).

C. The semi-implicit method

In the semi-implicit method, some variables are discretized in an explicit fashion and some others implicitly. In doing so, the number of Newton iterations can be reduced and the code runs faster. The semi-implicit equations are given by:

$$\frac{\rho_i^{n+1}-\rho_i^n}{\Delta t}+\frac{\widetilde{\rho}_{i+\frac{1}{2}}^n u_{i+\frac{1}{2}}^{n+1}-\widetilde{\rho}_{i-\frac{1}{2}}^n u_{i-\frac{1}{2}}^{n+1}}{\Delta x}=0 \tag{4.7}$$

$$\overline{\rho}_{i+\frac{1}{2}}^n\frac{u_{i+\frac{1}{2}}^{n+1}-u_{i+\frac{1}{2}}^n}{\Delta x}+\overline{\rho}_{i+\frac{1}{2}}^n u_{i+\frac{1}{2}}^n\frac{\widetilde{u}_i^n-\widetilde{u}_i^n}{\Delta x}+\frac{P_{i+1}^{n+1}-P_i^{n+1}}{\Delta x}+ \tag{4.8}$$

$$\overline{\widehat{\rho}}_{i+\frac{1}{2}}^n g+f_w\frac{\rho_{i+\frac{1}{2}}^n}{D_h}\left|u\right|_{i+\frac{1}{2}}^n u_{i+\frac{1}{2}}^{n+1}=0 \tag{4.9}$$

$$C_v T_i^n\frac{\rho_i^{n+1}-\rho_i^n}{\Delta t}+C_v\rho_i^n\frac{T_i^{n+1}-T_i^n}{\Delta t}$$

$$+C_v\frac{\left(\widetilde{\rho T}\right)_{i+\frac{1}{2}}^{n+1}u_{i+\frac{1}{2}}^n-\left(\widetilde{\rho T}\right)_{i-\frac{1}{2}}^{n+1}u_{i-\frac{1}{2}}^n}{\Delta x}+P_i^n\frac{u_{i+\frac{1}{2}}^{n+1}-u_{i-\frac{1}{2}}^{n+1}}{\Delta x}=Q_i^{n+1} \tag{4.10}$$

In the semi-implicit formulation, some variables are treated explicitly. In the continuity equation, the mass flow is now an explicit variable. The velocity is taken at time n. In the momentum equation, all terms are explicit except the pressure that is treated implicitly. In the energy equation, the velocity is implicit in all terms of the equations and only the pressure is explicit. The time derivative term is broken down into two terms.

D. Solution method

After temporal and spatial discretization, the above problem forms a set of nonlinear equations for the unknowns at time t^{n+1}. There are $N = 3 \times n_{el}$ unknowns: 3 types of variables per cell (ρ, u, T); 1 unknown per variable per cell (FV method); and a total of n_{el} cells. The nonlinear system of equation can be expressed as follows

$$\mathcal{F}(U^{n+1})=0 \tag{4.11}$$

(we will drop the $^{n+1}$ superscript in the rest of this section). $\mathcal{F}$ is a nonlinear residual vector of N components. This nonlinear system is solved iteratively (iteration index is ℓ) using Newton's method:

$$\left.\frac{\partial \mathcal{F}}{\partial U}\right|_{U^\ell} \delta U = -\mathcal{F}(U^\ell) \tag{4.12}$$

$$U^{\ell+1} = U^\ell + \delta U \tag{4.13}$$

until $|\mathcal{F}(U^\ell)| < \epsilon$. The Jacobian matrix $J = \frac{\partial \mathcal{F}}{\partial U}$ is never formed. Rather, the (non-symmetric) linear system $J\delta U = -\mathcal{F}$ is solved using a Krylov method (GMRES). In Krylov methods, only the action of the matrix on a Krylov vector ν is required. Here, this is approximated using a finite difference formula as follows

$$J\nu \simeq \frac{\mathcal{F}(U^\ell + \varepsilon\nu) - \mathcal{F}(U^\ell)}{\varepsilon} \tag{4.14}$$

where ε is typically the square-root of machine precision. Hence, only a function that evaluates the nonlinear residual $\mathcal{F}$ is required. This forms the basics of the Jacobian-free Newton-Krylov (JFNK) techniques.

Another method used to solve the non-linear equations is the Picard iteration technique. It consists of ,(1), lagging some parameters of the discretized equations given in Eq. (4.15), Eq. (4.16) and Eq. (4.17) in order to linearize the system, and , (2), iterating until convergence. The discretized equations used in this case are the following:

$$\frac{\rho_{l+1}^{n+1} - \rho^n}{\Delta t} + \frac{\left(\rho_{l+1}^{n+1} u_l^{n+1}\right)_{i+\frac{1}{2}} - \left(\rho_{l+1}^{n+1} u_l^{n+1}\right)_{i-\frac{1}{2}}}{\Delta x} = 0 \tag{4.15}$$

$$\left(\bar{\rho}_l^{n+1}\right)_{i+\frac{1}{2}} \frac{\left(u_{l+1}^{n+1}\right)_{i+\frac{1}{2}} - (u^n)_{i-\frac{1}{2}}}{\Delta t} + \left(\bar{\rho}_l^{n+1}\right)_{i+\frac{1}{2}} \left(u_l^{n+1}\right)_{i+\frac{1}{2}} \frac{\left(u_{l+1}^{n+1}\right)_{i+1} - \left(u_{l+1}^{n+1}\right)_i}{\Delta x} + \frac{\left(P_{l+1}^{n+1}\right)_{i+1} - \left(P_{l+1}^{n+1}\right)_i}{\Delta x} + \bar{\rho}_{l+1}^{n+1}{}_{i+\frac{1}{2}} g + f \frac{\left(\rho_l^{n+1}\right)_{i+\frac{1}{2}}}{D_h} \left|u_l^{n+1}\right|_{i+\frac{1}{2}} \left(u_{l+1}^{n+1}\right)_{i+\frac{1}{2}} = F_{pump} \tag{4.16}$$

$$C_v \frac{\left(\rho_l^{n+1} T_{l+1}^{n+1}\right)_i - (\rho^n T^n)_i}{\Delta t} + C_v \frac{\left(T_{l+1}^{n+1} u_l^{n+1}\right)_{i+\frac{1}{2}} - \left(T_{l+1}^{n+1} u_l^{n+1}\right)_{i-\frac{1}{2}}}{\Delta x} + \left(P_l^{n+1}\right)_i \frac{\left(u_{l+1}^{n+1}\right)_{i+\frac{1}{2}} - \left(u_{l+1}^{n+1}\right)_{i-\frac{1}{2}}}{\Delta x} = Q_i^{n+1} \tag{4.17}$$

where i, n and $n+1$ are defined as previously. The parameters l and $l+1$ are the l^{th} and $l+1^{th}$ iterations. This method allows linearizing the system by using the vector solution of the previous Newton iteration.

Picard and the JFNK techniques are implemented in the same function and only differ by the type of inputs. Three input vectors are required: U^n, U_l^{n+1} and U_{l+1}^{n+1} that are the vector solution at time n, $n+1$ and iteration l, and time $n+1$ and iteration $l+1$, respectively. The residual can be decomposed a a function of a matrix, A, a vector and a source term, S (Eq. (4.18)):

$$\mathcal{F}(U_{l+1}^{n+1}, U_l^{n+1}, U^n) = A(U_l^{n+1}) U_{l+1}^{n+1} - S = 0 \tag{4.18}$$

$$S = \mathcal{F}(0, 0, U^n) \tag{4.19}$$

where A is an approximation to the Jacobian matrix and is computed by using Eq. (4.20):

$$A(U_l^{n+1}) = \frac{\mathcal{F}(U_{l+1}^{n+1} + \epsilon v, U_l^{n+1}, U^n) - \mathcal{F}(U_{l+1}^{n+1}, U_l^{n+1}, U^n)}{\epsilon} \tag{4.20}$$

where ϵ is a parameter to set and v is a unitarian vector. When, JFNK technique is used, the vectors U_{l+1}^{n+1} and U_l^{n+1} equal each other and therefore A is the Jacobian

matrix.

E. Convergence criteria, scaling and preconditioner

Matlab is used to code the modified Euler Equations. The code is broken down in many functions in order to facilitate modifications and updates. It has an input file that allows changing all the parameters relative to the fluid (viscosity, heat capacity, ...) and the system (Q_{in}, Q_{out}, ...). Some further details about the code are given:

- The variables (pressure and temperature) are scaled in order to reduce the condition number of the Jacobian matrix. This should limit the singularity of J at very low Mach numbers which might be the case if the pump is turned off [8].The temperature and pressure are scaled as follows:

$$P(x,t) = P_0 + cP'(x,t) \tag{4.21}$$

$$T(x,t) = d \cdot T'(x,t), \tag{4.22}$$

  where $P(x,t)$ and P_0 are the pressure in the loop and the average pressure in the loop respectively. $P'(x,t)$ is the variation of the pressure around the average pressure of the system. c is a constant that can be adjusted in order to make $P'(x,t)$ smaller or bigger. The variables $T(x,t)$ and $T'(x,t)$ are the temperatures of the fluid. d is also a constant that can be adjusted. The process of scaling aims at making all variables vary between 1 and 10 in the solution vector, yielding a smaller condition number. Scaling reduced the condition number from 10^{16} to 10^{8}. It was tested that the numerical solution is not scaling-dependent.

- Two convergence criteria are used for the GMRES method. The exact Newton is used (i.e., the nonlinear system is solved to a given tolerance) and an additional

criterion, given in Eq. (4.23), is set in order to force the system to converge when steady state is reached:

$$\frac{\delta U}{U} < tol, \tag{4.23}$$

where δU is the update vector computed by the GMRES method, U is the solution vector and tol is the tolerance ($tol = 10^{-8}$).

- The Jacobian matrix (Jacobian matrix of the previous time step) is used as a preconditioner in the GMRES method. Computing the Jacobian matrix, however, can be time consuming when a large number of cells is utilized.

- Steady state is detected by computing the heat removed from and supplied to the system. When they equal each other within a given tolerance, it is considered that the steady state has been reached:

$$Q_{in} = -Q_{out} \tag{4.24}$$

- A description of the various functions of the code can be found in appendix A.

F. Numerical flux

The numerical flux used here is a modification of the upwind method [9]. First the standard upwind method is recalled and then the numerical flux used is described. Let consider three cells $i-1$, i and $i+1$ and the continuity equation discretized on cell i. Two cases are possible at edge $i+\frac{1}{2}$ (these cases are explained with the density as an example but can be applied to any variables). The standard upwind method is defined as follows:

$$\widetilde{\rho}_{i+\frac{1}{2}} = \begin{cases} \rho_i & \text{if } u^{n+1}_{i+\frac{1}{2}} > 0 \\ \rho_{i+1} & \text{if } u^{n+1}_{+\frac{1}{2}} < 0 \end{cases} \quad \forall i \in [1,\, n_{el}] \tag{4.25}$$

The numerical flux used in this thesis is not based on the velocity but the on the average velocity on a cell as follows. The average velocity in cell i is defined as the average of velocities in cells $i+\frac{1}{2}$ and $i-\frac{1}{2}$ as in Eq. (4.5).

- if the average velocity is positive at the given edge, the density $\widetilde{\rho}_{i+\frac{1}{2}}$ equals the density in cell i,
- if the average velocity is negative at the given edge, the density $\widetilde{\rho}_{i+\frac{1}{2}}$ equals the density in cell $i+1$.

That is

$$\widetilde{\rho}_{i+\frac{1}{2}} = \begin{cases} \rho_i & \text{if } \overline{u}_i^{n+1} > 0 \\ \rho_{i+1} & \text{if } \overline{u}_i^{n+1} < 0 \end{cases} \quad \forall i \in [1,\, n_{el}] \tag{4.26}$$

Similar definitions of numerical fluxes hold for other variables, as required in the spatial FV scheme. This numerical flux does not conserve the momentum (that is momentum fluxed out of cell $i+\frac{1}{2}$ at face i is not the momentum fluxed into cell $i-\frac{1}{2}$) but is stable in all cases. Some other numerical fluxes could be used in future work (e.g., central difference).

G. Complete form of the discretized equations

In this section, the continuity, momentum and energy equations are given in Eq. (4.27), Eq. (4.28) and Eq. (4.29), respectively.

$$\frac{\rho_i^{n+1} - \rho_i^n}{\Delta t} + \frac{(\widetilde{\rho}u)_{i+\frac{1}{2}}^{n+1} - (\widetilde{\rho}u)_{i-\frac{1}{2}}^{n+1}}{\Delta x} = \frac{(\widetilde{\rho}u_p)}{\Delta x}\chi \tag{4.27}$$

$$\begin{aligned} &\overline{\rho}_{i+\frac{1}{2}}^{n+1}\frac{u_{i+\frac{1}{2}}^{n+1} - u_{i+\frac{1}{2}}^{n}}{\Delta t} + \overline{\rho}_{i+\frac{1}{2}}^{n+1}u_{i+\frac{1}{2}}^{n+1}\frac{\widetilde{u}_{i+1}^{n+1} - \widetilde{u}_i^{n+1}}{\Delta x} \\ &+\frac{P_{i+1}^{n+1} - P_i^{n+1}}{\Delta x} + \overline{\widehat{\rho}}_{i+\frac{1}{2}}^{n+1}g + f\frac{\rho_{i+\frac{1}{2}}^{n+1}}{D_h}\,|u|_{i+\frac{1}{2}}^{n+1}\,u_{i+\frac{1}{2}}^{n+1} = \overline{\rho}_{i+\frac{1}{2}}^{n+1}gs_p \end{aligned} \tag{4.28}$$

$$C_v \frac{(\rho T)_i^{n+1} - (\rho T)_i^n}{\Delta t} + C_v \frac{(\widetilde{\rho T} u)_{i+\frac{1}{2}}^{n+1} - (\widetilde{\rho T} u)_{i-\frac{1}{2}}^{n+1}}{\Delta x} + P_i^{n+1} \frac{\widetilde{u}_{i+\frac{1}{2}}^{n+1} - \widetilde{u}_{i-\frac{1}{2}}^{n+1}}{\Delta x}$$
$$= h\left(T_i^{n+1} - T_{wall}\right) + C_v \frac{\left(\widetilde{\rho T} u_p\right)}{\Delta x} \chi \qquad (4.29)$$

where χ is a characteristic function and is given in Eq. (4.30):

$$\chi = \left\{ \begin{array}{c} 1 \text{ if } x \in [L_3; L_3 + L_4] \\ \\ 0 \text{ else} \end{array} \right\} \qquad (4.30)$$

where L_3 and L_4 are defined in Fig. V-3 on p.36.

CHAPTER V

CODE VERIFICATION

This chapter describes the temporal and spatial convergence rates for the compressible model. In the case of the incompressible model, an analytical solution is derived and used to quantify the spatial error. The following pseudo transient is used in this chapter to reach a steady-state: a ramp of 9 seconds is set for the source and sink energy, the error is computed at the time $t = 20$ seconds in order to have smooth variations in the solutions (steady-state is reached around $t = 50s$).

A. Temporal convergence

The time integration method used is first-order in time. Hence, the temporal error $\epsilon_{\Delta t}$ should be decreased by a factor of two each time the time step size is decreased by a factor two.

$$\epsilon_{\Delta t} = C\Delta t^p \tag{5.1}$$

$$\log(\epsilon) = \log(C) + p \times \log(\Delta t), \tag{5.2}$$

where C is a constant depending on the system of equations of the time-stepping scheme, and p is the order of the numerical method ($p = 1$ for Backward Euler). The second form of the equation is used to plot the log of the error as a function of the log of the time step, yielding the numerical slope p. In order to avoid any pollution from the spatial discretization error, a very fine spatial mesh is utilized. To perform the temporal convergence analysis, the following time steps, given in seconds, have been employed: 2, 1, 0.5, 0.25, 0.125, 0.0625 and 0.03125. The average error is computed

using successive numerical solutions as follows:

$$\epsilon_{\Delta t} = \frac{1}{n_{el}} \sum_{i=1}^{n_{el}} \left(U(i,t)_{\Delta t} - U(i,t)_{\frac{\Delta t}{2}} \right), \tag{5.3}$$

where $\epsilon_{\Delta t}$ is the average difference between numerical simulations employing time steps Δt and $\frac{\Delta t}{2}$, n_{el} is the number of cells, and $U(i,t)$ is the solution vector in cell i at time t. The temperature error is plotted versus the time step in Fig. V-1.

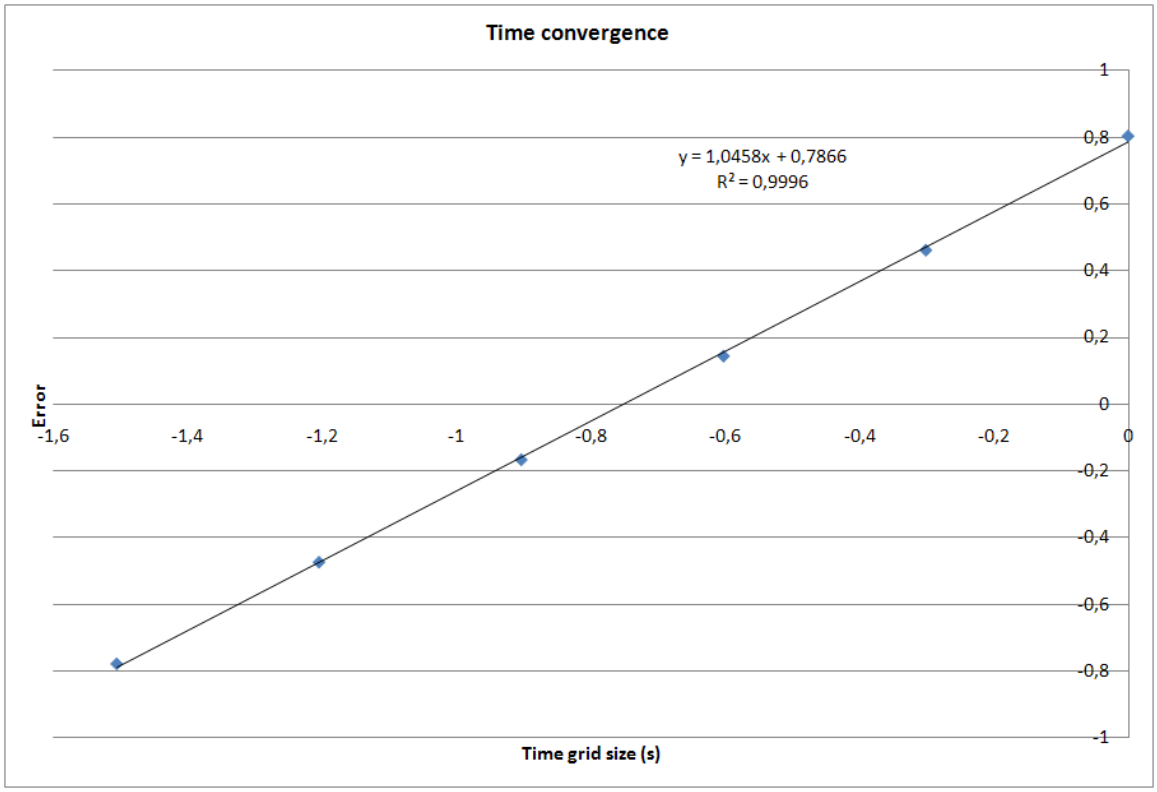

Fig. V-1. Time convergence.

The numerically observed slope is 1.0458, which is close to the expected theoretical value of 1. This proves that the code is indeed first-order in time.

B. Spatial convergence

In this section,spatial convergence is demonstrated. The procedure employed is the following: the space grid size is changed by a factor of two for each new simulation while the time step chosen is constant and small to avoid pollution from the temporal discretization error. The error is computed at steady-state with Eq. (5.2) and is plotted as function of the space grid size in Fig. V-2. A slope of 0.9633 is observed, showing that the code is first-order in space.

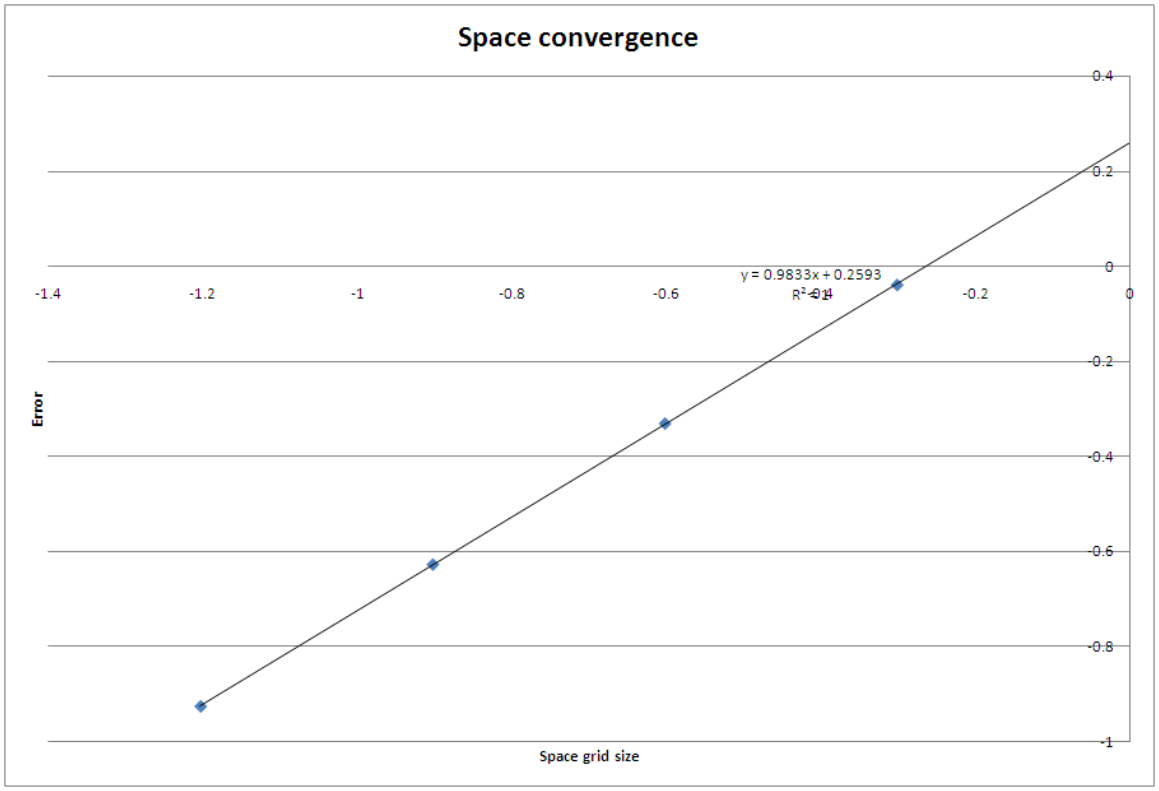

Fig. V-2. Space convergence.

C. Mesh refinement with an analytical solution

In the case of the incompressible model, it is possible to derive an analytical solution from the equations. The modified Euler Equations in the case of the incompressible

model (with Boussinesq correction) are recalled:

$$\partial_x(u) = 0 \tag{5.4}$$

$$\rho\partial_t u + \rho u\partial_x u + \partial_x P + \hat{\rho} g\left(1 - s_p\right) + f_w \frac{\rho}{D_h}\left|u\right| u = 0 \tag{5.5}$$

$$\rho\ C_v\partial_t T + \rho u C_v \partial_x T + P\partial_x u = Q(x,t) \tag{5.6}$$

$$\rho = \rho_0 \tag{5.7}$$

$$\hat{\rho} = \rho_0 + \frac{\partial\rho}{\partial T}\left(T - T_0\right) \tag{5.8}$$

The momentum and energy equations can be simplified using the continuity equation:

$$\rho_0\partial_t u + \partial_x P + \hat{\rho} g\left(1 - s_p\right) + f_w \frac{\rho_0}{D_h}\left|u\right| u = 0 \tag{5.9}$$

$$\rho_0\ C_v\partial_t T + \rho_0 u C_v \partial_x T = Q(x,t). \tag{5.10}$$

An analytical solution can be derived from the equation above at steady state assumption. The steps are detailed for the temperature and pressure profiles along the core and the results will be given for the other legs of the loop (pressurizer, steam generator and pump) in Appendix B.

Along the core, the heat source is $Q(x) = h_{core} L_1 \left(T_{wcore} - T(x)\right)$ in one dimension where h is the heat transfer coefficient, L_1 is the length of the core, T_{wcore} is the wall temperature along the core (given) and $T(x)$ is the fluid temperature profile along the core (it is assumed that the area is $L_1 \times 1$). Then, the energy equation yields:

$$\rho_0 u C_v \partial_x T = h_{core} L_1 \left(T_{wcore} - T(x)\right) \tag{5.11}$$

$$T(x) + \frac{\rho_0 u C_v}{h_{core} L_1}\partial_x T(x) = T_{wcore} \tag{5.12}$$

This is a first order differential equation that can be solved analytically. To simplify the equation, let us define $l_{core} = \frac{\rho_0 u C_v}{h_{core} L_1}$ which is the characteristic length of the

energy equation. The parameter l_{core} depends on the fluid velocity so that it will affect the temperature profile as expected. A solution for this type of differential equation is (the temperature is solved as a function of position x):

$$T_{core}(x) = T_{wcore} + Be^{\frac{-x}{l_{core}}}, \tag{5.13}$$

where B is a yet-to-be-determined constant. Eq. (5.13) gives the temperature profile along the core. We can now derive the pressure profile along the core using the momentum equation. The temperature and the pressure are coupled through the Boussinesq correction in the momentum equation. The pressure along the core is given by Eq. (5.14)

$$\begin{aligned} P(x) = \frac{\partial \rho}{\partial T} B g l_{core} \left(e^{\frac{-x}{l_{core}}} - e^{\frac{-L_1}{l_{core}}} \right) - \\ \left[\left(\rho_0 + \frac{\partial \rho}{\partial T} \left(T_{core} - T_0 \right) \right) g + f_w \frac{\rho_0}{D_h} \left| u \right| u \right] \left(L_1 - x \right) + P_p, \end{aligned} \tag{5.14}$$

where P_p is the pressure in the pressurizer and is an input in the code. Eq. (5.14) gives the pressure as a function of space at steady-state along the core. This analytical solution will be used as a reference for the numerical solution. Of course, the constant B has to be computed. This requires one to compute the temperature profile along the steam generator. The energy equation to solve for the steam generator is the following:

$$\begin{aligned} \rho_0 u C_v \partial_x T = h_{sg} L_1 \left(T_{wsg} - T(x) \right) \\ T(x) + \frac{\rho_0 u C_v}{h_{sg} L_1} \partial_x T(x) = T_{wsg}, \end{aligned} \tag{5.15}$$

where T_{wsg} is the temperature in the steam generator, h_{sg} is the heat transfer coefficient between the fluid and the steam generator. All other variables are defined as above. We also define $l_{sg} = \frac{\rho_0 u C_v}{h_{sg} L_1}$ to be the space scale of the energy equation along

the steam generator. The solution technique is the same as before and the solution is:

$$T_{sg}(x) = T_{wsg} + De^{\frac{-(x+L_1+L_2)}{l_{sg}}}, \tag{5.16}$$

where D is a constant to be determined. To obtain the constants B and D, two equations are required. The first one is obtained by stating that the temperature along the pump leg is constant since, in this model, the pump does not modify the energy equation (this assumption is not true along the pressurizer). As a result:

$$T_{core}\left(x = 0\right) = T_{sg}\left(x = 2L_1 + L_2\right), \tag{5.17}$$

where T_{sg} and T_{core} are the temperatures in the steam generator and in the core, respectively, and L_1 and L_2 are the loop lengths. The second equation is obtained by considering that the steady-state is reached when the energy put into and removed from the system equal each other:

$$Q_{in} = -Q_{out} \tag{5.18}$$

Using these two relations above, the system can be solved and the constants expressed as a function of the boundary conditions (since the system is periodic, the boundary conditions are defined as the temperature in the core and in the stem generator).

$$D = \frac{T_{wcore} - T_{wsg}}{e^{-\frac{(2L_1+L_2)}{l_{sg}}} - \frac{l_{sg}h_{sg}}{l_{core}h_{core}} \frac{e^{-\frac{(2L_1+L_2)}{l_{sg}}} - e^{-\frac{(L_1+L_2)}{l_{sg}}}}{1-e^{-\frac{L_1}{l_{core}}}}} \tag{5.19}$$

$$B = \left(T_{wcore} - T_{wsg}\right)\left(\frac{1}{1 - \frac{l_{sg}h_{sg}}{l_{core}h_{core}} \frac{1-e^{-\frac{L_1}{l_{sg}}}}{1-e^{-\frac{L_1}{l_{core}}}}} - 1\right) \tag{5.20}$$

As it can be seen in Eq. (5.19) and Eq. (5.20), the constants B and D are independent of the initial conditions in the case of the incompressible model. Since the constants

B and D are known, the pressure equations can be derived:

$$P(x) = \frac{(T_{wcore} - T_{wsg})\, g}{l_{core}} \left(\frac{1}{1 - \frac{l_{sg} h_{sg}}{l_{core} h_{core}} \frac{1 - e^{-\frac{L_1}{l_{sg}}}}{1 - e^{-\frac{L_1}{l_{core}}}}} - 1 \right) \left(e^{\frac{-x}{l_{core}}} - e^{\frac{-L_1}{l_{core}}} \right) - \left[\left(\rho_0 + \frac{\rho_0}{T} \right) g + f_w \frac{\rho_0}{D_h} |u|\, u \right] (L_1 - x) + P_p \tag{5.21}$$

The same study can be done for all the other legs of the loop. These steps are not detailed here but the technique is similar. There is neither a heat source nor sink along the horizontal legs containing the pressurizer and the pump (the temperature in the pressurizer is set to the temperature of the cells linked to it). The temperature and the pressure equations along the pressurizer are:

$$T_{pressurizer}(x) = T_{core}(x = L_1) \tag{5.22}$$

$$P_{pressurizer}(x) = P_p + f \frac{\rho_0}{D_h} |u|\, u\, (L_1 + L_3 - x) \text{ for } x \in [L_1; L_1 + L_3] \tag{5.23}$$

$$P_{pressurizer}(x) = P_p \text{ for } x \in [L_1 + L_3; L_1 + L_3 + L_4] \tag{5.24}$$

$$P_{pressurizer}(x) = P_p + f_w \frac{\rho_0}{D_h} |u|\, u\, (L_1 + L_3 + L_4 - x) \text{ for } x \in [L_1 + L_3 + L_4; L_1 + L_2] \tag{5.25}$$

where L_3 and L_4 are the lengths given on Fig. V-3, P_p is the pressure in the pressurizer, ρ_0 the density and D_h is the hydraulic diameter. At steady-state, the pressurizer does not exchange any mass and energy with the loop. As a result, the velocity u_p defined in section 2, equals zero. This condition is important since it allows computing an analytical solution.

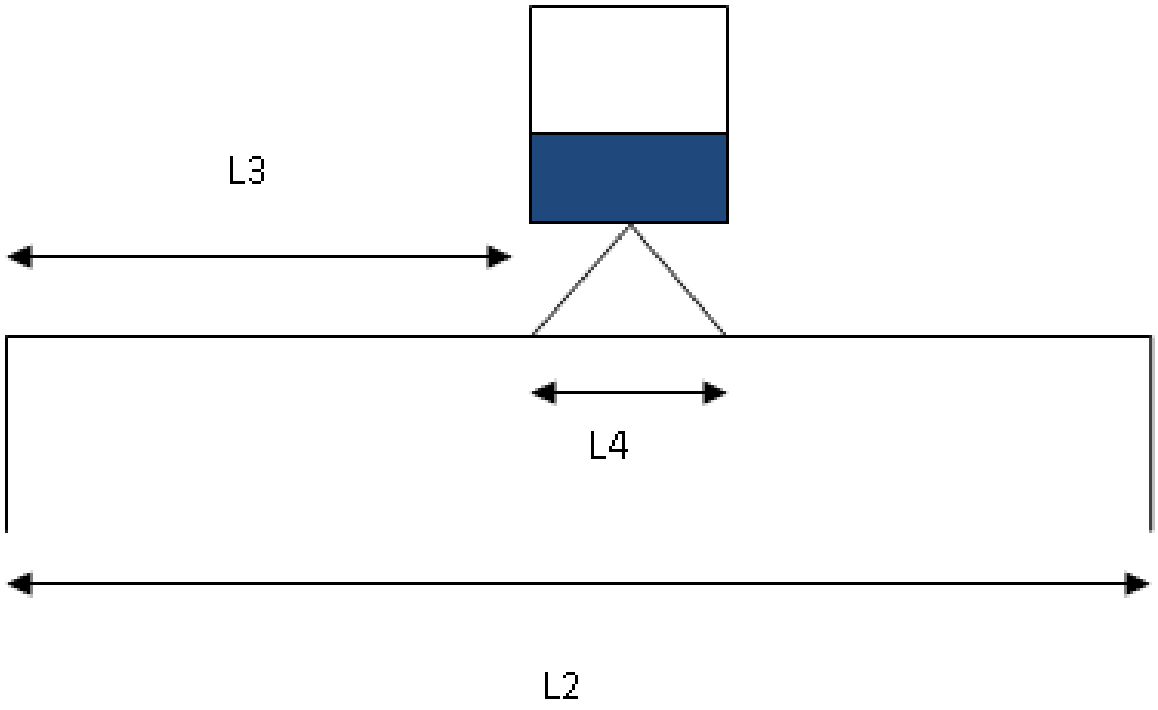

Fig. V-3. Uniform pressurizer used in the code.

Along the pump, the temperature and pressure profiles are (Fig. V-4 is a representation of the uniform pump over the length L_6 in the code) :

$$T_{pump}(x) = T_{sg}(x = 2L_1 + L_2) \tag{5.26}$$

$$P_{pump}(x) = P_{sg} + f\frac{\rho_0}{D_h}|u|\,u\,(2L_1 + L_2 - x) \;\text{ for } x \in [2L_1 + L_2; 2L_1 + L_2 + L_5] \tag{5.27}$$

$$P_{pump}(x) = P_{sg} - L_5 f_w \frac{\rho_0}{D_h}|u|\,u + \left(\rho_0 g h - f_w \frac{\rho_0}{D_h}|u|\,u\right)(2L_1 + L_2 + L_5 - x)$$
$$\text{for } x \in [2L_1 + L_2 + L_5; 2L_1 + L_2 + L_6] \tag{5.28}$$

$$P_{pump}(x) = P_{sg} - (L_5 + L_6)\, f_w \frac{\rho_0}{D_h}|u|\,u + f\frac{\rho_0}{D_h}|u|\,u\,(2L_1 + L_2 + L_5 - x)$$
$$\text{for } x \in [2L_1 + L_2 + L_6; 2L_1 + 2L_2] \tag{5.29}$$

where L_5 and L_6 are lengths given in Fig. V-4. The temperature is constant in both horizontal legs of the loop. The pressure drop is due to the friction forces and the pump and varies linearly.

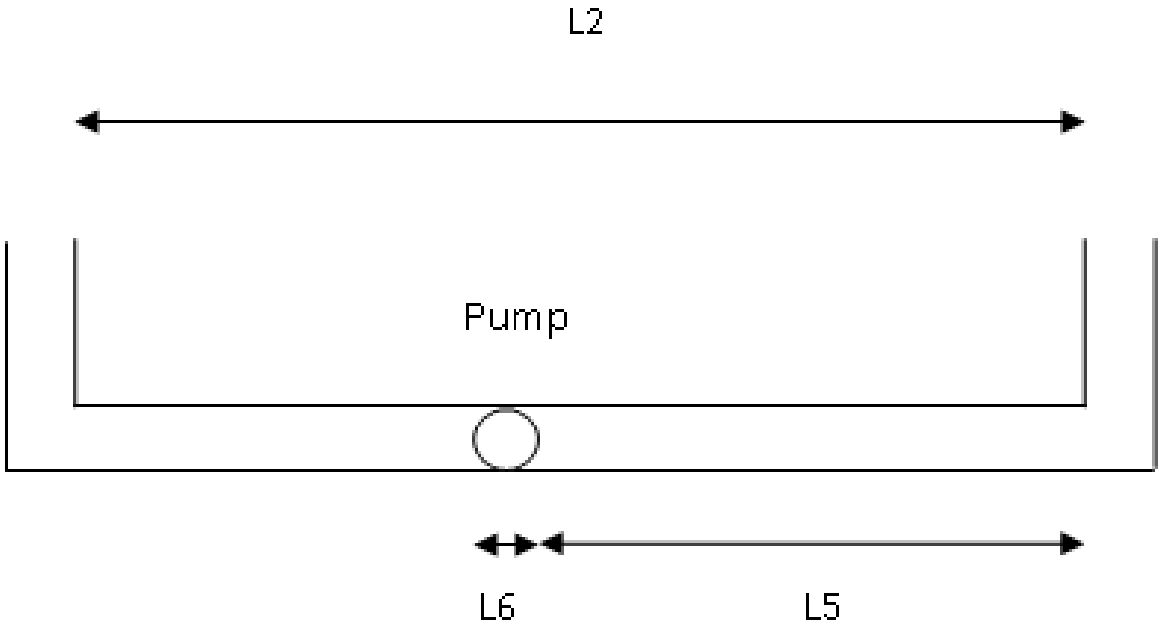

Fig. V-4. Pump used in the code.

We notice above that the temperature profiles along the core and the steam generator are functions of the parameters l_{core} and l_{sg} ,respectively; these parameters also depend on the velocity. If the velocity is high (forced convection), the term $\frac{x}{l_{core}}$ is small compared to one so that the exponential function can be approximated using a Taylor series development:

$$e^{-x} \approx 1 - x \tag{5.30}$$

As a result, in the case of forced convection, the temperature profile is almost linear. If the buoyancy forces dominate (natural convection), the velocity is smaller than the previous case and $\frac{x}{l_{core}}$ is no longer small compared to 1. Thus, the temperature

profile will not be linear.

Having determined the analytical solution for the temperature and the pressure, a mesh refinement study can be performed. The spatial grid size is divided by two for each new simulation. The spatial grid size for the coarsest grid is $\Delta x = 2$ meters. The Fig. V-5 shows the numerical solution for different grid sizes and the exact solution. Fig. V-6 shows the error versus space grid size.

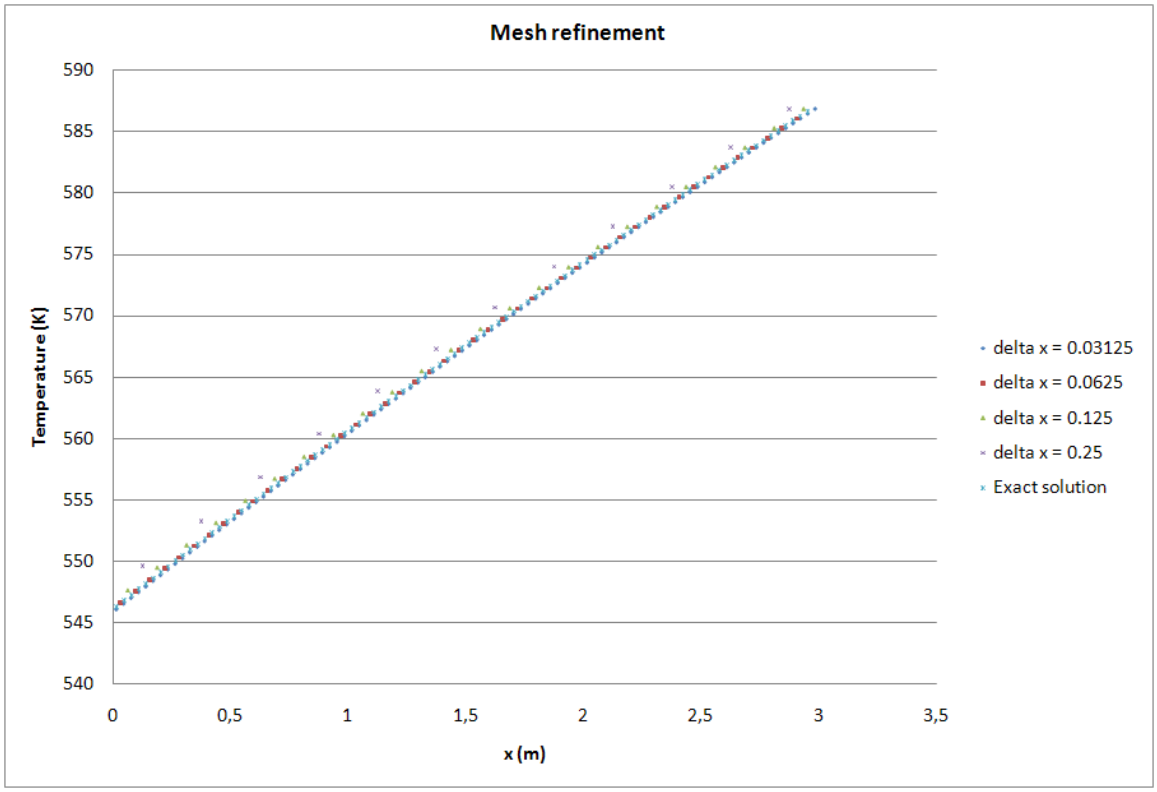

Fig. V-5. Mesh refinement.

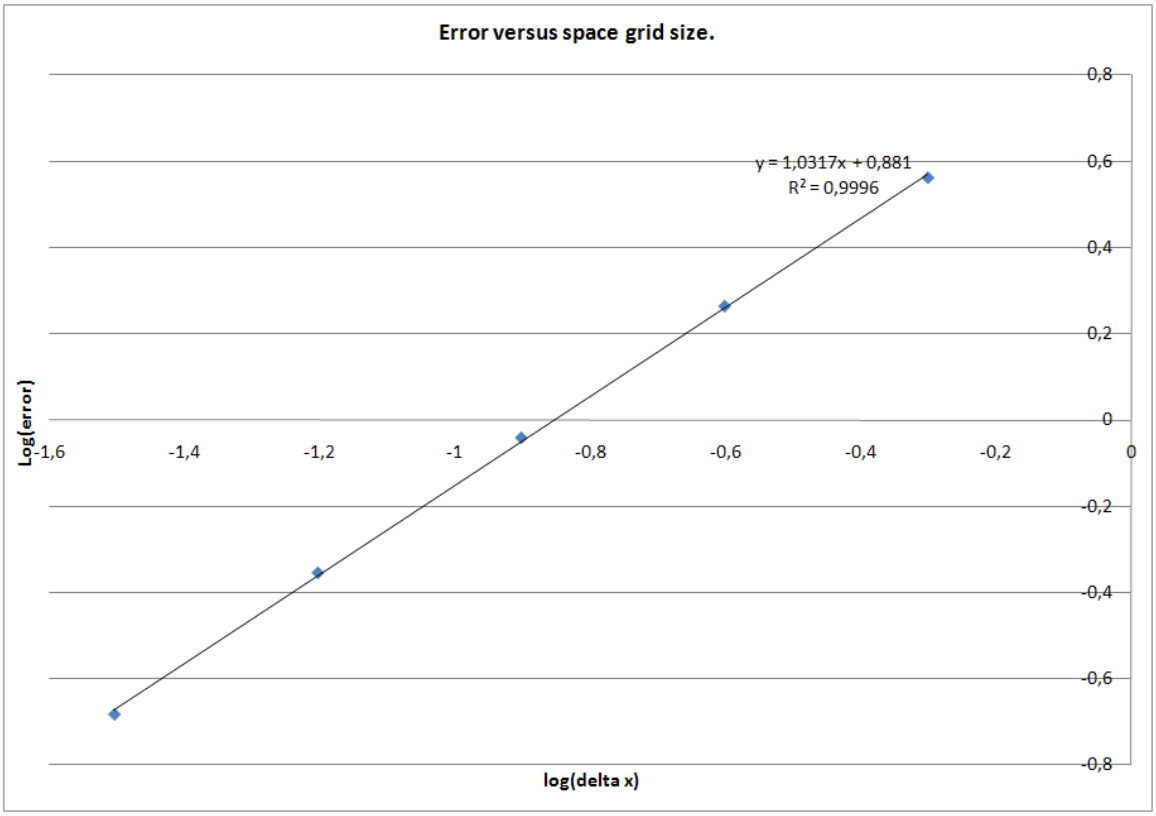

Fig. V-6. Error versus space grid size.

As expected, as the mesh is refined, the numerical solution converges to the exact solution (in yellow on Fig. V-5). On Fig. V-6 the slope of the straight line is 1.0317 as expected for a first-order code.

CHAPTER VI

PRESSURIZED WATER REACTOR (PWR) EXAMPLE

This chapter deals with light water reactors. PWR characteristics are used in the model, and results obtained with compressible and incompressible models are provided in order to compare them at steady-state and for a pump coast down transient. A sensitivity analysis is also performed for the friction factor. A last section will deal with uncertainty study carried out for the density, the heat transfer coefficient, the viscosity and the heat capacity, based on Polynomials Chaos theory.

A. Characteristic data for PWRs

The simulation model possesses some input parameters that can be changed in order to match the flow data pertinent to the reactor under consideration. Here, we present the parameters employed for a PWR. The steady-state core inlet and outlet temperatures are 548 K and 588 K respectively. The Equation Of State is linearized at the following points: $P_0 = 15.5\ MPa$ and $T_0 = 569\ K$. All physical parameters of the water are taken at this state point (e.g., ρ_0, viscosity, and heat capacity). The heat transfer coefficients are set in order to match the inlet and outlet temperatures in the core of $548K$ and $588K$ respectively. The pump strength is set to result in an average velocity of the order of 5 $m.s^{-1}$ in the loop. The core and steam generator temperatures are set to $T_{wcore} = 800\ K$ and $T_{wsg} = 373\ K$. All these inputs can be changed to match different types of PWR reactors. Some complementary parameters are given in Table VI-I.

Table VI-I. PWR parameters

$Parameters$	$Value$	$Units$
h_{core}	$28.9 \cdot 10^4$	$W \cdot m^2 \cdot K^{-1}$
h_{sg}	$35 \cdot 10^4$	$W \cdot m^2 \cdot K^{-1}$
c	1291.7	ms^{-1}
μ	0.0001280	$Pa \cdot s^{-1}$
$\frac{\partial \rho}{\partial T}$	-0.44	$kg \cdot m^3 \cdot K^{-1}$
T_{wcore}	800	K
T_{wsg}	373	K
P_0	15	MPa
T_0	500	K
D_h	0.020	m
C_v	3218.2	$J \cdot kg^{-1} \cdot K^{-1}$
s_p	10	$none$
$P_{pressurizer}$	15.5	MPa
L_1	3	m
L_2	3	m
L_3	1	m
L_4	0.5	m
L_5	1	m
L_6	0.5	m
A	$L_1 \cdot 1$	m^2

B. Steady-state and transient

1. Steady-state

The steady-state is computed for the compressible and incompressible models. A pseudo-transient is run to reach the initial steady-state. We are interested in both the final steady-state and the transient before the steady-state. A 9-second ramp for the heat source/sink is set. The initial conditions are atmospheric pressure and temperature. The initial velocity is 0.001 $m.s^{-1}$. The following plots, Fig. VI-1, Fig. VI-2, Fig. VI-3 and Fig. VI-4, show the temperature, velocity, density and pressure profiles at steady-state and during the transient.

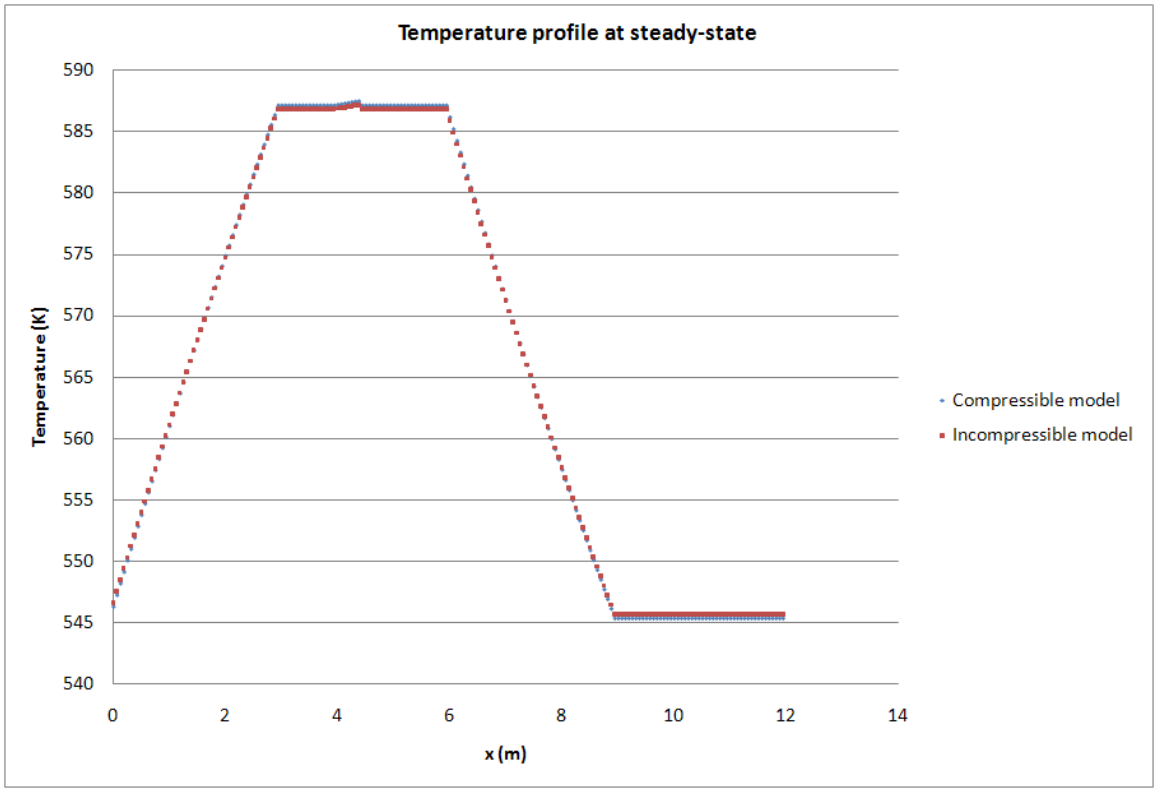

Fig. VI-1. Temperature profile at steady-state (PWR).

The temperature profile in Fig. VI-1 is linear along the core and the steam

generator for both the compressible and incompressible models. In section C, it is shown that the temperature profile is linear for the incompressible model. In the compressible model, the change in density is not very large as shown in Fig. VI-3 so that it is also expected to obtain a linear temperature profile along the core for the compressible model. It is noted that the temperature is constant along the pressurizer and the pump. For the compressible model, the temperature is slightly higher than in the incompressible model. This offset is due to the dilatation of the fluid. A hump, observed on the temperature profile around $x = 2.5$, is due to the pressurizer.

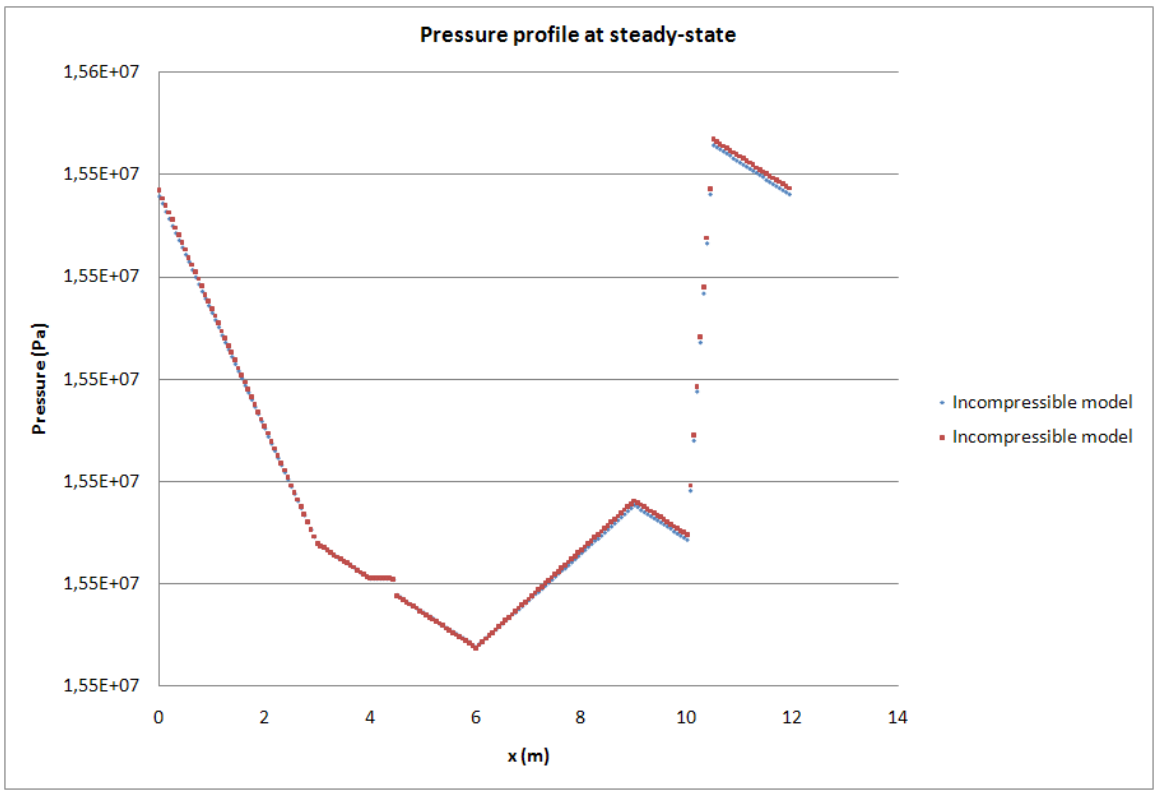

Fig. VI-2. Pressure profile at steady-state (PWR).

In Fig. VI-2, the pressure decreases along the core because of the gravity force and the increase in velocity. Along the upper leg, the pressurizer sets the pressure and a pressure drop is observed because of friction forces. Along the steam generator,

gravity causes the pressure to rise. Fiction forces are not strong enough to cause a pressure drop. Along the lower leg, the pump adds an artificial pressure rise.

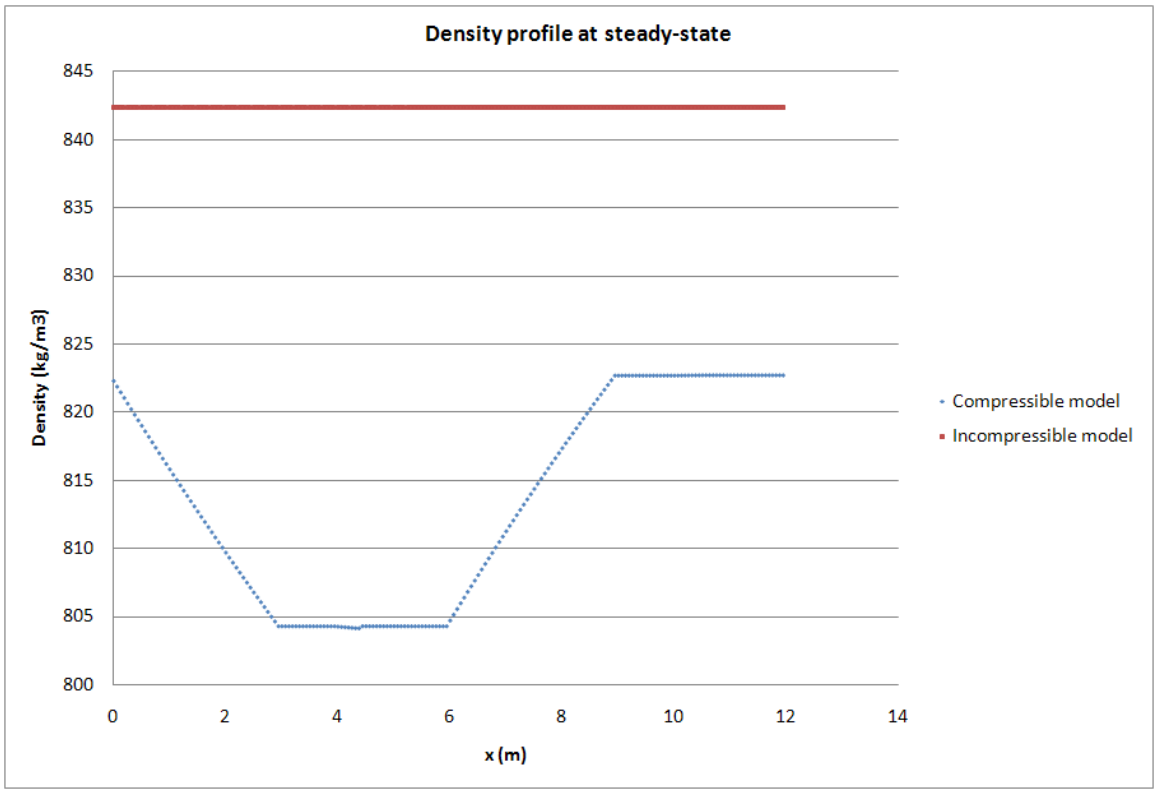

Fig. VI-3. Density profile at steady-state (PWR).

The density (Fig. VI-3) is coupled to the pressure and the temperature through the EOS. The pressure term in the EOS can be neglected in front of the temperature term since the sound speed is of the order of 10^3. As a result, the density will be mainly sensitive to the change in temperature in the system. Then, it is expected to have a density gradient along the core and the steam generator for the compressible model. As the temperature rises, the density decreases. In the incompressible model the density is constant and higher than in the compressible model since it is not temperature-dependent. The density with the Boussinesq correction is not plotted for the incompressible model.

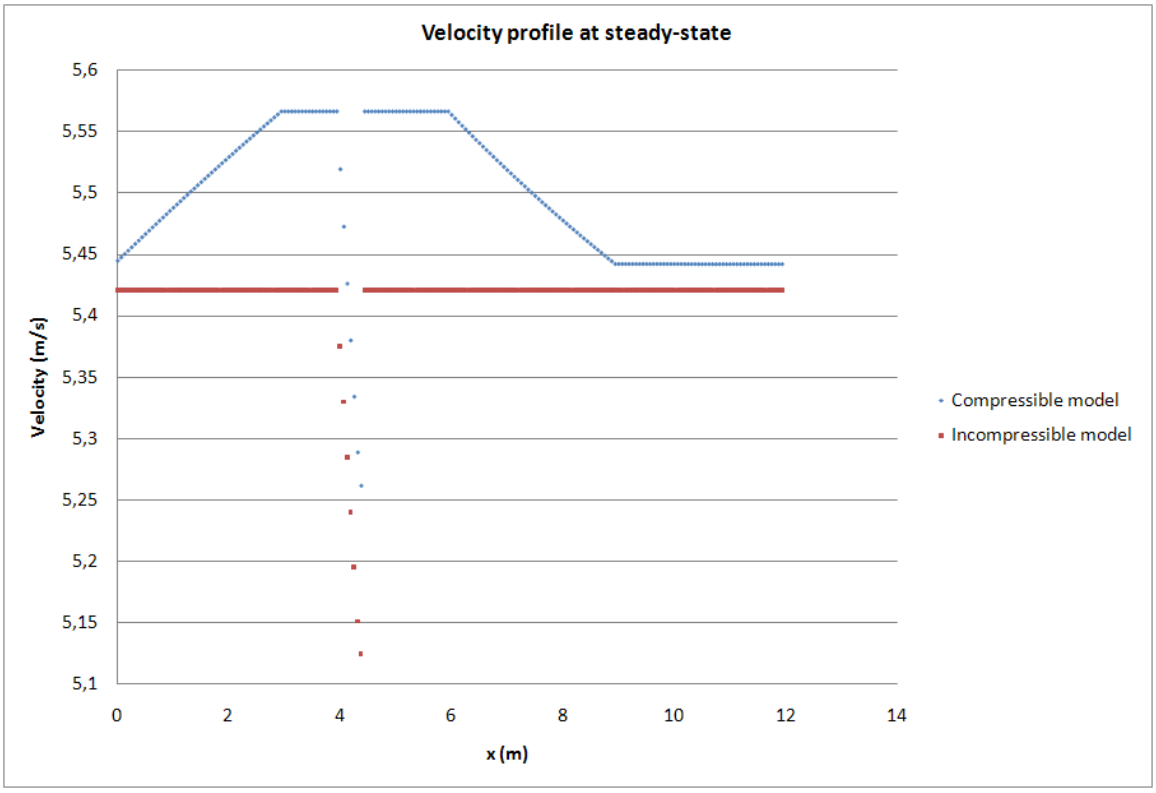

Fig. VI-4. Velocity profile at steady-state (PWR).

In the core, buoyancy forces make the velocity (Fig. VI-4) rise as temperature increases. The inverse phenomena is observed in the steam generator. Since the temperature is held constant in the pressurizer and pump legs, the velocity is also constant. In the case of the incompressible model, the continuity equation $\frac{\partial u}{\partial x}$ requires the velocity to be constant in the loop. This statement is not true along the pressurizer since there is a mass source/sink term in the continuity equation. In Fig. VI-4, a decrease in the velocity is observed because the steady-state is not fully reached.

2. Pseudo-transient to steady-state (with pumps on)

This section aims at describing the pseudo-transient employed to reach steady-state; the pump is on. The following plots, Fig. VI-5 and Fig. VI-6, show temperature and

velocity variations during the transient. The last plot, Fig. VI-7, is the difference between the energy supplied to the fluid (in the core, Q_{in}) and the energy removed from the fluid (in the steam generator, Q_{out}).

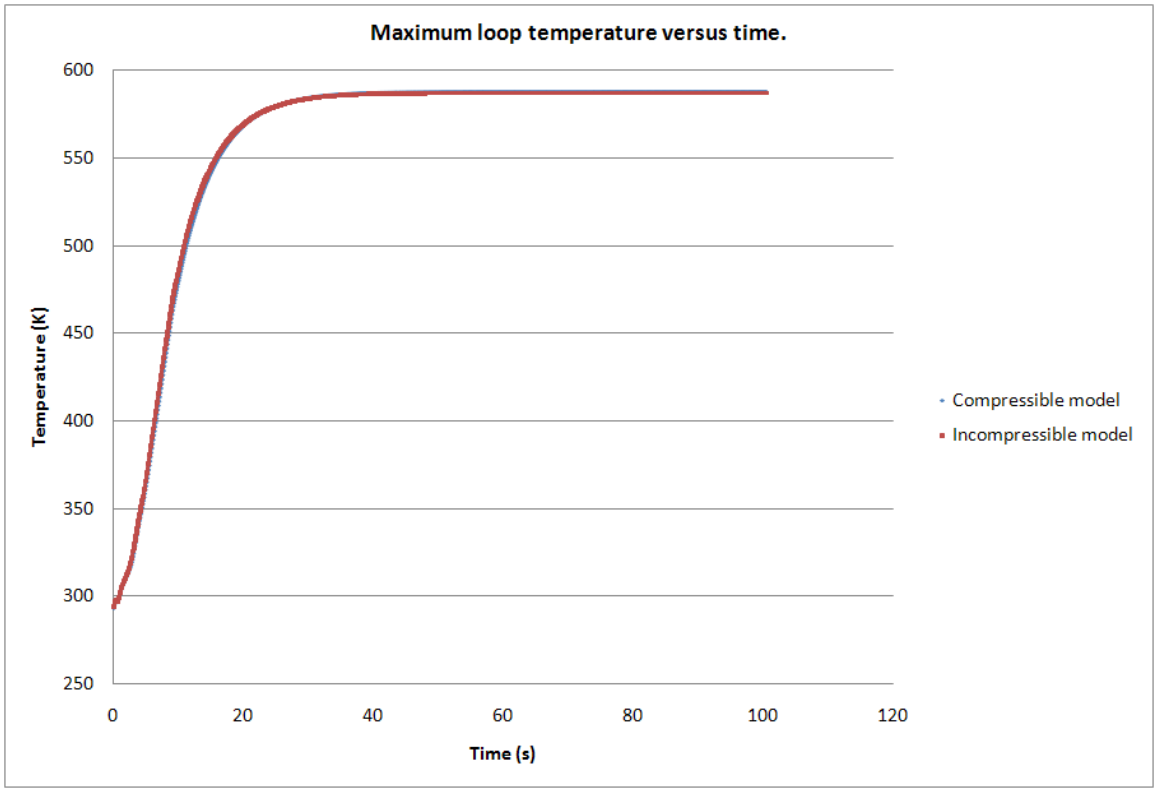

Fig. VI-5. Temperature profile during the transient.

The temperature profiles,Fig. VI-5, using the compressible and incompressible models are very similar.

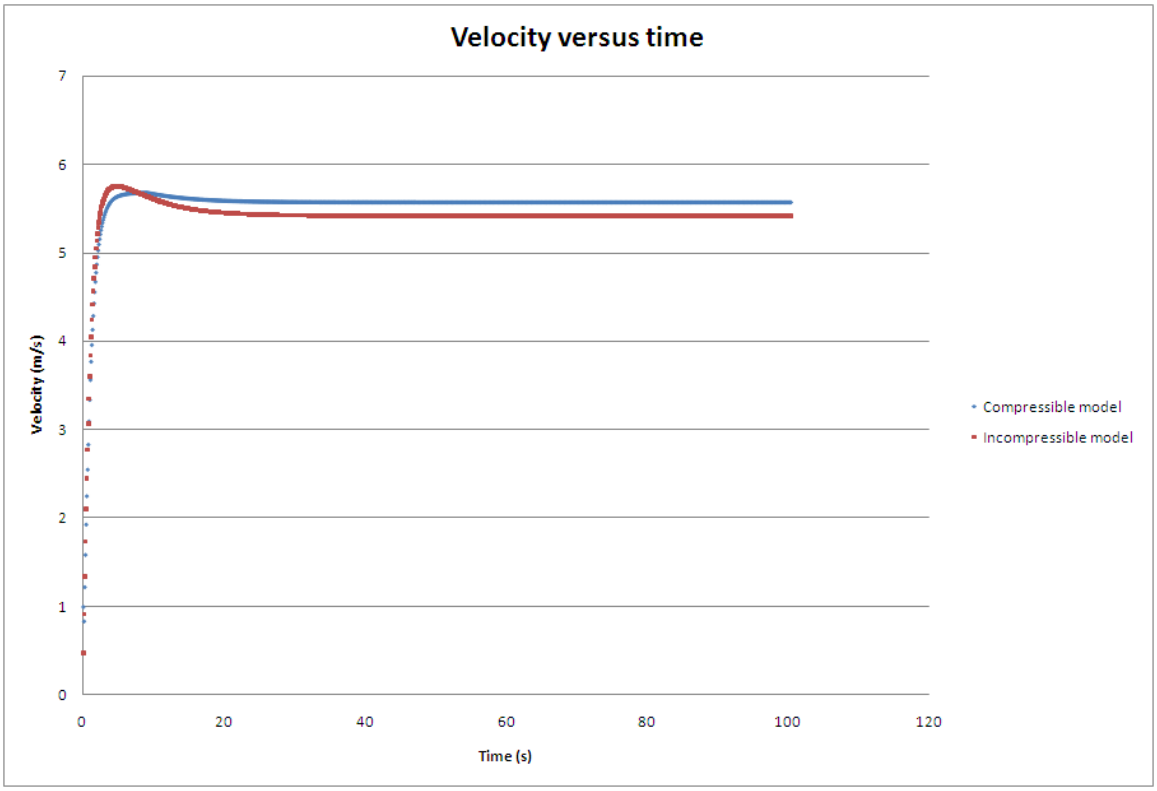

Fig. VI-6. Velocity profile during the transient.

The velocity is a function of the pump strenght and reaches quickly a stead-state value (Fig. VI-6). The steady-state is reached quicker with the incompressible model.

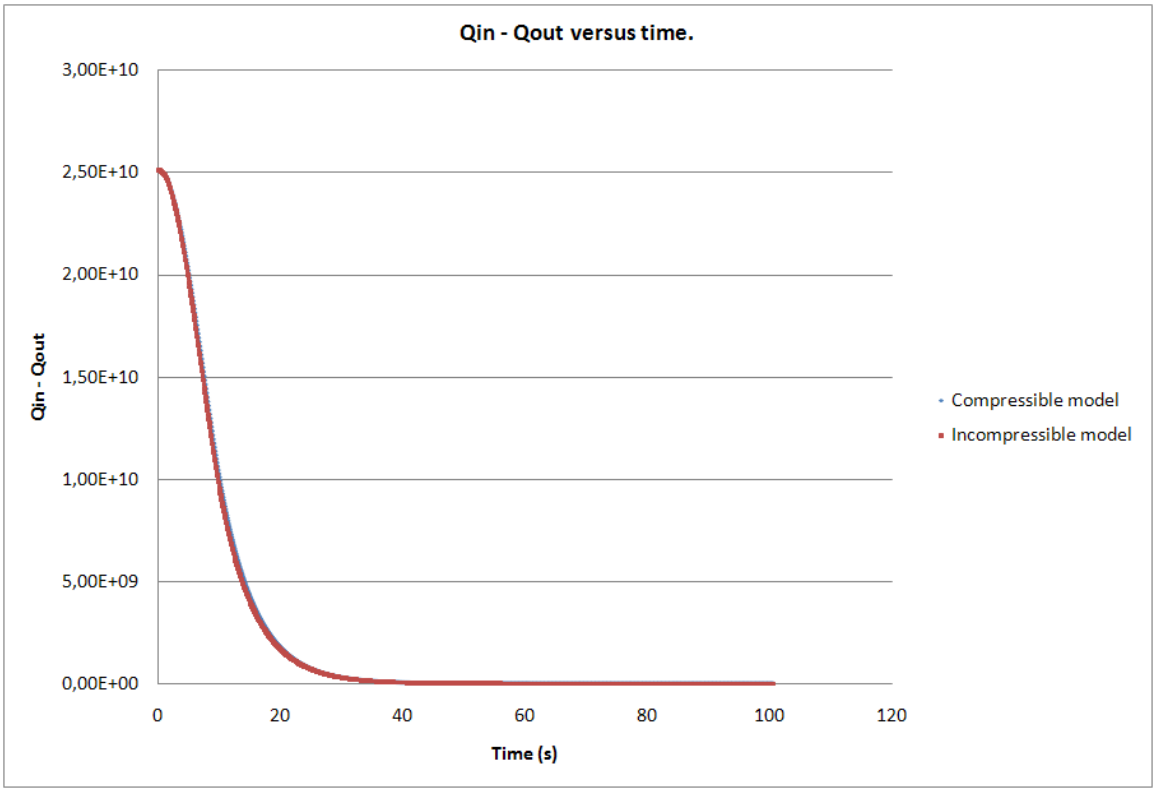

Fig. VI-7. $Q_{in} - Q_{out}$ versus time.

In order to reach steady-state, the system has to balance the energy removed from and supplied to the fluid. The initial temperature is set to $293K$ so that the initial system is far from the steady-state. As a result, the term $Q_{in} - Q_{out}$ is large at the beginning of the transient and decreases afterwards. No major differences are found between the incompressible and compressible models during this pseudo transient (Fig. VI-7).

3. Model uncertainty

The purpose of this study is the uncertainty quantification between compressible and incompressible models. In that regard, it is of interest to plot the change in velocity and density in the system in order to quantify importance of the term $\frac{\partial u}{\partial x}$. In the

incompressible model, the continuity equation leads to $\frac{\partial u}{\partial x} = 0$.

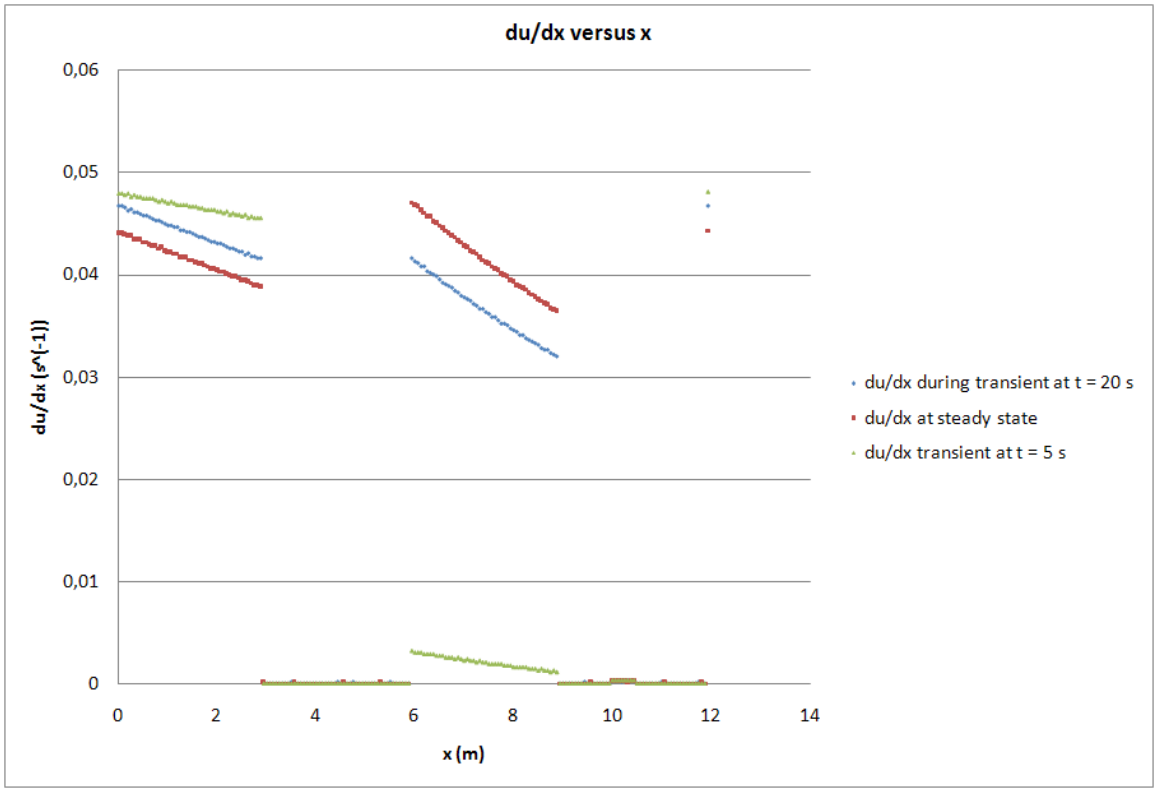

Fig. VI-8. $\frac{\partial u}{\partial x}$ versus x at steady-state.

Fig. VI-8 shows the variation of $\frac{\partial u}{\partial x}$ in the loop for the compressible model at various times during the pseudo-transient ($t = 5s$ and $t = 20s$) and at steady-state. From Fig. VI-8, one can conclude that the term $\partial u/\partial x$ is not larger than 0.05 in the system.

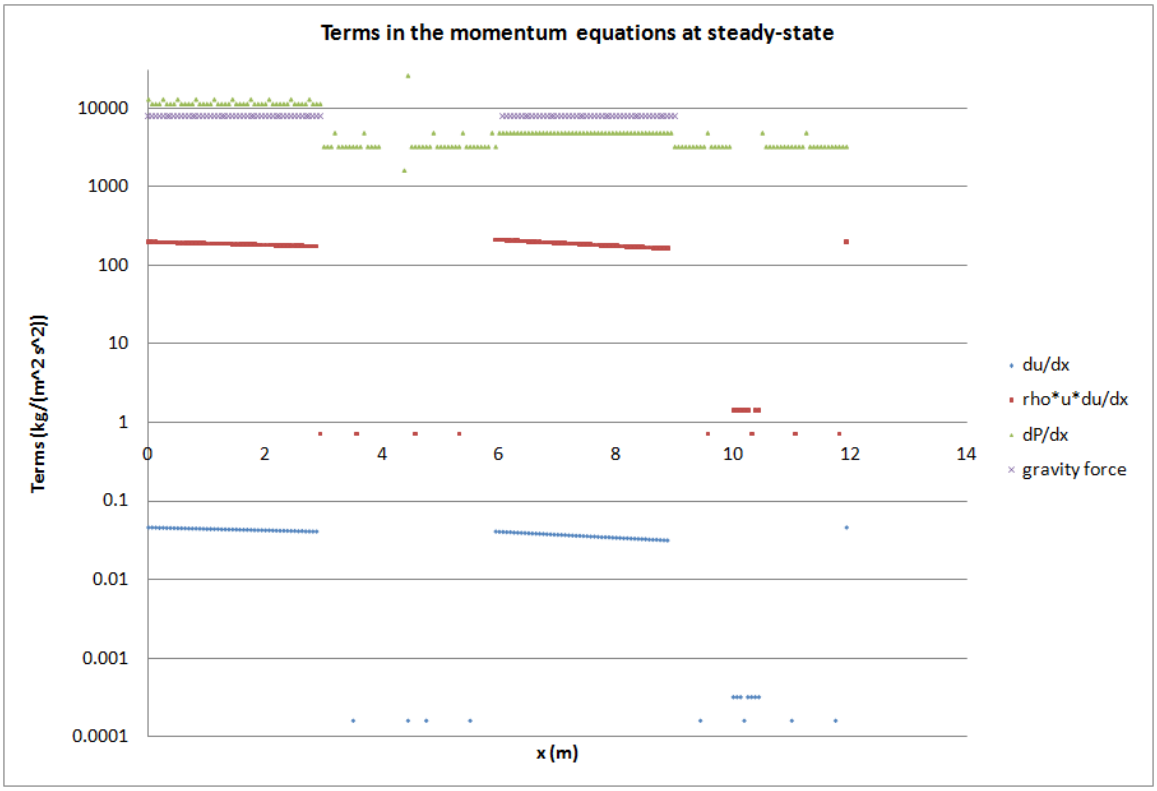

Fig. VI-9. Terms in the momentum equation at steady-state versus x.

More precisely, we want to compare $\frac{\partial u}{\partial x}$ to some terms of the momentum (for instance $\frac{\partial P}{\partial x}$) and energy equation (for instance $P\frac{\partial u}{\partial x}$), both at steady-state and during the transient, in order to determine if the incompressible model is valid.

In Fig. VI-9, the magnitudes of different terms appearing in the momentum equation are compared (on a logarithm scale) for the compressible model. It is obvious that the advection term, $\rho u\frac{\partial u}{\partial x}$ is the smallest, by about three orders of magnitude, and, therefore, can be reasonably neglected for steady-state simulations.

The same comparison was performed for the terms in energy equation, $P\frac{\partial u}{\partial x}$ and $\rho u C_v\frac{\partial T}{\partial x}$, and led to the same conclusions. From Fig. VI-8 and Fig. VI-9 using, the incompressible model seems to be a good assumption since the term $\frac{\partial u}{\partial x}$ is small compared to others terms. In addition, the temperature and pressure profiles are very

similar during the transient with the pump on and at steady-state. In other terms, in the case of forced convection, the incompressible model is a valid approximation to the compressible model in 1D for a PWR application.

C. Study of a transient: pumps turned off

The simulated transient consists of a pump coast-down, where the pump is completely stopped with a ramp of 4 seconds. In this case, buoyancy forces take over to cool down the core. Compressible-flow and incompressible-flow simulations are run with the same compressible steady-state values in order to start with the same amount of energy, mass and momentum. One question arises in doing so: what are the perturbations caused by the compressible-flow initial conditions when running the transient with the incompressible flow option? This question is addressed in Fig. VI-12 (green plot). The transient and the new steady-state (i.e., end of the transient) are given in the next sections.

1. Transient simulations

Fig. VI-10 and Fig. VI-11 show the variations in velocity and temperature as a function of time for the compressible and incompressible models.

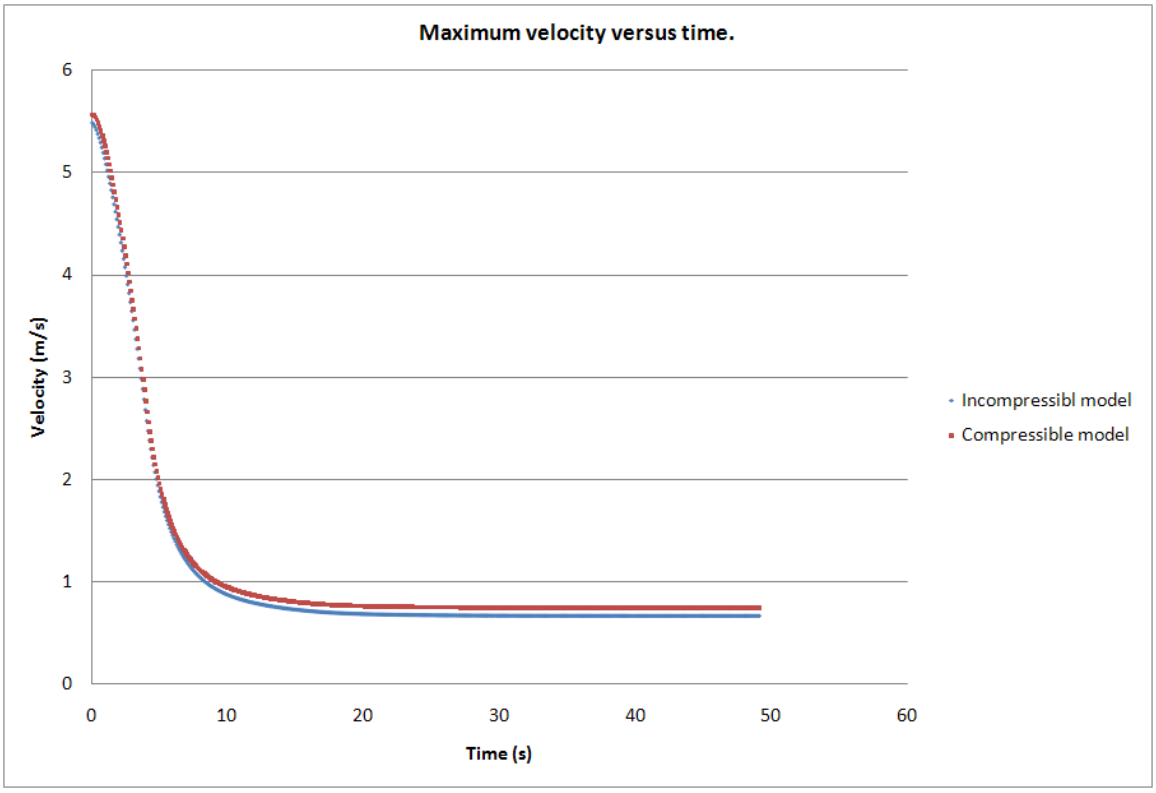

Fig. VI-10. Maximum of velocity versus time during the pump coast down transient.

As the pump strength is decreased (but still not zero), the incompressible and compressible models yield the same velocity. As soon as the pump is fully off, buoyancy forces take over and a change in velocity is observed starting at about 4 seconds. Since the change in density is the driver of the buoyancy forces, the Boussinesq correction is used in the incompressible model (for the compressible model, the density is always pressure- and temperature-dependent) in order to account for the change in density. According to Fig. VI-10, the Boussinesq correction does not seem good enough for the incompressible model since the velocities are not the same between the two models.

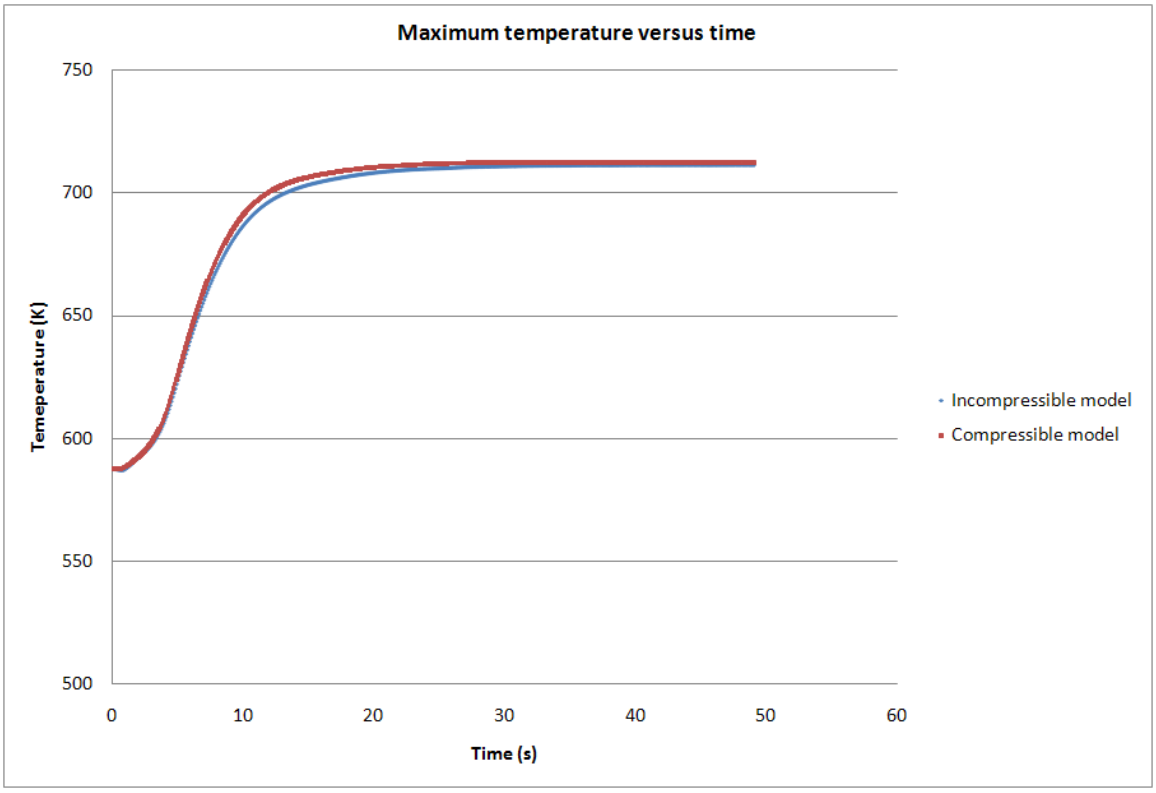

Fig. VI-11. Maximum of temperature versus time during the transient.

At the beginning and at the end (when the steady-state is reached) of the transient, the temperature profiles are identical (Fig. VI-11). The main difference between the two models occurs when the temperature increases rapidly and the pump is fully off. As explained above, a change in velocity is observed; this leads to some modifications in the temperature since temperature and velocity are coupled to each other, when $\frac{\partial T}{\partial t}$ and $\frac{\partial u}{\partial t}$ are large. As it is shown in the section dealing with the mesh refinement, the temperature profile is coupled with velocity.

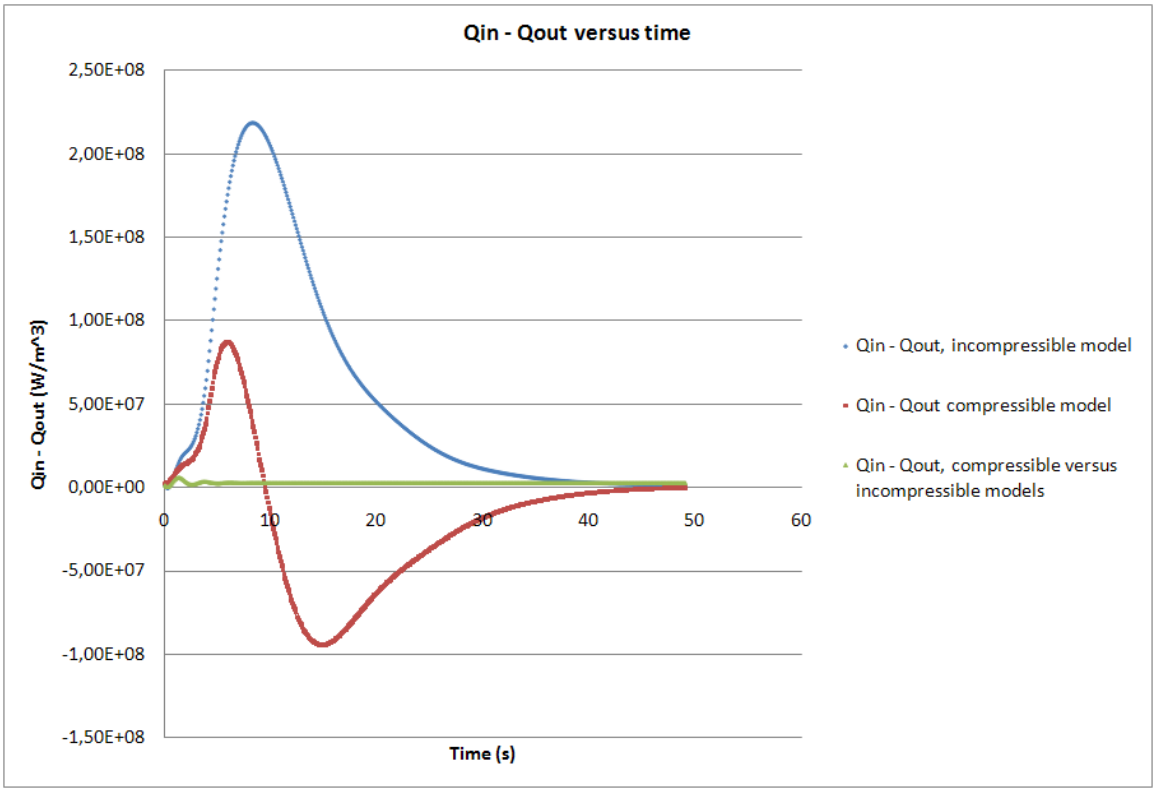

Fig. VI-12. $Q_{in} - Q_{out}$ versus time during the transient.

Fig. VI-12 shows that the energy removed from and supplied to the fluid strongly depends on the compressibility for the pump coastdown transient. In the case of the incompressible model, this quantity is always positive, whereas for the compressible model, $Q_{in} - Q_{out}$ changes sign. It is observed that the same steady-state is reached. The third curve (green plot) in Fig. VI-12 represents the variations of $Q_{in} - Q_{out}$ for a null transient simulation in which the initial conditions are those obtained with the compressible solver but the null transient is computed with the incompressible solver. For a null transient, we would expect to observe no changes. Here, switching between models incurs some variations, but these are small when compared with the ones from the pump coastdown transient. As a result, it can be considered that the modifications due to the impact of steady-state model are not important for this type

of transient.

2. New steady-state after the pump coast down transient

In this section, the temperature, density and pressure profiles are shown in Fig. VI-13, Fig. VI-14 and Fig. VI-15.

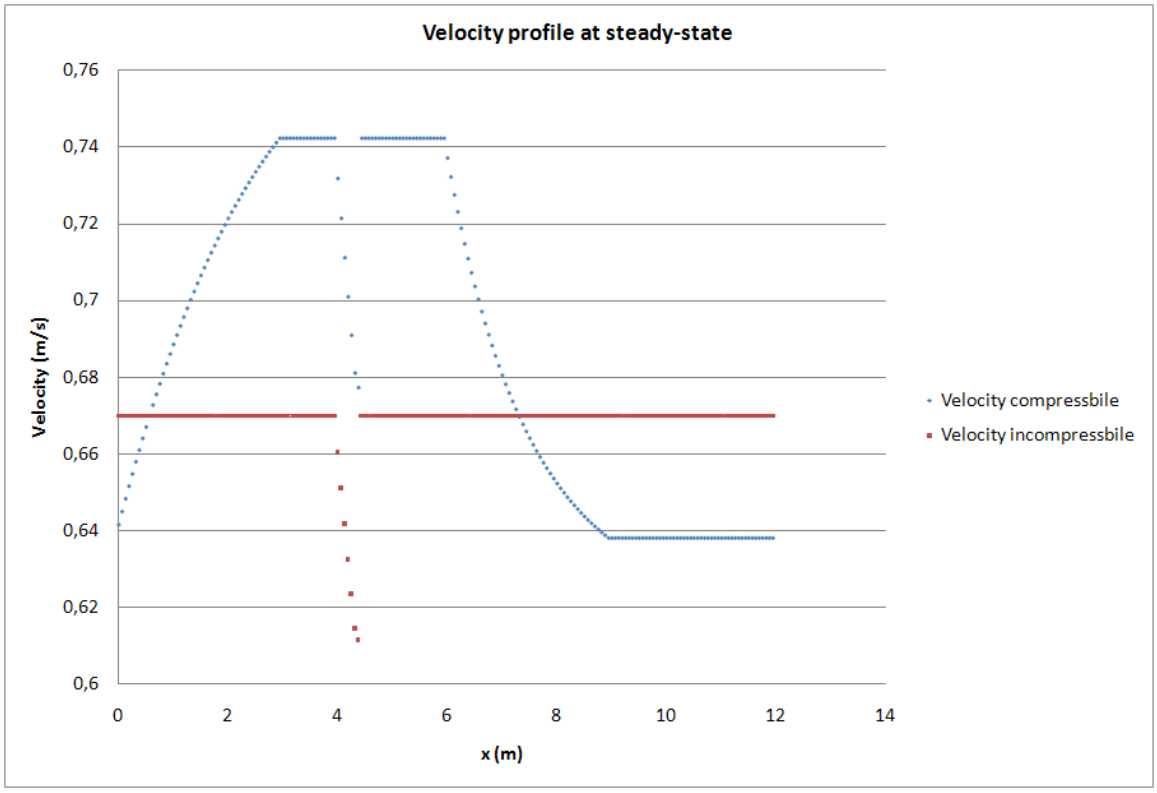

Fig. VI-13. Velocity versus x after the transient.

As expected, the velocity (Fig. VI-13) in the incompressible model is constant at steady-state since $\frac{\partial u}{\partial x} = 0$ as shown in Fig. VI-13. In the compressible model, the velocity is function of space. Along the core, the fluid temperature rises so that the velocity will also increases because of buoyancy forces. Along the steam generator, the inverse phenomena is observed since the fluid is cooled down. Everywhere else, the fluid velocity is constant. It is noted a sharp drop at $x = 4$ is present due to the

pressurizer (the system has not yet reached steady-state). The velocity experiences a change of almost 10% between the compressible and incompressible models whereas the variations was about 2% only in the case of forced convection (see Fig. VI-4).

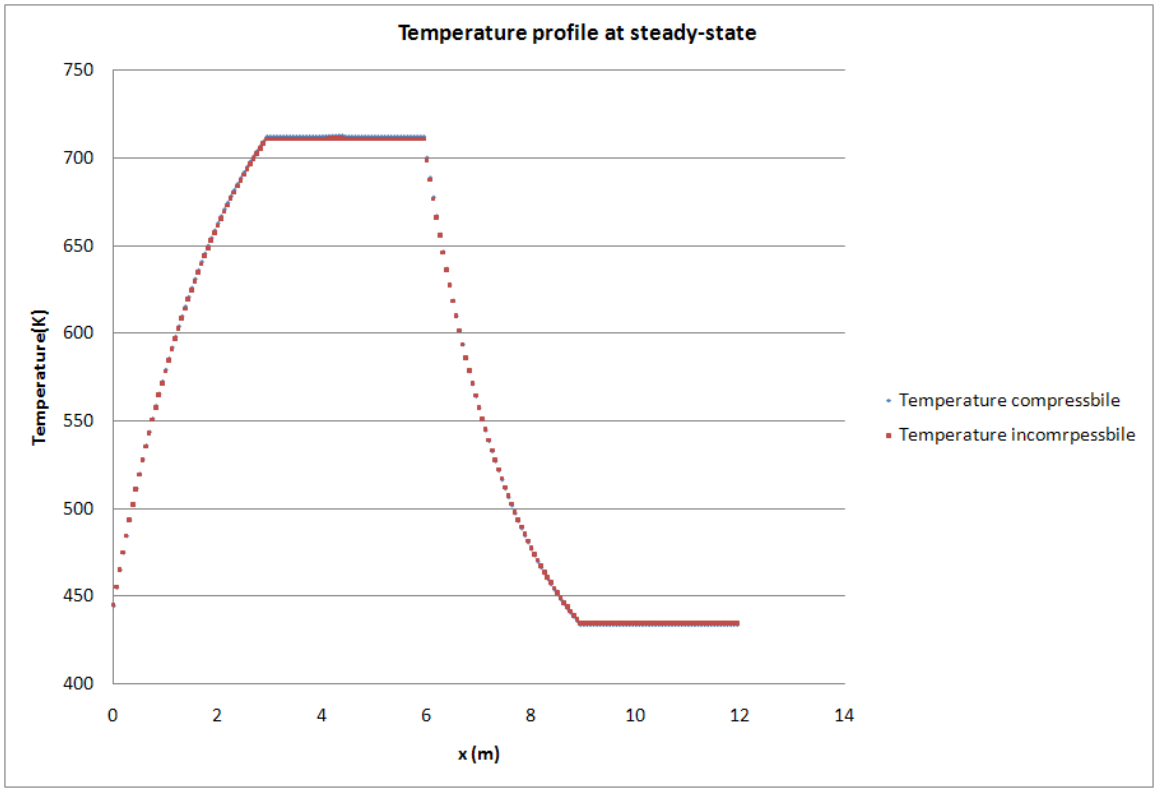

Fig. VI-14. Temperature versus x after the transient.

In Fig. VI-14, it is observed that the temperature profiles are similar to each other at the new steady-state. In addition, the shape matches the analytical solution computed in section C. Since the length scales l_{core} and l_{sg} defined in Eq. (5.16) and Eq. (5.13), are proportional to the velocity, which is smaller in the case of natural convection, the exponential analytical solution can no longer be approximated by a linear function. We clearly observe that the temperature rise and drop are not linear in Fig. VI-14.

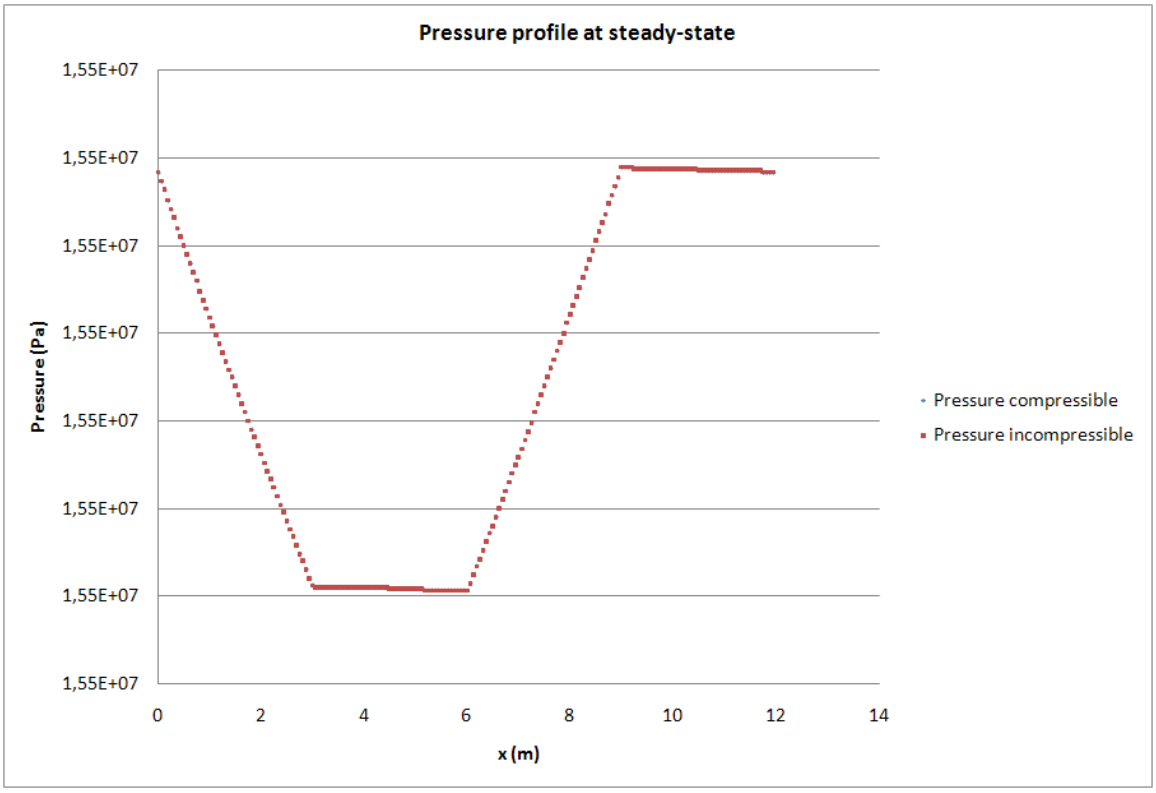

Fig. VI-15. Pressure versus x after the transient.

In Fig. VI-15, the same pressure profiles are obtained at steady-state for both models. At steady-state and under natural convection conditions, the pressure forces are balanced by the gravity and friction forces. In the core and in the steam generator, the pressure gradient is mainly due to gravity forces. In the horizontal legs, the pressure drop is due to friction forces.

3. Model uncertainty

As in the previous section it is interesting to plot the term $\frac{\partial u}{\partial x}$ in order to see how accurate the incompressible assumption is. The following plots show the variations of the velocity at different times during the transient (maximum of $Q_{in} - Q_{out}$) and at the final steady-state.

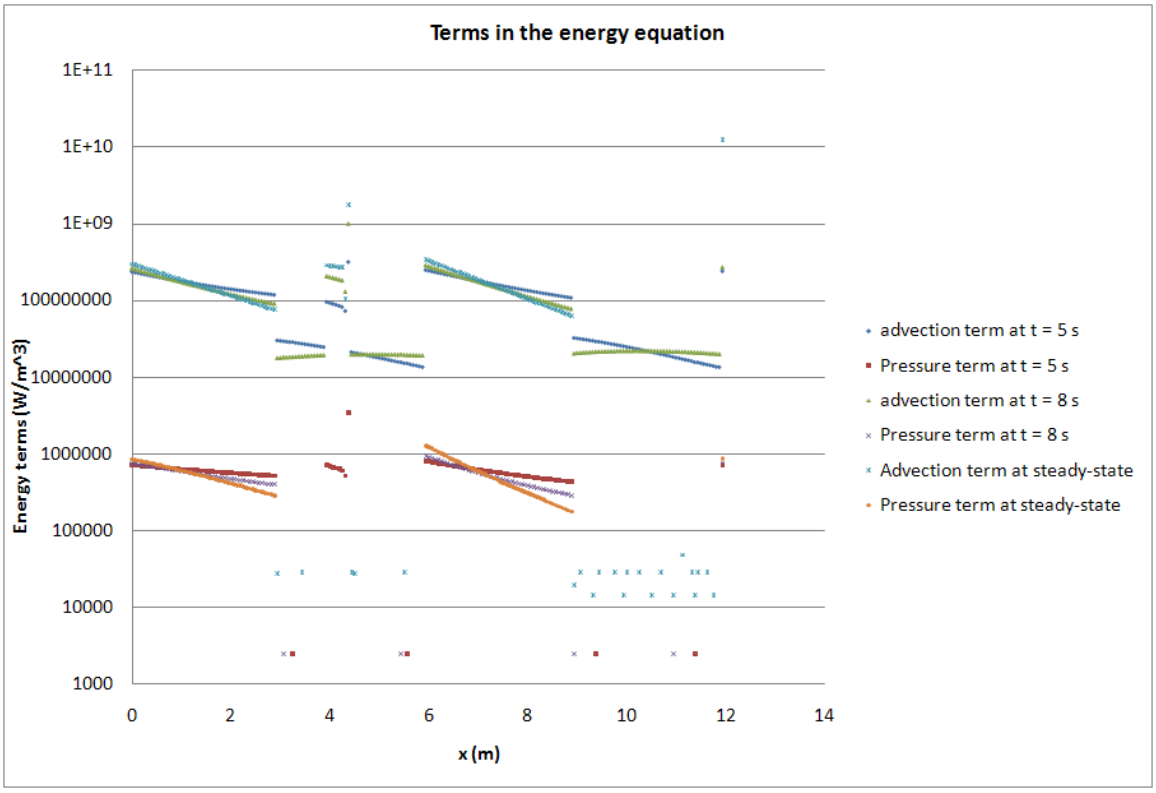

Fig. VI-16. Energy terms in the energy equation versus x at different time of the transient.

Fig. VI-16 shows the variations of the advection ($\rho u C_v \frac{\partial T}{\partial x}$) and the compressible work ($P\frac{\partial u}{\partial x}$) terms at different times ($t = 5s$ and $t = 8s$) during the transient and at steady-state. From Fig. VI-16, it is clear that the pressure term containing the term $\frac{du}{dx}$ cannot be neglected in the energy equation when compared to the advection term. As a result, it seems that the incompressible model cannot be used as an approximation to the compressible model in the case of natural convection.

D. Sensitivity analysis

A sensitivity analysis is performed for the friction coefficient in the friction forces. This parameter usually comes from semi-heuristic experimental data and we as-

sume here it is known with an uncertainty up to 30% . Three simulation are run with a variation of ±5% of the friction parameter. We are mainly interested in the variations of $Q_{in} - Q_{out}$ as a function of time. Fig. VI-17 shows the variation of

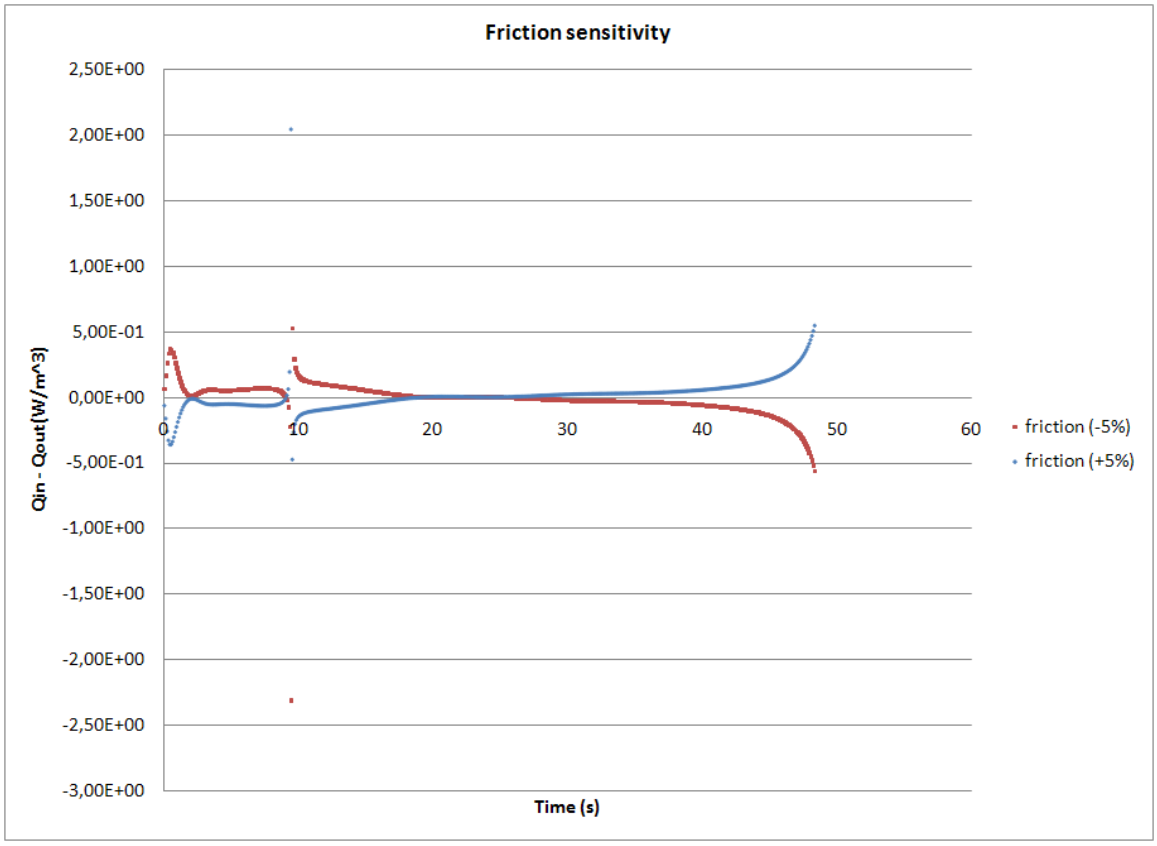

Fig. VI-17. Friction sensitivity.

$(Qin - Qout)_{\pm 5\%} - (Qin - Qout)$ versus time as the plot with the non-modified value of the friction parameter is taken as a reference. We can note that the simulations seem very sensitive to modification of 5% of the friction factor.

E. Polynomials chaos and uncertainties

In this section, we propose to carry out an uncertainty study based on the Polynomials Chaos theory. We begin with a short paragraph dealing with Polynomials Chaos

theory, and present some results related to the uncertainties in the density, ρ_0, the heat transfer coefficient, h, the viscosity, μ, and the heat capacity, C_v for both compressible and incompressible models.

1. Polynomials chaos

An increasing attention is given to uncertainty quantification in scientific computing, due to the increasing complexity of models and the introduction of physical inputs with experimental uncertainties. Polynomials Chaos (PC) theory can be used to analyze the response of complex physical systems to Gaussian distributed random excitation in model parameters and inputs. In other terms, the propagation of uncertainties in the numerical output is studied. A new dimension is added to the system of equations under considerations, namely the stochastic dimension, and the numerical output solution is also expanded in this additional dimension.

In this thesis, we assume that the inputs are Gaussian (some others type of distributions can be used) and given by Eq. (6.1).

$$f(x) = \frac{1}{\sqrt{2\pi}} e^{-\frac{(x-\overline{\mu})^2}{2\sigma^2}} \tag{6.1}$$

where σ and $\overline{\mu}$ are the standard deviation and the mean values, respectively, and x is the variable of interest (ρ_0, μ, h and C_v here).

Then, a prediction of the output is computed using the Hermite polynomials given in Eq. (6.2) (continuous Gaussian random process requires the use of Hermite's polynomials basis [10]).

$$\phi_n(x) = (-1)^n e^{x^2} \frac{d^n}{dx^n} e^{-x^2} \tag{6.2}$$

where n is the order of the Hermite polynomial and x is the variable of interest.

Hermite polynomials form an orthogonal basis with respect to the weight function

$w(x) = e^{-x^2}$, so that they have some interesting properties when used with the inner product of Hilbert space as shown in Eq. (6.3).

$$\begin{aligned} \langle \phi_m(x), \phi_n(x) \rangle &= \int_{-\infty}^{+\infty} \phi_m(x)\phi_n(x)e^{-x^2}dx = 0 \text{ if } n \neq m \\ \langle \phi_n(x), \phi_n(x) \rangle &= \int_{-\infty}^{+\infty} \phi_n(x)\phi_n(x)e^{-x^2}dx = n!\sqrt{2\pi} \end{aligned} \tag{6.3}$$

In this thesis, we consider the temperature in the node at the bottom of the core to be the output of interest. A quadratic Hermite expansion is employed. The output is projected on the Hermite's basis and is called prediction. Since we make the choice of varying two parameters simultaneously, the output prediction, g, is of the type given in Eq. (6.4).

$$g(x_1, x_2, x_3, x_4) = c_0 + \sum_{i=1}^{4} c_i^{(1)} x_i + \sum_{i=1}^{4} c_i^{(2)} \left(x_i^2 - 1\right) + \sum_{i=1}^{3} \sum_{j=i+1}^{4} c_{ij} x_i x_j \tag{6.4}$$

where c_0, $c_i^{(1)}$, $c_i^{(2)}$, and c_{ij} are the coefficients of the expansion and are computed using the orthogonal properties of the Hermite polynomials, x_1, x_2, x_3 and x_4 are the parameters of interest, and $g(x_1, x_2, x_3, x_4)$ is the output distribution (the temperature in this thesis).

The formula used to compute the coefficients c_i is the following and can be derived by using the orthogonality relation for Hermite polynomials:

$$c_i = \frac{\left\langle g(\vec{x}), \phi_i(\vec{x}) \right\rangle}{\left\langle \phi_i(\vec{x}), \phi_i(\vec{x}) \right\rangle} = \int_{-\infty}^{+\infty} dx_1 \int_{-\infty}^{+\infty} dx_2 e^{-\frac{x_1^2+x_2^2+x_3^2+x_4^2}{2}} g(x_1, x_2, x_3, x_4)\phi_i(x_1, x_2, x_3, x_4) \tag{6.5}$$

where $\vec{x}$ is the input vector of coordinates x_1 and x_2. $\langle \cdot, \cdot \rangle$ is defined as the inner product in the Hilbert space.

A Gaussian quadrature is used to compute the coefficients c_i given in Eq. (6.5). As a result, it is required to run some simulations in order to get the values of the output for a given combination of inputs. Since, the expansion is of second order, it

is only required to have three quadrature points for each variable. The quadrature points and the corresponding weights are given in Table VI-II.

Table VI-II. Quadrature points, x_i, and associated weight, w_i for Hermite polynomials

Quadrature points, x_i	Weight, w_i
0	$\frac{8}{9}$
$\sqrt{\frac{3}{5}}$	$\frac{5}{9}$
$-\sqrt{\frac{3}{5}}$	$\frac{5}{9}$

As soon as the output is known for each combination of inputs, the coefficients c_i can be computed. Then, the prediction function given in Eq. (6.4) is fully known and a Monte-Carlo process is run in order to get the shape of the output distribution. By using the orthogonality, we can show that the mean, $\bar{\mu}$, and the variance, σ^2, are given by the following relations:

$$\langle g(x_1, x_2, x_3, x_4), 1\rangle = \mu = c_0 \tag{6.6}$$

$$\begin{aligned}\sigma^2 &= \langle g(x_1, x_2, x_3, x_4), g(x_1, x_2, x_3, x_4)\rangle - \langle g(x_1, x_2, x_3, x_4), 1\rangle^2 \\ &= \sum_{i=0}^{m} c_i^2 \left\langle \phi_i(\vec{x}), \phi_i(\vec{x})\right\rangle - c_0^2 \end{aligned} \tag{6.7}$$

where m is the number of coefficients (here $m = 15$).

2. Results

We present some results obtained by using the PC method. The propagation of the uncertainties is investigated for both the compressible and incompressible models in the case of a PWR under natural and forced convection. Four inputs parameters are assumed having a Gaussian distribution: the density ρ_0, the viscosity μ, the heat transfer coefficient h and the heat capacity C_v. The standard deviation is taken to

be 10% of the mean value for all four parameters. The mean value and the standard deviation are analysed and discussed for each case studied. The first paragraph deals with the study of the propogation of the uncertainty in the case of forced convection for both the compressible and incompressible models. In a second paragraph, the same study is performed but in the case of natural convection. The output of interest, $g(x_1, x_2, x_3, x_4)$, is the temperature of the cell located at the inlet of the core.

In section B, it was shown that the compressible and incompressible models yield the same transient and steady-state under forced convection. As a result, it is not expected to have any major differences in the mean and variance values of the output distribution for the compressible and incompressible models. Fig. VI-18 and Fig. VI-19 show the distribution of the temperature as the inputs vary at the time $t = 15s$ (during the pseudo-transient).

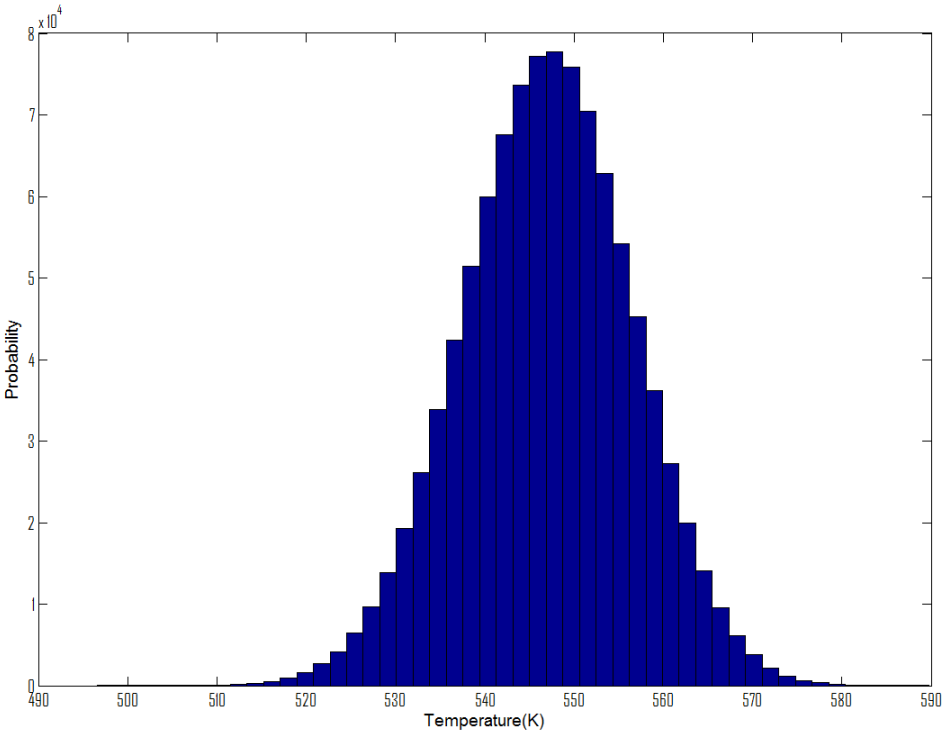

Fig. VI-18. Distribution of the output for the compressible model under forced convection.

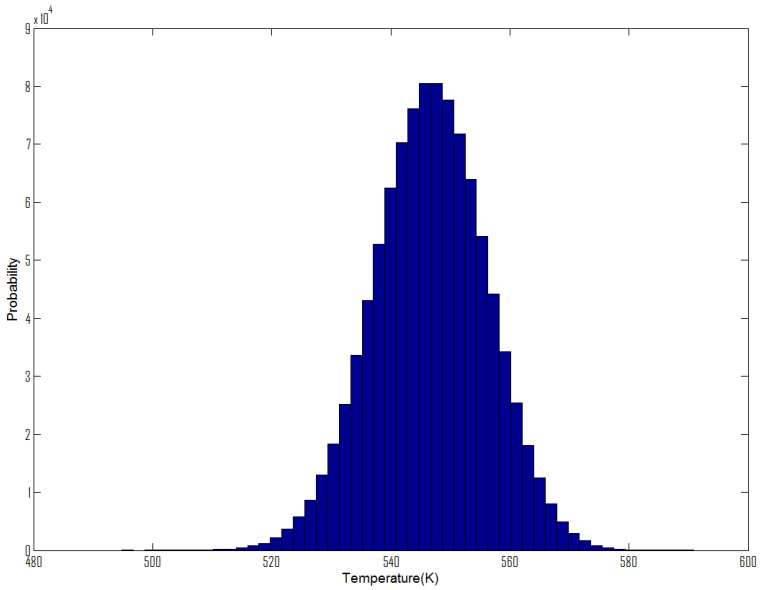

Fig. VI-19. Distribution of the output for the incompressible model under forced convection.

In Fig. VI-18 and Fig. VI-19, we can see that the distribution of the output for the compressible model is very similar to the one of the incompressible model. The means and variances are: $\mu = 546.64K$, $\sigma = 9.43K$, and, $\mu = 546.94K$, $\sigma = 9.54K$ for the compressible and the incompressible models, respectively. The standard deviation is 1.6% of the mean value and is to be compared to the standard deviation of the input that was 10% of the mean value. These results show that the compressible and the incompressible models yield the same output distribution with the same mean and standard deviation. In addition, the numerical simulation is not very sensitive to a change in the input values under forced convection since the standard deviation of the output is only of 1.6%.

Fig. VI-20 shows the distribution of the temperature at the time $t = 9s$ for the compressible and the incompressible models. This time corresponds to the maximum of the plots $Q_{in} - Q_{out}$ of the incompressible model given in Fig. VI-12.

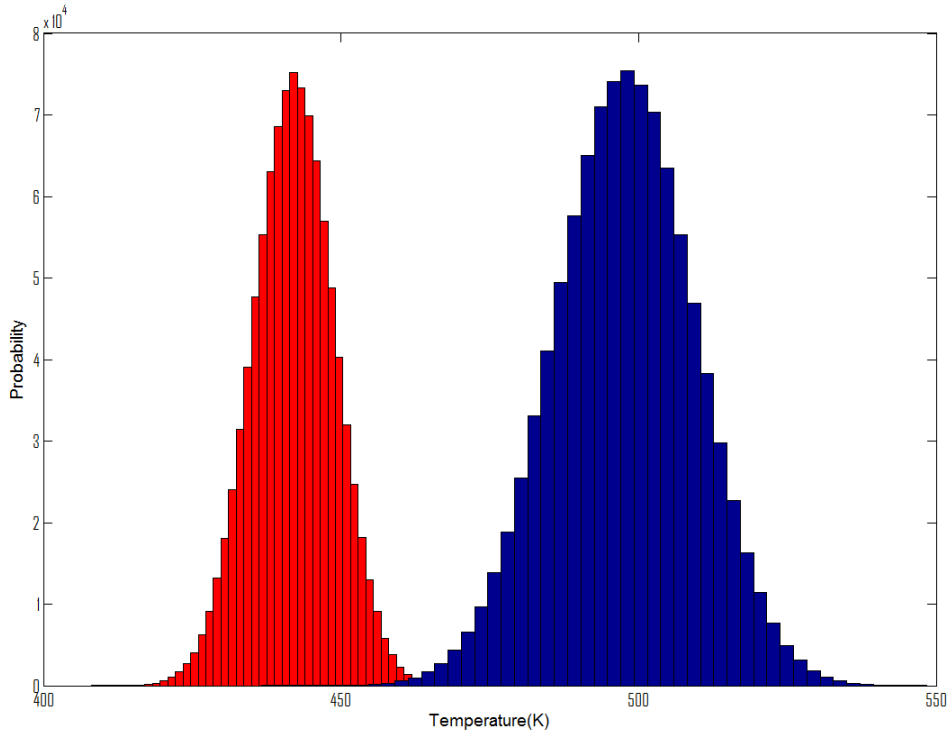

Fig. VI-20. Distribution of the temperature for the compressible (right plot) and the incompressible (left plot) models under natural convection.

In Fig. VI-20, we can see that the distribution of the temperature are very different. We can note a common part between the two plots. As a result, for a given combination of two terms, the compressible and the incompressible models yield the same temperature. For the compressible model (right plot), the mean and standard deviation are $497.60K$ and 11.4, respectively. In the case of the incompressible model, the mean and standard deviation are $442.02K$ and 6.85, respectively. The standard deviations correspond to 2.2% and 1.6% of the mean value for the compressible and the incomressible models, respectively. It is also interesting to compute the difference of the means noted $\delta = 55.56K$ between the two models. In other terms, by shifting the incompressible model answer by δ, we obtain the distribution of the compressible

model but with a different standard deviation.

This study shows that in the case of forced convection, the distribution of the temperature is the same for the compressible and the incompressible models with the same mean and standard deviation. Under natural convection, the mean and standard deviation values are different. The two plots, in Fig. VI-20, have a common part so that for a given combination of inputs, the both models yield the same temperature. Further studies are required to determine if this statement is true for all cells of the loop or just only for some of them.

Future work could include the study of the dependence in time and space of the δ value in order to generate a correcting term for the temperature profile of the incompressible model. From the study above it is still possible to sketch the variations of δ as a function of time for this particular cell of the loop. Since, both simulations start from and end up with the same steady-state, the δ values should be null at this particular times. During the transient, δ will change, reach a maximum, and then decrease.

CHAPTER VII

HIGH TEMPERATURE GAS REACTOR (HTGR)

This chapter aims at presenting some results relative to the Gas Reactor. We are interested in comparing Darcy's law (Eq. (3.34)) to the full momentum equation (Eq. (3.16)) that corresponds to the compressible model (in the remainder of this chapter, the full momentum equation will be referred to as the compressible model). As in Chapter VI, a steady-state is obtained with the pump turned on. Then, the pump is turned off and the resulting transient and the final steady-state are studied.

A. Characteristics data of the HTGR

As in the case of the PWR, the inputs are changed in order to match the characteristics of the HTGR. In this type of reactor, the input and output temperatures are 510 and 935 degrees Kelvin. The velocity is of the order of 50 $m.s^{-1}$ and the flow is reversed compared to a PWR reactor (the velocity will have a negative sign in this case). The Equation Of State is linearized at the following points: $P_0 = 9\ MPa$ and $T_0 = 800$ Kelvin. All physical parameters are taken at this state point (i.e., the viscosity, the heat capacity and ρ_0). The heat transfer coefficients are adjusted in order to match the input and output temperatures in the core of 510 and 935 degrees Kelvin respectively. The pump strength in set to -100 in order to obtain a velocity close to 50 $m.s^{-1}$. The core and steam generator temperatures are set to 1000 and 373 degrees Kelvin, respectively. Some further paramaters relative to the HTGR are given in Table VII-I.

Table VII-I. HTGR parameters

$Parameters$	$Value$	$Units$
h_{core}	$20 \cdot 10^4$	$W \cdot m^2 \cdot K^{-1}$
h_{sg}	$13 \cdot 10^4$	$W \cdot m^2 \cdot K^{-1}$
c	667	ms^{-1}
μ	$3.95 \cdot 10^{-5}$	$Pa \cdot s^{-1}$
$\frac{\partial \rho}{\partial T}$	-0.034	$kg \cdot m^3 \cdot K^{-1}$
T_{wcore}	1000	K
T_{wsg}	373	K
P_0	9	MPa
T_0	800	K
D_h	0.20	m
C_v	$1.82 \cdot 10^3$	$J \cdot kg^{-1} \cdot K^{-1}$
s_p	-100	$none$
$P_{pressurizer}$	9	MPa
L_1	5	m
L_2	5	m
L_3	0	m
L_4	0	m
L_5	2	m
L_6	0.5	m
A	$L_1 \cdot 1$	m

B. Steady-state and transient

1. Initial steady-state

In this section the initial steady-state is computed for Darcy's law and the compressible models. We are both interested in the final steady-state and the transient. The initial conditions are the same as for the PWR: atmospheric pressure and temperature and an initial velocity of 0.001 $m.s^{-1}$. A 9-seconds ramp for the heat/sink and for the pressurizer is set. The plots given in Fig. VII-1, Fig. VII-2, Fig. VII-3 and Fig. VII-4 show the velocity, temperature, pressure and density profiles at steady-state for the compressible model and Darcy's law.

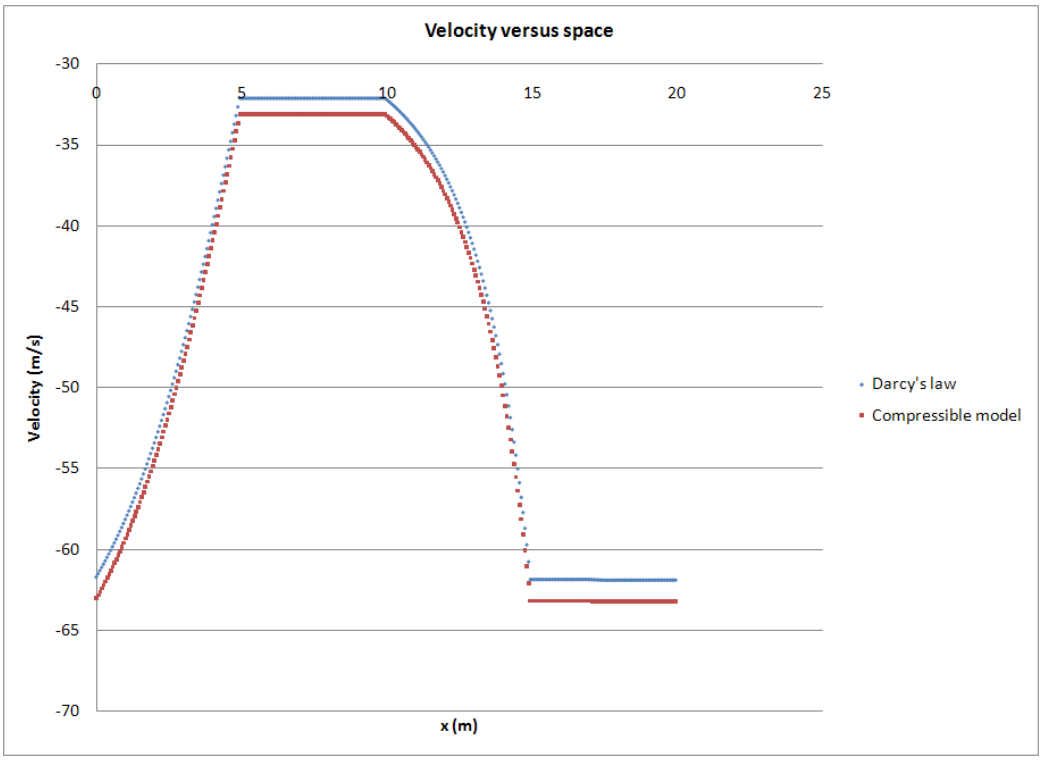

Fig. VII-1. Velocity profile at steady-state (HTGR).

The velocity (Fig. VII-1) is negative in the case of a HTGR. As a result, the profile is reversed compared to the PWR case. Along the core (for x increasing),

the absolute value of the velocity decreases, is constant along the horizontal legs and rises along the steam generator for both models. As for the PWR, buoyancy forces make the velocity increase along the core and decrease along the steam-generator. It is noted that the velocity profile for Darcy's model is shifted up by about 6 % compared to the compressible model. This variation of the velocity is not very large at steady-state.

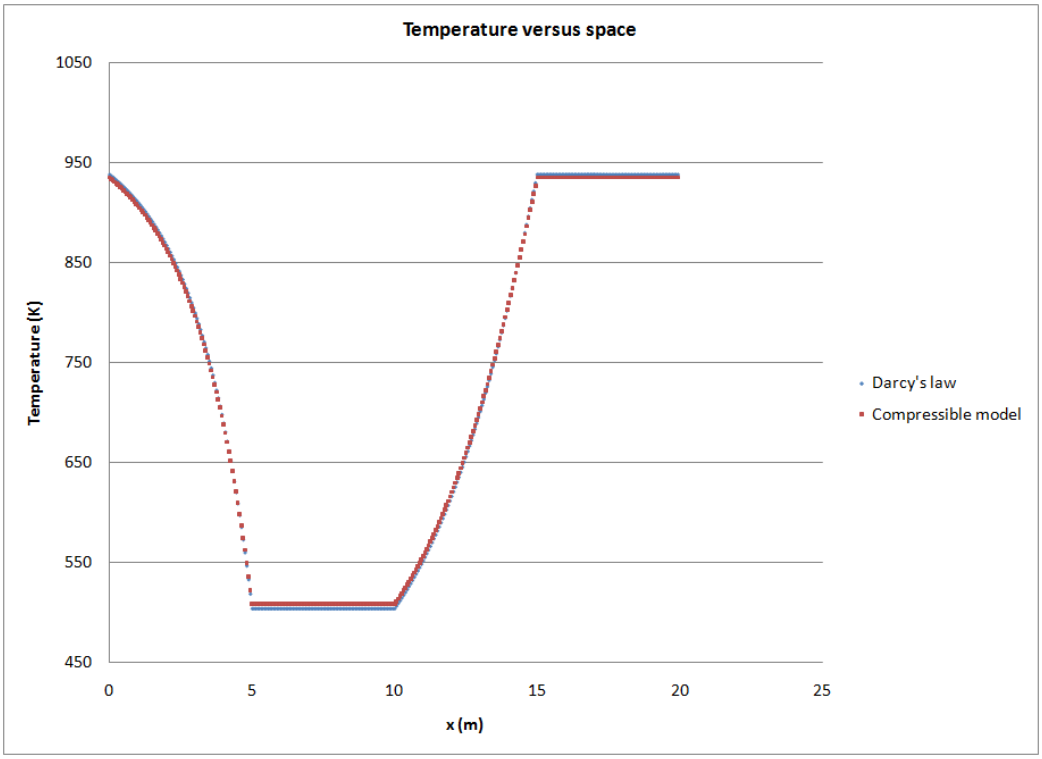

Fig. VII-2. Temperature profile at steady-state (HTGR).

The temperature (Fig. VII-2) increases along the core and decreases along the steam generator for both models (the velocity fluid is negative here). There is no heat source/sink along the horizontal legs and the temperature is constant. We can note that the temperature is not linear along the core and the steam generator as was observed in the PWR case. As a reminder, l_{core} and l_{sg} defined in section C are a

function of density and velocity. In the case of the HTGR, the velocity is about ten times larger than the velocity in the PWR. But the density of the gas is thirty times smaller than that of water density. As a result, l_{core} and l_{sg} for the gas are smaller and the ratio $\frac{x}{l_{core}}$ is larger than in the case of the PWR.

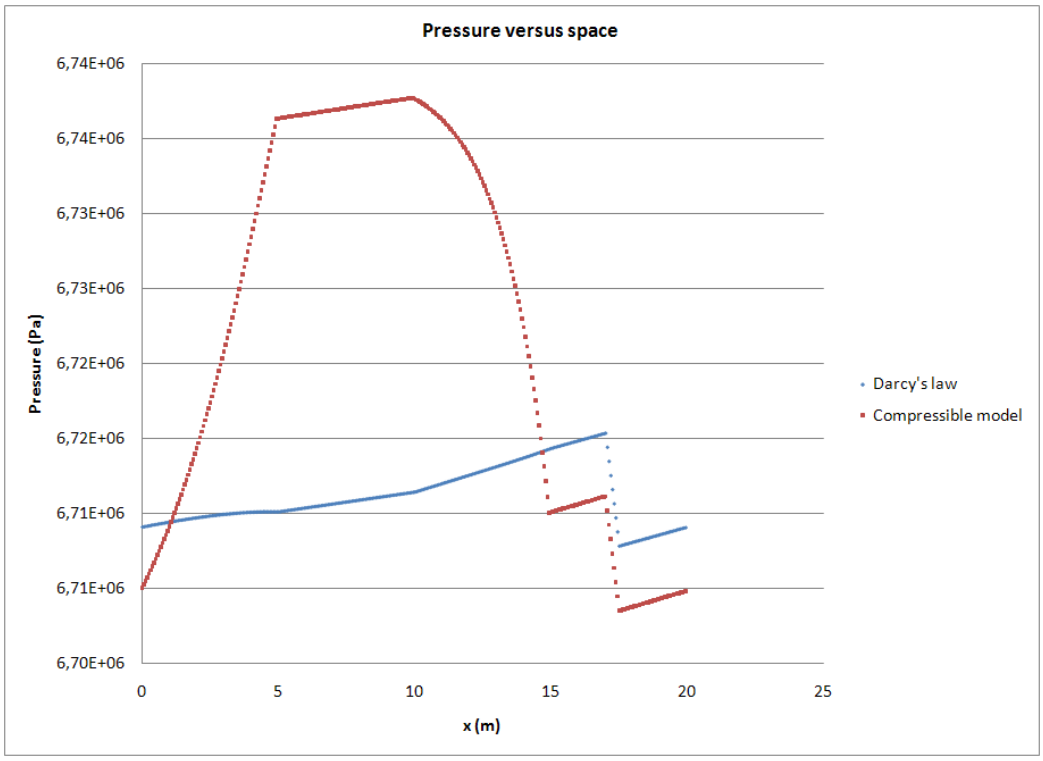

Fig. VII-3. Pressure profile at steady-state (HTGR).

The pressure profiles (Fig. VII-3) for the compressible model and Darcy's law show significant discrepancies. In a single phase flow, the pressure drop is composed of friction, gravity and acceleration terms. It is noted that along the horizontal legs, the pressure profile is the same for the compressible model and Darcy's law. On these parts, the density is constant and the flow is perpendicular to the gravity vector so that only friction pressure drops occur. Along the core and the steam generator, the acceleration and gravity components of the pressure drop are important since the

change in density is large and the gravity force in present in these parts of the loop. Along the core and the steam generator, the acceleration and gravity components make the pressure strongly vary. Darcy's law seems to account for the friction and gravity components of the pressure drop (since the slope along the core of the pressure profile is different than the slope along the horizontal legs) but not for the acceleration term. This is due to the approximation made since the convection and time dependent terms are neglected in the momentum equation. As a result, the pressure is no longer related to the change in velocity through the term $u\frac{\partial u}{\partial x}$ and to the change in density through the continuity equation. In the compressible model, the pressure varies slightly along the horizontal legs because of the friction component of the pressure drop.

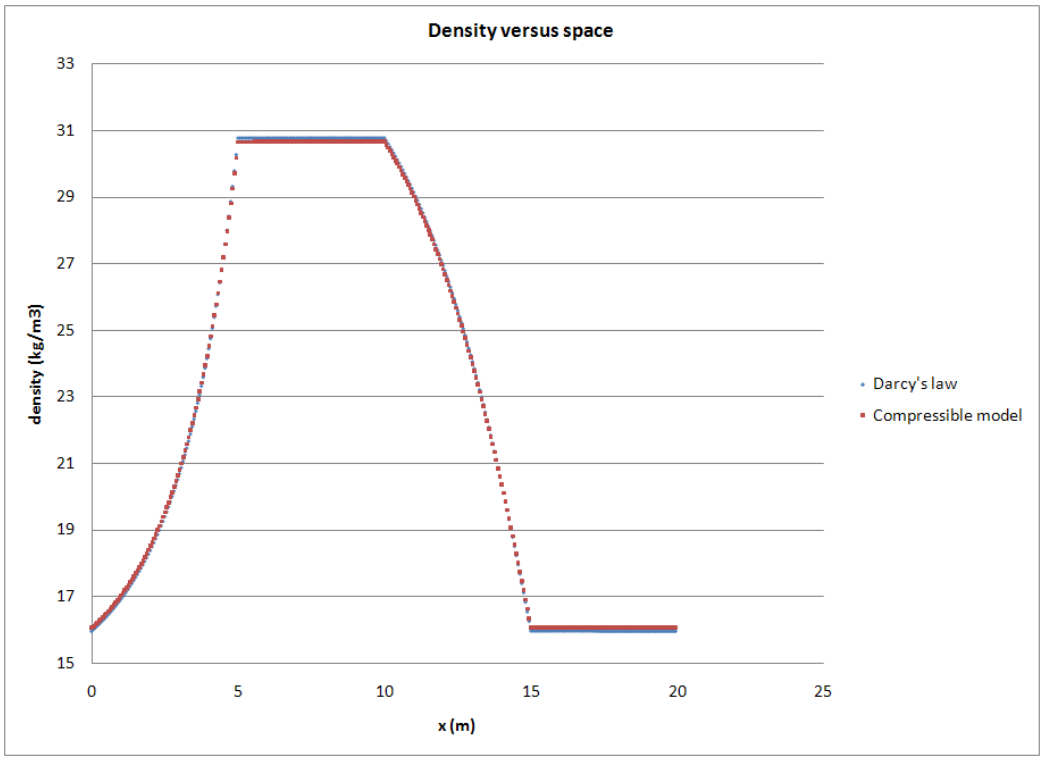

Fig. VII-4. Density profile at steady-state (HTGR).

The density (Fig. VII-4), in both models, is computed using the Equation Of State given by Eq. (3.4) so that the density is temperature and pressure dependent. The speed of sound in the gas is 600 $m.s^{-1}$. As a result, the density is mainly temperature-dependent. Once again, the velocity is negative. As x increases (from the bottom to the top of the core), the density increases since the temperature decreases along the core because of Buoyancy forces. Along the steam generator the opposite variation is observed. The density remains constant along the horizontal legs since the temperature does not vary there.

2. Pseudo-transient to reach the initial steady-state (pump on)

This section describes the pseudo-transient employed to reach the initial steady-state described in section 1. Variations of the temperature and the velocity as a function of time during the transient are shown. The energy supplied to and removed from the system is also plotted as a function of time. The uncertainties between models are pointed out.

From Fig. VII-5, we can observe that the velocity has different variations as a function of time for Darcy's law and the compressible model. When Darcy's law is used, the velocity is explicitly given by Eq. (3.34). There is no dependence in time and the velocity will reach a value very far from the initial velocity ($0.001 m.s^{-1}$) after the first iteration in time. In the compressible model, the velocity is time dependent and rises until the steady-state value. The steady-state values are not exactly the same and an offset of 10% (3 m/s) is noted.

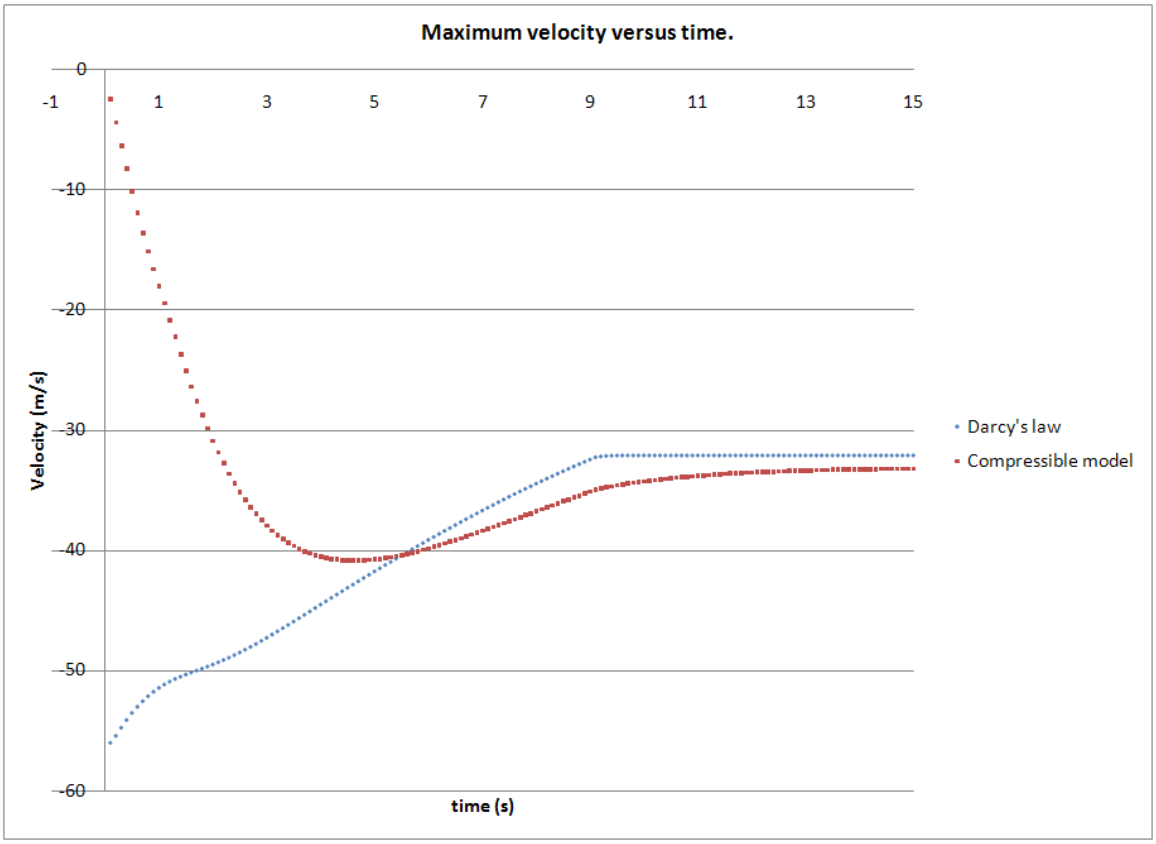

Fig. VII-5. Velocity versus time during the pseudo-transient.

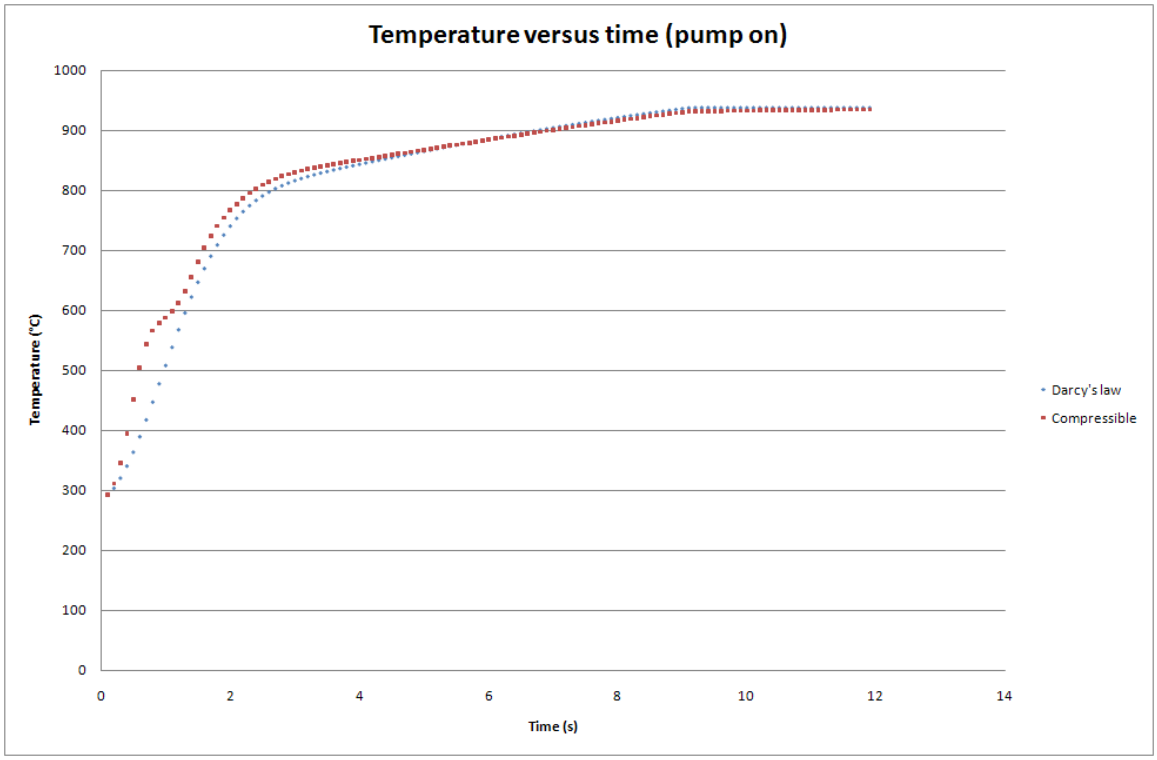

Fig. VII-6. Temperature versus time for pseudo-transient.

From Fig. VII-6, two regions can be distinguished: before and after $t = 4\ s$. Before $t = 4\ s$, the temperature computed with Darcy's law is larger than the compressible model's temperature . After $t = 4\ s$, the temperature profiles are identical and reach the same steady-state values.

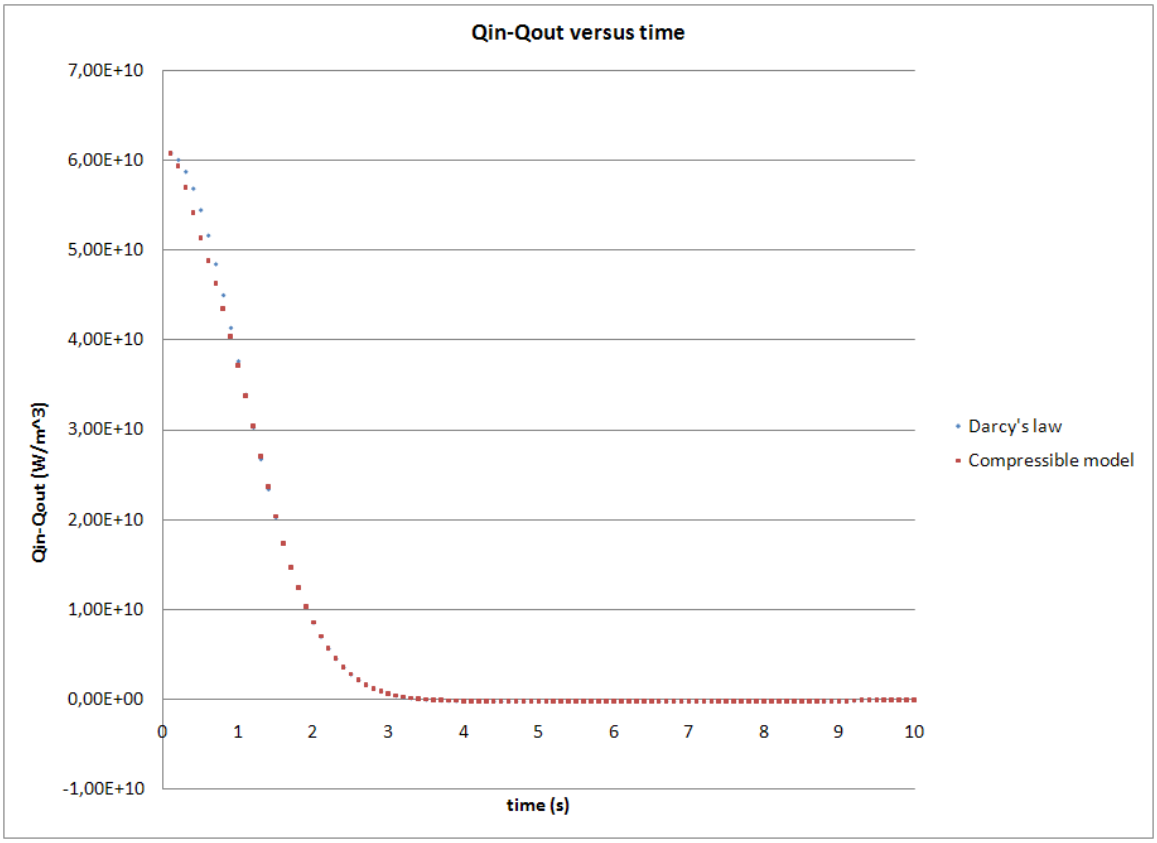

Fig. VII-7. $Q_{in} - Q_{out}$ as a function of time with pump on.

Fig. VII-7 shows the variation of the energy supplied to (Q_{in}) and removed from (Q_{out}) the fluid as a function of time for both models. Little differences is noted any large differences between Darcy's law and the compressible model. This was expected since the energy is computed as a function of the temperature and we did not notice any large differences between the models in Fig. VII-6.

3. Model uncertainty

The aims of this section is to quantify the approximation made by using Darcy's law compared to the compressible model. As a reminder, Darcy's law consists of neglecting the time dependent and convection terms of the momentum equation. As

a result, it is interesting to plot at a given time of the transient, the different values of each term of the momentum equation in order to measure the accuracy of the approximation. This study is also done at steady-state.

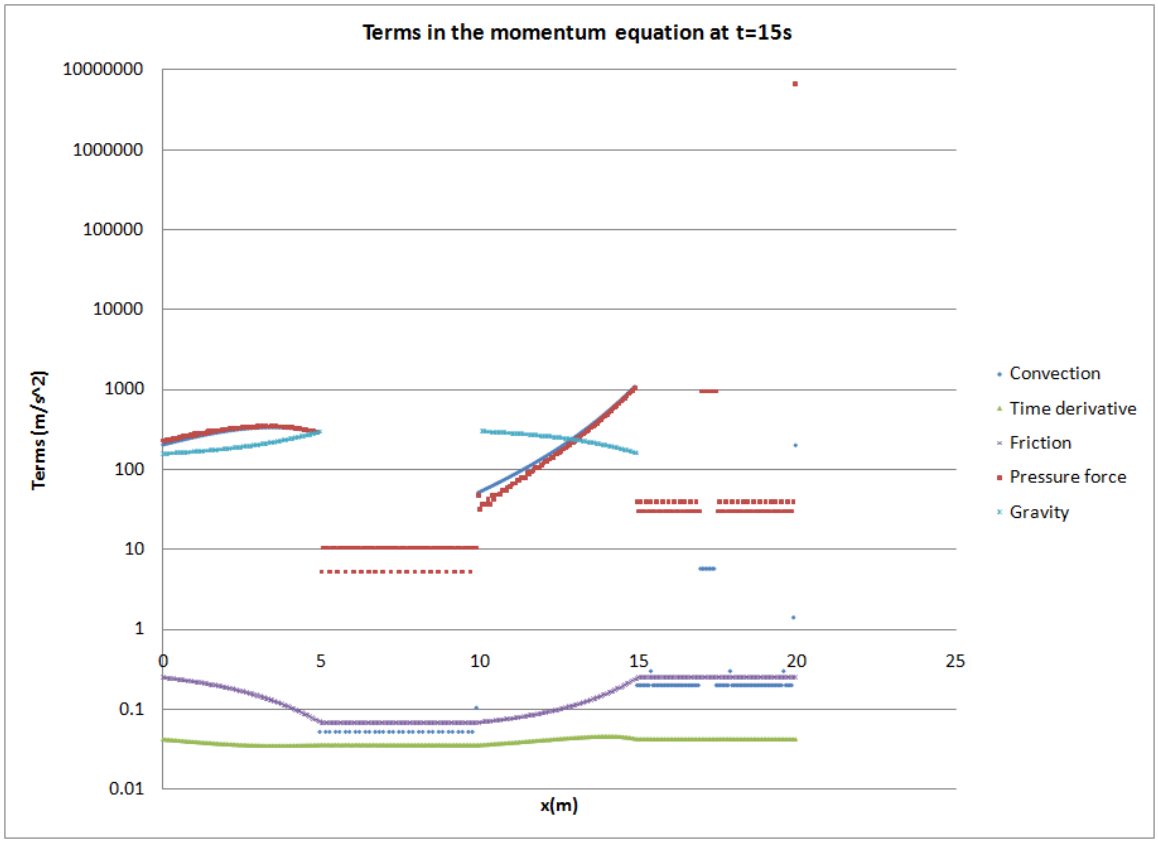

Fig. VII-8. Terms of the momentum equation as a function of space at $t = 15s$ with the pump turned on.

From Fig. VII-8, the different terms of the momentum equation are plotted at a date $t = 15\ s$ during the pseudo-transient. We observe that, the time dependent and convection terms, $\rho\frac{\partial u}{\partial t}$ and $\rho u\frac{\partial u}{\partial x}$, respectively, cannot be neglected compared to the friction, pressure and gravity terms as suggested by Darcy's law. This was expected since some large differences in the velocity between the two models as a function of time were noted in section 2.

The same study is performed for the steady-state and the graph is given in

Fig. VII-9.

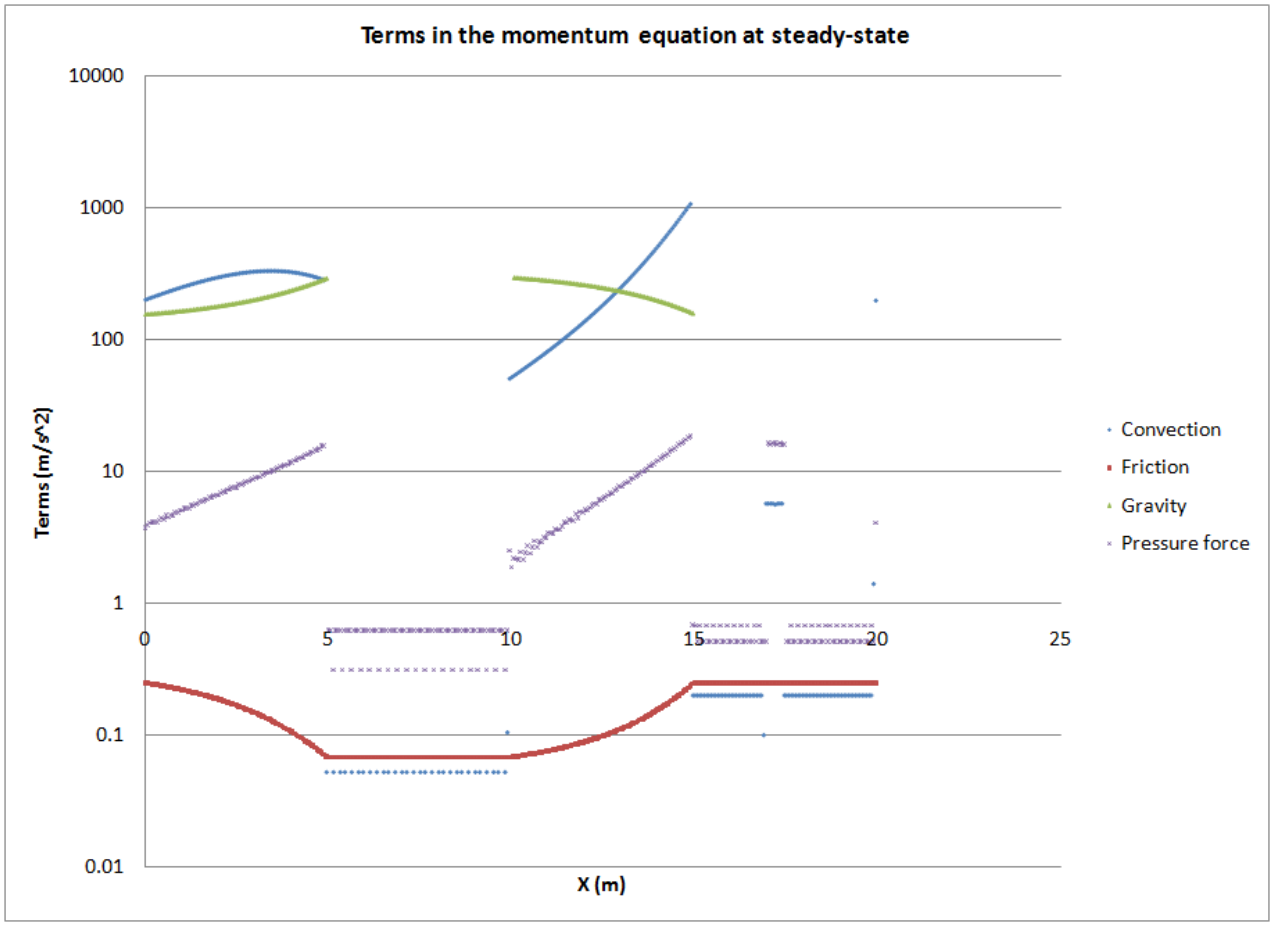

Fig. VII-9. Terms of the momentum equation as a function of space at steady-state.

It is noted that the convection term dominates the other terms in the core and the steam generator. In other terms, as the temperature changes, Darcy's law is no longer accurate. The time dependent term is not plotted since this is a steady-state study analysis.

In this section, it is shown that Darcy's law is not a good approximation of the compressible model in forced convection. More precisely, some large differences are noted in the pressure profile at steady-state. However, the temperature profiles at steady-state are very similar.

C. Study of transient: pump coast down

In this section, the simulation consists of a pump coast-down, where the pump is completely stopped within a 4 seconds ramp. As in the PWR case, the buoyancy forces will take over to cool down the core. The study is very similar to the one carried out for the PWR case in Chapter VI. Darcy's law and the compressible model are run from the same compressible steady-state and the profiles are compared.

1. Transient pump off

In this section, the temperature, the velocity and the pressure profiles are plotted as a function of time in Fig. VII-10, Fig. VII-11 and Fig. VII-12. As for the PWR case, the energy supplied to and removed from the fluid is plotted as a function of time for both models in Fig. VII-13.

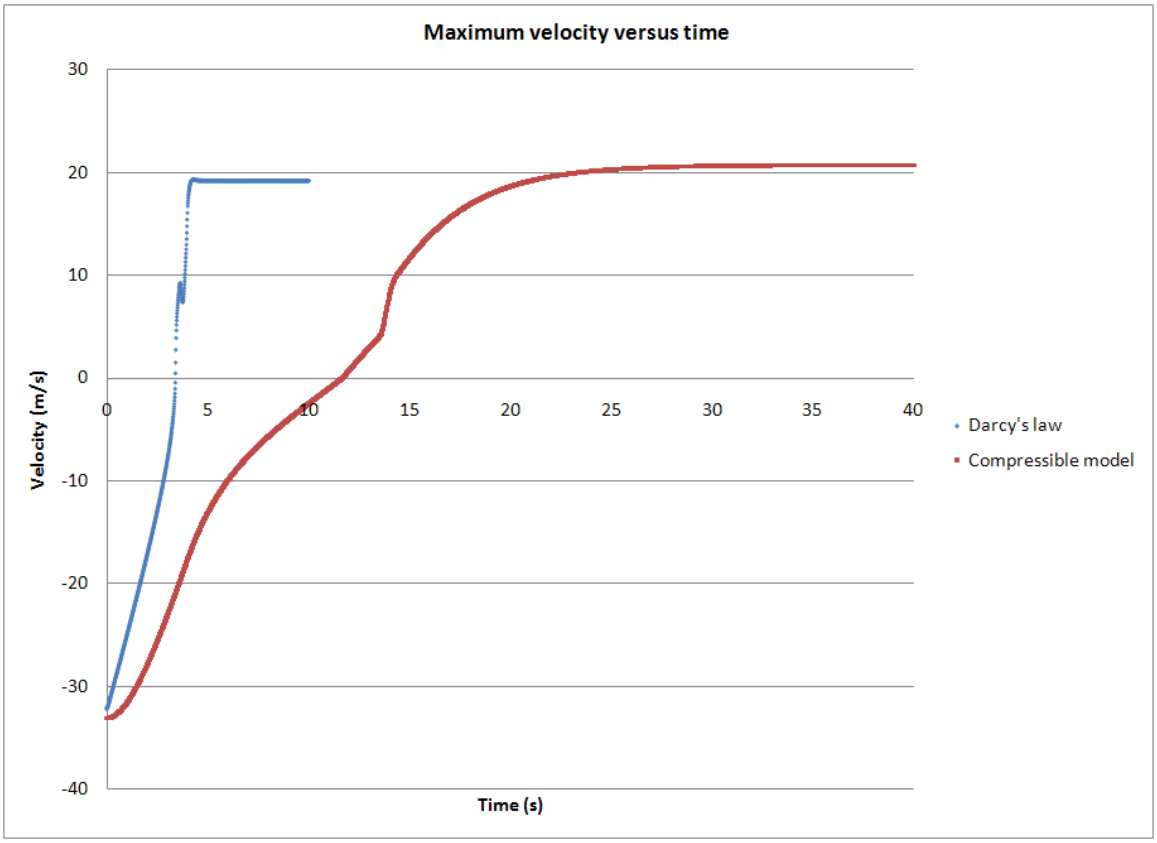

Fig. VII-10. Velocity profile as a function of time during the pump coast down transient.

We can note in Fig. VII-10 that the velocity profiles are significantly different between Darcy's law and the compressible model. As the pump is turned off after a ramp of 4 s, the velocity from Darcy's law changes of sign at about the same time. Hence the fluid suddenly changes its direction of flow. This is not the case with the compressible model, where the fluid has some momentum and only reserves its direction of flow at $t = 12$ s. The final value of the velocity between Darcy's law and the compressible model are not exactly the same. In the case of Darcy's law, the steady-state velocity is reached quickly.

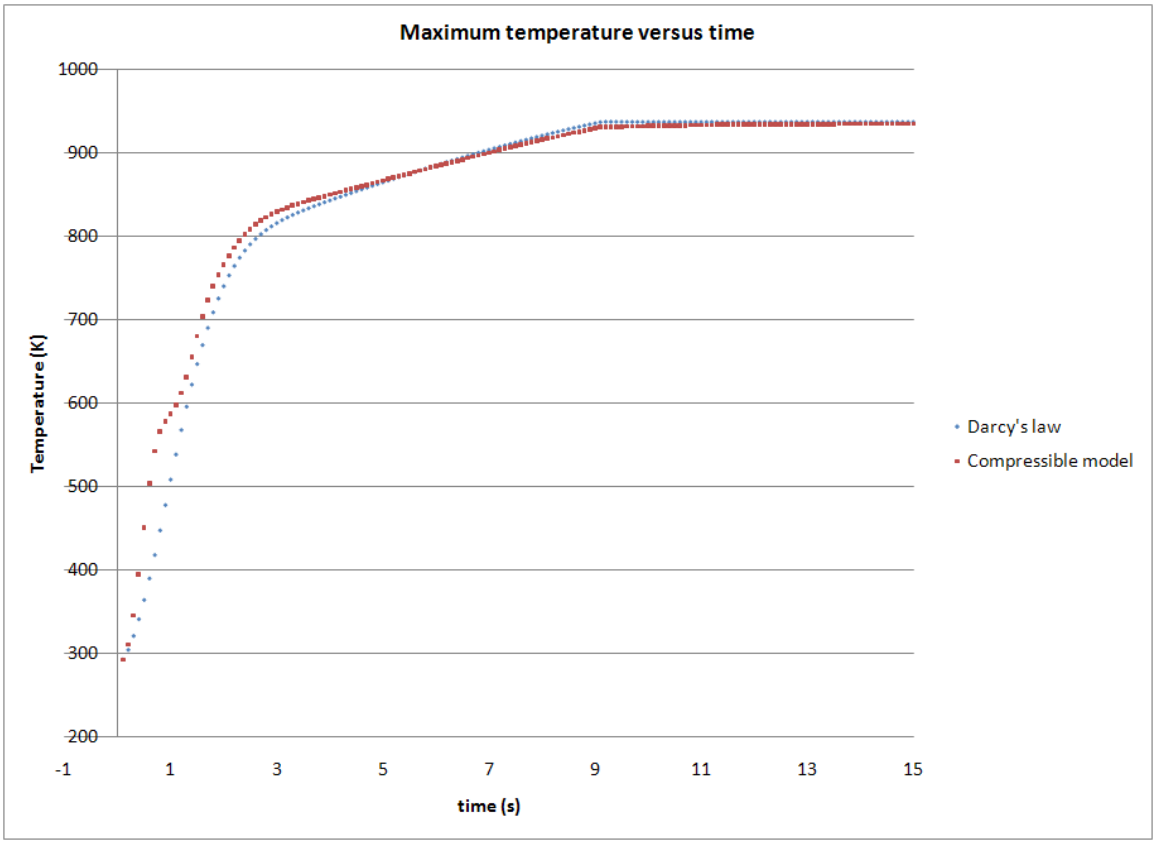

Fig. VII-11. Temperature profile as a function of time during the pump coast down transient.

As the pump strength decreases, the maximum temperature increases since the velocity of the fluid decreases in both models (Fig. VII-11). Darcy's law and the compressible model, do not yield the same temperature profile. The rise of temperature is faster with Darcy's law than with the compressible model. As the steady-state is reached, the temperature value are not hardly different, about 1% difference. In addition, the steady-state is reached faster whe using Darcy's law.

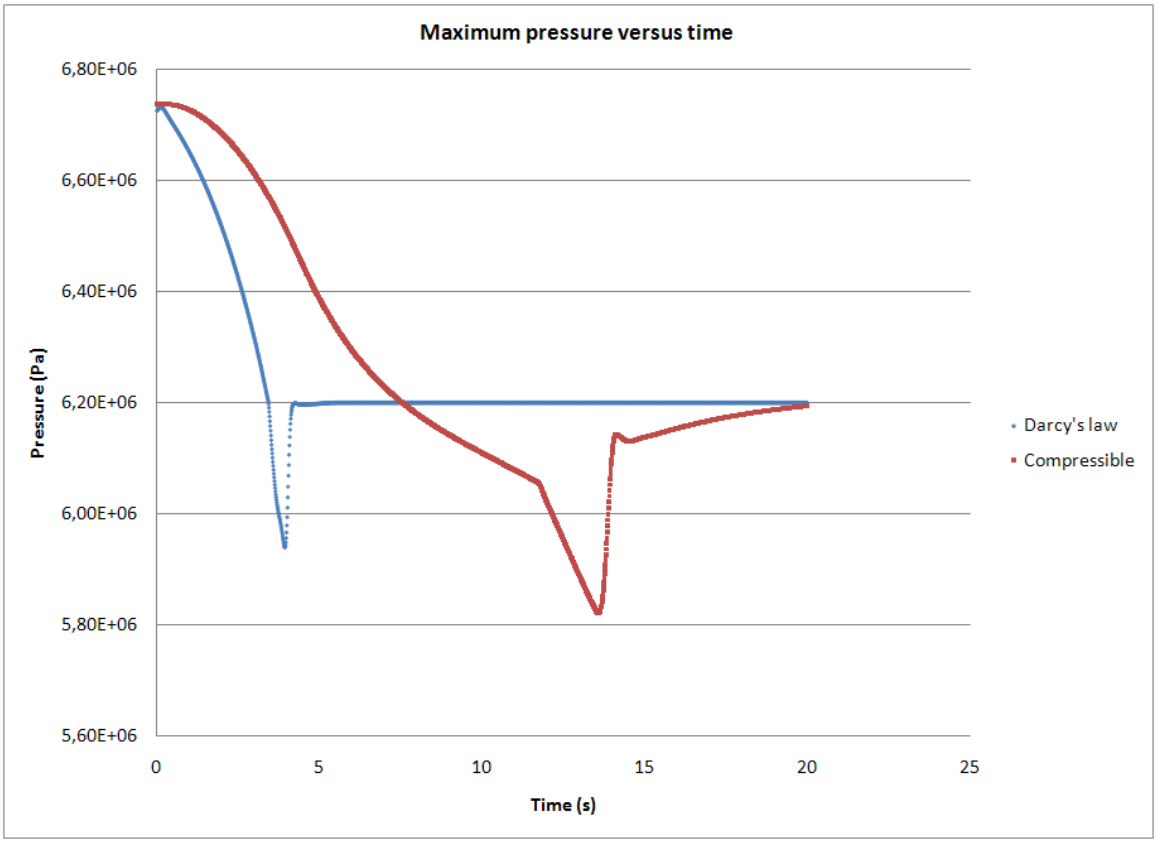

Fig. VII-12. Pressure profile as a function of time during the transient.

In Fig. VII-12, we note that the variation of the pressure are the same for both models but with a time delay for the compressible model. When Darcy's law is used, the pressure reaches its minimum as soon as the pump is completely off. In the compressible model, the pressure reaches its minimum (a lower minimum than in Darcy's law case) 8 s after the end after the pump has been shut off. Both models converge to the same final pressure value at steady-state.

Fig. VII-13 shows the variation of the energy supplied to and removed from the system as a function of time for Darcy's law and the compressible model. The green plot is the compressible steady-state run with Darcy's law in order to see how the numerical simulation is affected by a change of model.

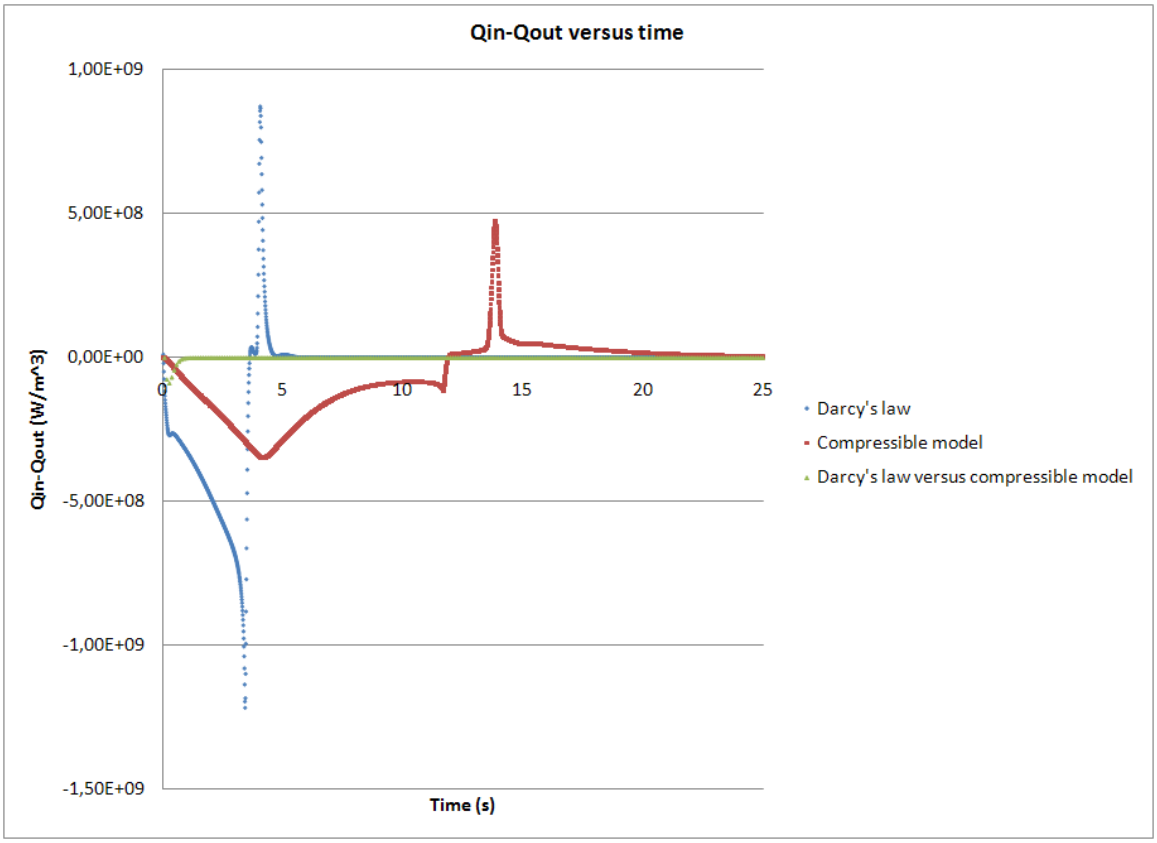

Fig. VII-13. $Q_{in} - Q_{out}$ versus time during the transient.

First, the numerical solution is not strongly affected by the change of model. As a result, the modifications can be neglected since the variations are much smaller than the variations due to the pump ramp. The variations of $Q_{in} - Q_{out}$ are very different between Darcy's law and the compressible model. It seems that the compressible model has almost the same variations as Darcy's law but with a time delay. The magnitude of the peaks are also different. At $t = 4s$ (end of the pump's ramp), the plot $Qin - Qout$ for Darcy's law experiences a change of sign, then a peak, and reaches a steady-state value. For the compressible model, at $t = 4s$, the slope is changed but $Qin - Qout$ remains negative. The change of sign occurs later at $t = 12s$. Then, a peak occurs with a smaller magnitude than in Darcy's law. The same final steady-

state value is reached.

This study of the transient shows that Darcy's law reaches a steady-state faster than the compressible model. In addition, the velocity and pressure profiles are very different. This could be expected since Darcy's law modifies the momentum equation. The temperature profiles are very similar for Darcy's law and the compressible model.

2. Final steady-state after the pump coast down transient

This section aims at presenting the final steady-state profile of the velocity, temperature, the pressure and the density after the transient in Fig. VII-14, Fig. VII-15, Fig. VII-16 and Fig. VII-17.

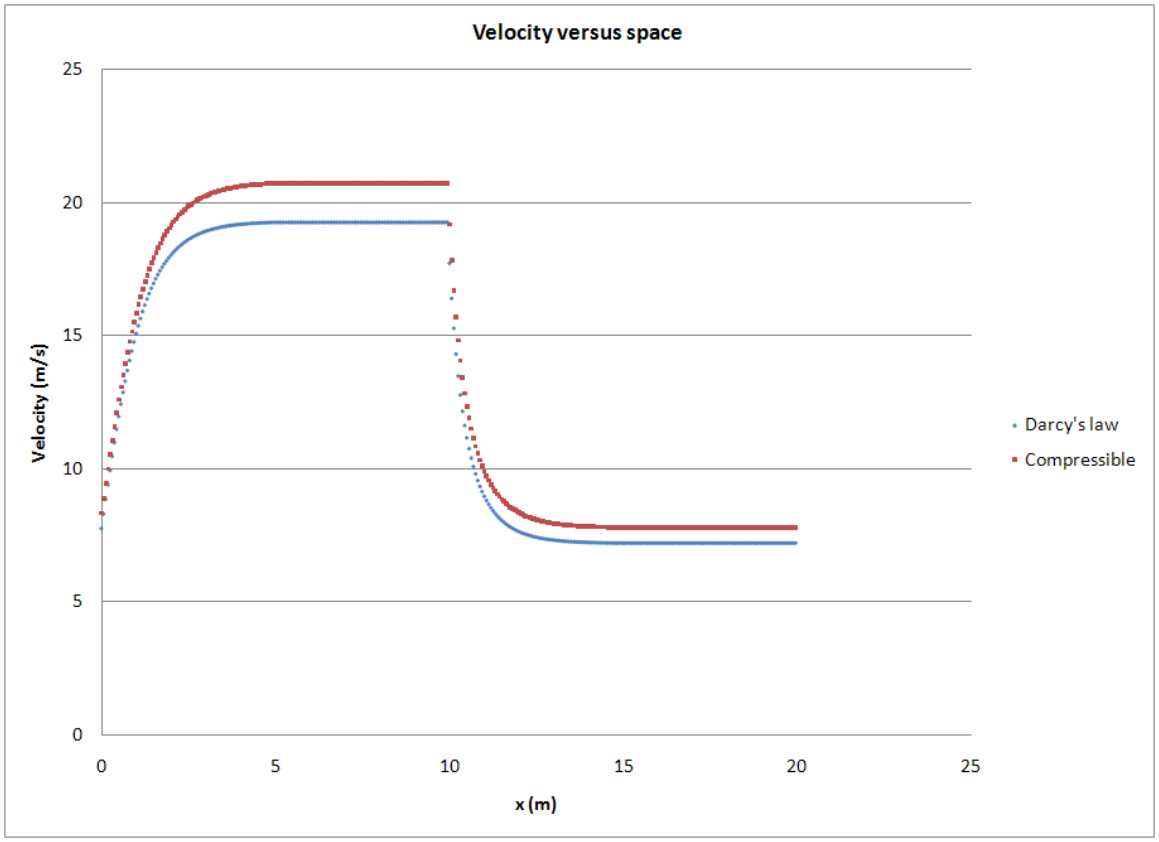

Fig. VII-14. Velocity profile as a function of space at the final steady-state.

From Fig. VII-14, we noted that both models have the same the velocity distribution in space. However, some differences are noted in the magnitude of the velocity. There is an offset of about 10% between Darcy's law and the compressible model (same as the steady-state as the pump is turned on). These differences mainly come from the approximation made in the momentum equation for Darcy's law.

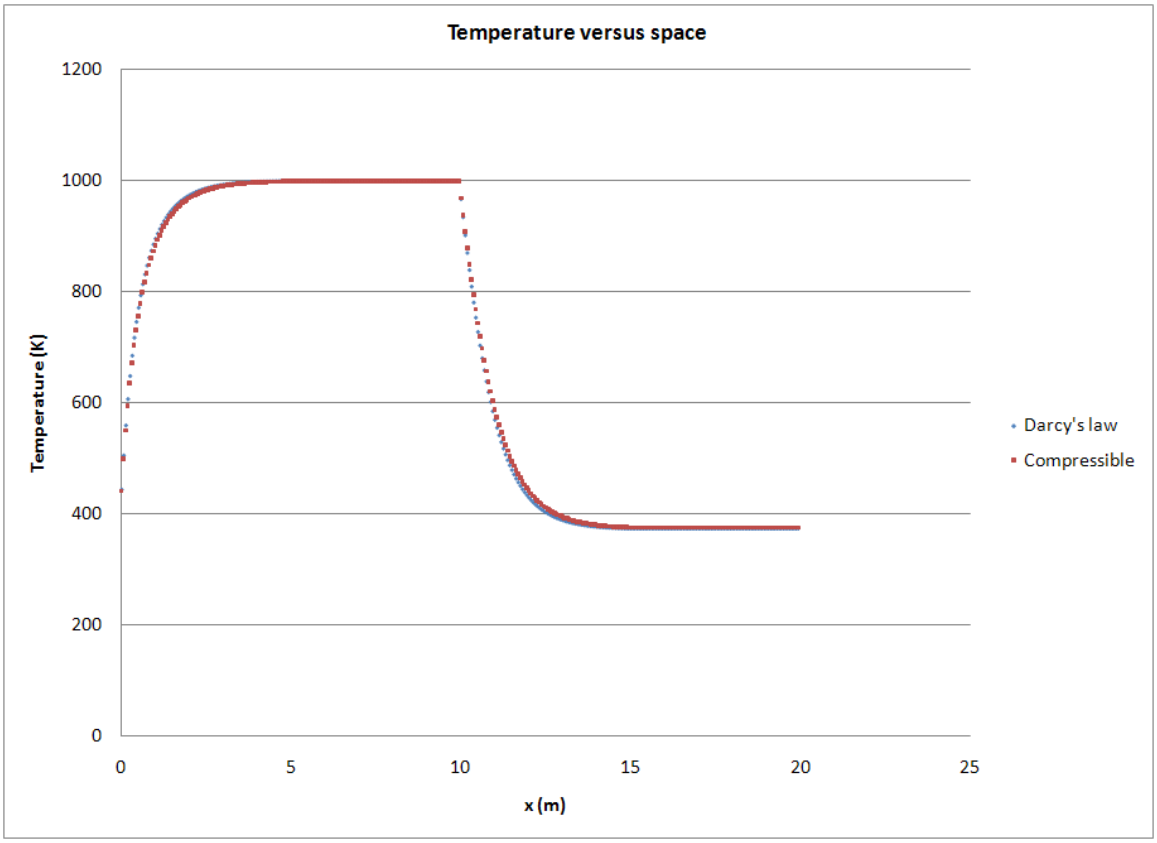

Fig. VII-15. Temperature profile as a function of space at steady-state.

The temperature profiles (Fig. VII-15) are very similar: the magnitude and the shape are the same.

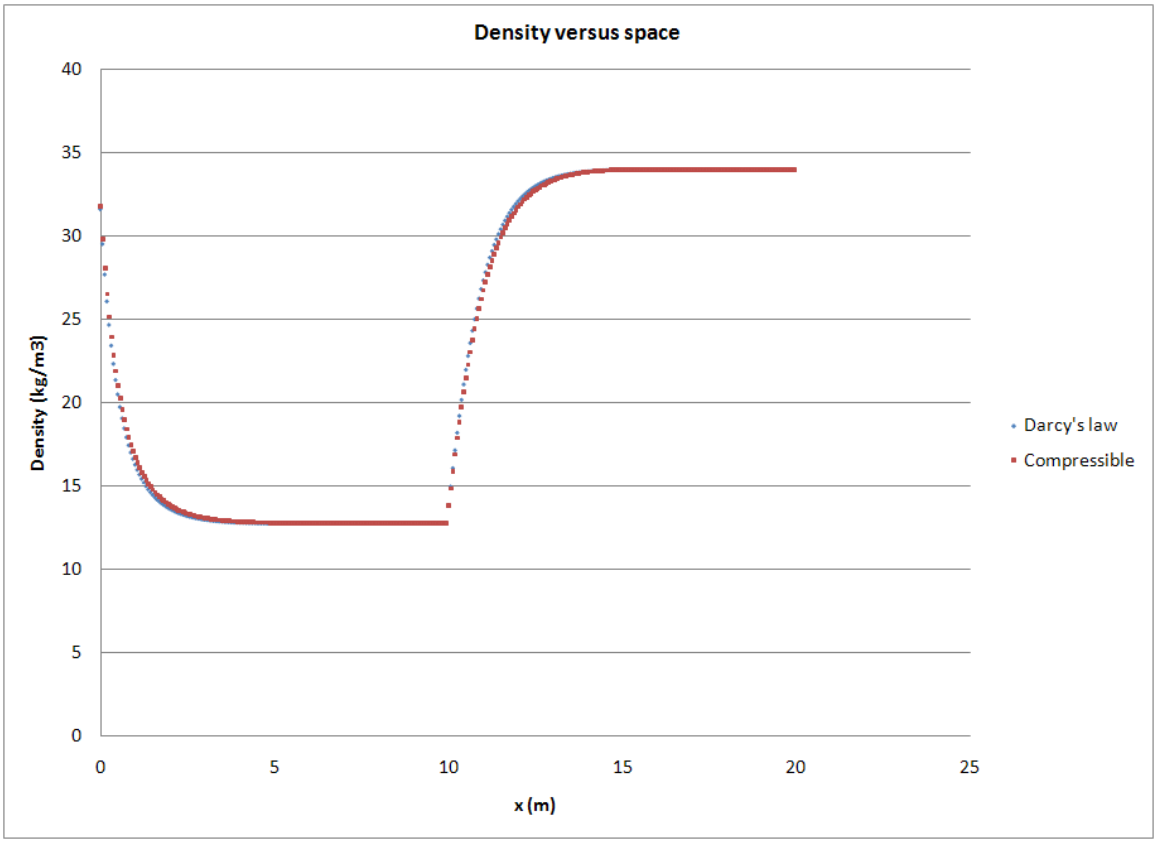

Fig. VII-16. Density profile as a function of space at steady-state.

Likewise, the density profiles (Fig. VII-16) are similar. Darcy's law only modifies the momentum equation so that it is expected to have the same temperature and density profiles computed using the energy and continuity equations, respectively.

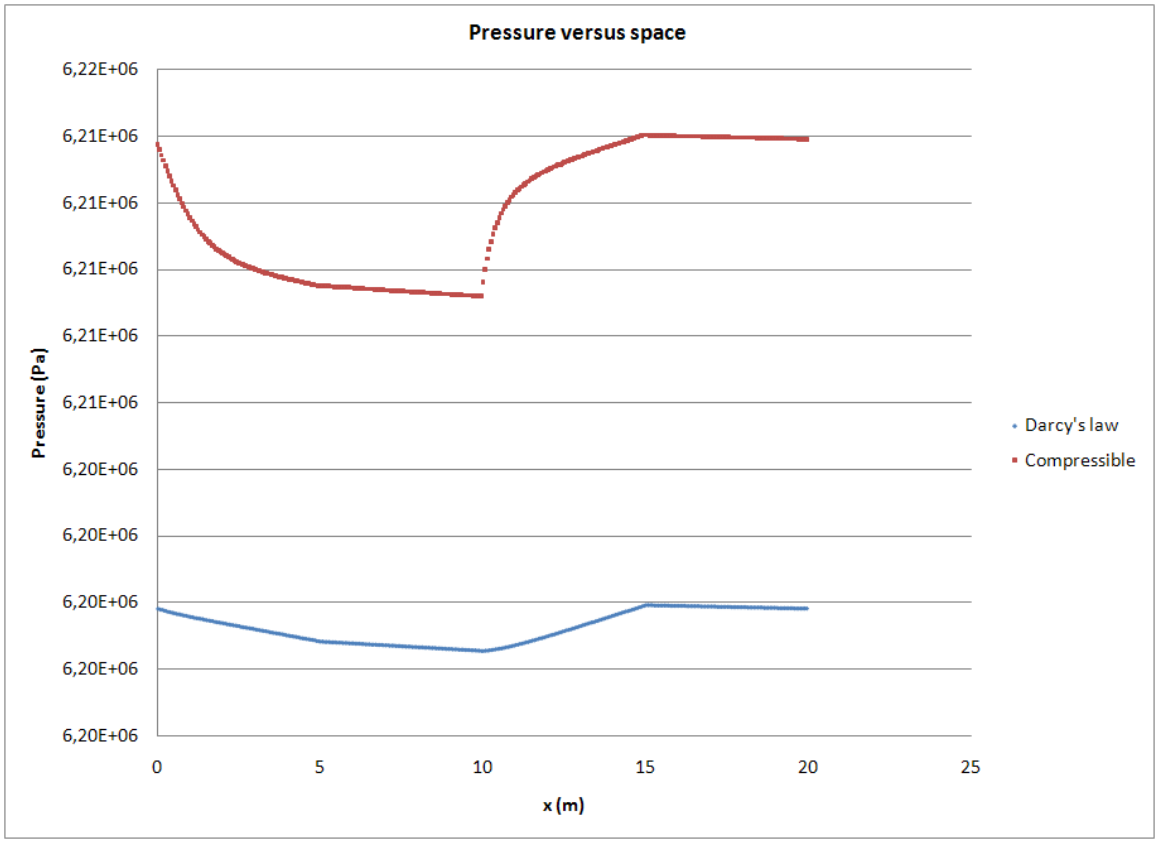

Fig. VII-17. Pressure profile as a function of space at steady-state.

In Fig. VII-17, we note that the pressure profiles computed with Darcy's law and the compressible model are very different. As explained in section 1, the acceleration of the pressure drop does not appear in Darcy's law since the pressure is not related to the change of density in the momentum equation. The variation of the pressure in the case of Darcy's law is only due to the friction and gravity forces. In the compressible model, the pressure is function of the friction and gravity forces and of the change of density along the core and the steam generator.

Through this study, it is shown that the temperature and density profiles are the same. The velocity and pressure profiles, however, are very different. Once again, Darcy's law does not seem to be a good approximation if we are interested in the

steady-state profiles of the velocity and the density in the case of free convection.

CHAPTER VIII

CONCLUSIONS AND FUTURE WORK

We have solved the modified Euler Equations for the primitive variables using a Finite Volume method for a closed loop 1D system representing a nuclear core and its primary loop. Time and space convergence studies demonstrate that the code is first-order in time and space. We have also shown that the code converges to the exact analytical steady-state solution in the case of the incompressible model. The study of (1) a pseudo-transient to reach the initial steady-state, (2) a pump coast down transient to assess the effect of the choice of fluid model from forced to natural convection, and (3) its final steady state with the characteristics of a PWR and HGTR were performed.

The PWR case suggests conditions when the incompressible model can be used:

- In forced convection mode and with a laminar flow, both models have the same transient and steady-state. The term $\frac{\partial u}{\partial x}$ can be neglected in this case and the incompressible model is a good approximation.

- In natural convection mode, the incompressible model seems to be an unreasonable approximation and does not yield the same numerical solution as the compressible model. We show that the final steady-state is still the same, but some significant discrepancies can be observed during the pump coast down transient.

In other terms, the compressible and incompressible models give the same numerical solution under forced convection and laminar flows conditions, but is not in the case for natural convection.

In addition, the same study was also performed for a HTGR reactor.

- In forced convection and with a laminar flow, Darcy's law and the compressible model yield some different profiles for the velocity and the pressure. The density and temperature profiles are similar. The same conclusions are made regarding the pseudo-transient employed to reach the initial steady-state.

- In natural convection mode and with a laminar flow conditions, the density and temperature profiles are also the same. However strong differences are observed in the pressure and velocity profiles both during the pump coastdown transient and at the final steady-state.

The conclusion of this study is that Darcy's law is not a reasonable approximation of the compressible model both in natural and forced convection if we are interested in the pressure and the velocity profiles. The temperature and density profiles at steady-state are similar and can be computed using Darcy's law and the steady-state is obtained faster than with the compressible model. In all cases, the transient computed using Darcy's law is very different than the one of the compressible model.

Some future work and improvement might include:

- The source term will include a feedback component $\frac{\partial Q}{\partial T}$, as well as a term to simulate a SCRAM.

- Correlations might be added for the heat transfer coefficients h_{core} and h_{sg}.

- The friction term correlation, f_w, could be changed in order to better model the behavior of a High Temperature Gas Reactor.

REFERENCES

[1] R.C. MARTINEAU, R.A. BERRY, A. ESTEVE, K.D. HAMMAN, D.A. KNOLL, R.PARK, W.TAITANO, "Comparative Analysis of Natural Convection Flows Simulated by Both the Conservation and Incompressible Forms of the Navier-Stokes Equation in a Differentially-Heated Square Cavity," Idaho National Laboratory, Idaho, (January 2009).

[2] R.A. BERRY and R.C. MARTINEAU, "Examination of the PCICE Method in Nearly Incompressible as Well as Strictly Incompressible Limits," *Journal of Power and Energy Systems*, **2**, *2*, 598-610, (2008).

[3] R.A. BERRY and R.C. MARTINEAU, "An Efficient, Semi-Implicit Pressure-Based Schemme Employing a High-Resolution Finite Element Method for Simulation Transient and Steady, Inviscid and Viscous, Compressible Flows on Unstructured Grids," Technical Report INEEL/EXT-03-00490, Idaho National Laboratory, Idaho, (April 2003).

[4] R.A. BERRY and R.C. MARTINEAU, "The Pressure-Corrected Ice Finite Element Method (PCICE-FEM) for Compressible Flows on Unstructured Meshes," Journal of Computational Physics **198**, 659-685, (2004).

[5] D.R. DURRAN and A. ARAKAWA, "Generalizing the Boussinesq Approximation to Stratified Compressible Flow," *C.R. Mecanique*, **335**, 655-664, (2007).

[6] F. BELBLIDIA, I.J. KESHTIBAN and M.F. WEBSTER, "Novel Schemes for Steady Weakly Compressible and Incompressible Flows," *ACME-UK Conference University of Strathclyde*, Glasgow, UK, (2003).

[7] H. FENECH, *Heat Transfer and Fluid Flow in Nuclear System*, Pergamon Press, Oxford, (1981).

[8] J.D. RAMSHAW and V. MOUSSEAU, "Damped Artificial Compressibility Method for Steady-State Low-Speed Flow Calculations," *Computers Fluids*, **20**, *2*, 177-186 (1991).

[9] C.A.J. FLETCHER, *Computational Techniques for Fluid Dynamics*, Springer-Verlag, Idaho National Laboratory, Idaho Falls, Idaho, (1990).

[10] ERIN D. FICHTL, ANIL K. PRINJA, and JAMES S. WARSA, "Stochastic Methods for Uncertainty Quantification in Radiation Transport," *International Conference on Advances in Mathematics, Computational Methods and Reactor Physics*, New York, (2009).

APPENDIX A

CODE AND ROUTINES

This section aims at describing the main subroutines as well as important variables used in the code. In the first paragraph, the variables are described and then a section deals with the different routines.

A. Variables

The variable are organized in structures and are listed above:

- $eos - dat$ stores the variable relative to the fluid parameters (viscosity, density, ...).
- $para$ contains all α parameters used to select the different models in the code.
- $geom$ stores the geometrical parameters such as the position of the pressurizer and the pump or the length of the core and the steam generator.
- V and V_{old} are the solution vectors at time $n+1$ and n, respectively. They contain the temperature, the velocity and the pressure of each cell in this order.
- $delta - t$ and $delta - x$ are the time and space size grids respectively.
- the number of cells in the loop is called nel.

The variables and structures listed above are the main parameters of the code.

B. Subroutines

- *input* is a subroutine allowing to set the parameters described in appendix A. The initial vector can either be set to atmospheric conditions with a velocity of 0.001 m/s (the velocity cannot be initially set to zero since the code accounts for friction forces), or can be read from a file if the code has to start from a steady-state which is the case when the pump is turned off.

- *main* allows calling the *input* subroutine and contains the loop over time. It also detects the steady-state by computing the energy removed from and supplied to the system that must equal within a given tolerance. The data are saved in a text file every ten iterations in time by calling the function $save - data$.

- $newton - solve$ computes the residual and the Jacobian matrix used as a pre-conditioner by calling the function *assembly* and *jacobian* respectively. The system is solved by using the $GMRES$ function of Matlab that computes the update vector used to update the vector source V at each non linear iterations.

- *assembly* computes the global non linear residual of the system. This function is divided in two parts. First, the residual of each cell is computed (continuity, momentum and energy equations) by calling the subroutine $residual - cell - i$ and added to the total residual vector. Then, the source term relative to the pressurizer are added to some cells and a momentum equation is added at the end of the total residual vector.

- $residual - cell - i$ computes the residual of a given cell i. The time dependent and the steady-state residuals are computed separately. This subroutine calls six functions: $comp - time - continuity$, $comp - time - momentum$, $comp - time - energy$, $comp - res - continuity$, $comp - res - momentum$ and $comp -$

$res - energy$. The last three functions are used to compute the steady-state residuals and the three others for the time dependent terms.

- *eos* and $eos - boussinesq$ are two subroutines that compute the density using the equation of state given in Eq. (3.4). $eos - boussinesq$ is only used in the momentum equation to compute the density that is multiplied by the gravity term. These two functions are a function of the α parameters described in section F.

- $compute - momentum - pressurizer$ computes the momentum equation to determine the velocity of the fluid coming into or out of the loop through the pressurizer. This function is called in the subroutine $residual - cell - i$.

The functions described above are the main subroutines of the code.

APPENDIX B

THE ANALYTICAL SOLUTION FOR THE INCOMPRESSIBLE MODEL

In the case of the incompressible model, it is possible to derive an analytical steady-state solution from the equations. The modified Euler Equation in the case of the incompressible model are recalled:

$$\partial_x(u) = 0 \tag{B.1}$$

$$\rho\partial_t u + \rho u\partial_x u + \partial_x P + \hat{\rho} g\left(1 - s_p\right) + f_w \frac{\rho}{D_h}\left|u\right| u = 0 \tag{B.2}$$

$$\rho\ C_v\partial_t T + \rho u C_v\partial_x T + P\partial_x u = Q(x,t) \tag{B.3}$$

$$\rho = \rho_0 \tag{B.4}$$

$$\hat{\rho} = \rho_0 + \frac{\partial\rho}{\partial T}\left(T - T_0\right) \tag{B.5}$$

here ρ and $\hat{\rho'}$ are the constant density and the density computed with the Boussinesq correction, u is the velocity, T and P are the temperature and pressure respectively, f is the friction factor, s_p is the pump strength, D_h is the hydraulic diameter, Q is the heat source and C_v is the heat capacity. These equations contain a momentum source and energy source.

The momentum and energy equations can be simplified using the continuity equation:

$$\rho_0\partial_t u + \partial_x P + \hat{\rho} g\left(1 - s_p\right) + f\frac{\rho_0}{D_h}\left|u\right| u = 0 \tag{B.6}$$

$$\rho_0\ C_v\partial_t T + \rho_0 u C_v\partial_x T = Q(x,t) \tag{B.7}$$

An analytical solution can be derived from the equations above at steady state. The steps are detailed for the temperature and pressure profiles along the core and

the results will be given for the other legs of the loop (pressurizer, steam generator and pump). Along the core, the heat source is $Q(x) = h_{core} L_1 \left(T_{wcore} - T(x)\right)$ in one dimension where h_{core} is the heat transfer coefficient, L_1 is the length of the core, T_{wcore} is the wall temperature along the core and $T(x)$ is the profile of temperature along the core (it is assumed that the area is $L_1 \times 1$. Then, the energy equation yields:

$$\rho_0 u C_v \partial_x T = h_{core} L_1 \left(T_{wcore} - T(x)\right) \tag{B.8}$$

$$T(x) + \frac{\rho_0 u C_v}{h_{core} L_1} \partial_x T(x) = T_{wcore} \tag{B.9}$$

This is a first-order differential equation that can be solved analytically. To simplify the equation, lets define $l_{core} = \frac{\rho_0 u C_v}{h_{core} L_1}$ a characteristic length of the energy equation. The parameter l_{core} depends on the fluid velocity so that it will affect the temperature profile as expected. A solution for this type of differential equation is (the temperature is solved for x):

$$T(x) = A(x) e^{\frac{-x}{l_{core}}} \tag{B.10}$$

where A is a function depending on the variable x and will be computed using the differential equation as follows:

$$A(x) e^{\frac{-x}{l_{core}}} + l_{core} \frac{\partial A(x)}{\partial x} e^{\frac{-x}{l_{core}}} - A(x) e^{\frac{-x}{l_{core}}} = T_{wcore} \tag{B.11}$$

$$l_{core} \frac{\partial A(x)}{\partial x} e^{\frac{-x}{l_{core}}} = T_{wcore} \tag{B.12}$$

$$\frac{\partial A(x)}{\partial x} = \frac{T_{wcore}}{l_{core}} e^{\frac{x}{l_{core}}} \tag{B.13}$$

A differential equation for A is obtained and can be solved:

$$A(x) = T_{wcore} e^{\frac{x}{l_{core}}} + B \tag{B.14}$$

where B is a constant to determine afterwards using the boundary conditions. Then, the final solution is:

$$T_{core}(x) = T_{wcore} + B e^{\frac{-x}{l_{core}}} \tag{B.15}$$

This equation yields the temperature profile in the core. We can now derive the pressure profile along the core using the momentum equation. The temperature and the pressure are coupled through the Boussinesq correction in the momentum equation. At steady-state and along the core (no pump), the momentum equation yields:

$$\partial_x P + \hat{\rho} g + f \frac{\rho}{D_h} |u| \, u = 0 \tag{B.16}$$

$$\partial_x P + \left(\rho_0 + \frac{\partial \rho}{\partial T} (T - T_0) \right) g + f \frac{\rho}{D_h} |u| \, u = 0 \tag{B.17}$$

where P and T are the pressure and temperature respectively, $\hat{\rho}$ is the density computed using the Boussinesq correction, ρ_0 is the density at the linearization point, f_w is the friction term, g is the gravity term, u is the velocity and D_h is the hydraulic diameter. All parameters are constant but the temperature T and the pressure P depend on space. Using the solution for the temperature, a differential equation for the pressure can be derived as a function of space.

$$\partial_x P + \left(\rho_0 + \frac{\partial \rho}{\partial T} \left(T_{core} + B e^{\frac{-x}{l_{core}}} \right) - T_0 \right) g + f \frac{\rho}{D_h} |u| \, u = 0 \tag{B.18}$$

It remains to integrate over space from $x = 0$ to $x = L_1$ where L_1 is the length of the core.

$$P(x) = \frac{\partial \rho}{\partial T} B g l_{core} e^{\frac{-x}{l}} - \left[\left(\rho_0 + \frac{\partial \rho}{\partial T} \left(T_{core} - T_0 \right) \right) g - f_w \frac{\rho}{D_h} |u| \, u \right] x + C \tag{B.19}$$

where C is a constant to be determined using the boundary condition. We will assume that the pressurizer is right after the core so that the pressure is fixed in $x = L_1$.

$$P(x) = \frac{\partial \rho}{\partial T} B g l_{core} \left(e^{\frac{-x}{l_{core}}} - e^{\frac{-L_1}{l_{core}}} \right) - \left[\left(\rho_0 + \frac{\partial \rho}{\partial T} \left(T_{core} - T_0 \right) \right) g + f_w \frac{\rho}{D_h} |u| \, u \right] (L_1 - x) + P_p \tag{B.20}$$

where P_p is the pressure in the pressurizer. This equation gives the pressure as a function of space at steady-state along the core. This analytical solution will be used as a reference for the numerical solution. Of course, the constant B has to be computed. This requires to compute the temperature profile along the steam generator. The energy equation to solve for the steam generator is the following:

$$\rho_0 u C_v \partial_x T = h_{sg} L_1 \left(T_{wsg} - T(x) \right) \tag{B.21}$$

$$T(x) + \frac{\rho_0 u C_v}{h_{sg} L_1} \partial_x T(x) = T_{wsg} \tag{B.22}$$

where T_{wsg} is the temperature in the steam generator, h_{sg} is the heat transfer coefficient between the fluid and the steam generator. All other variables are defined as above. We also define $l_{sg} = \frac{\rho_0 u C_v}{h_{sg} L_1}$ as the spatial scale of the energy equation along the steam generator. The test of the derivative is similar and the solution is:

$$T_{sg}(x) = T_{wsg} + De^{\frac{-(x+L_1+L_2)}{l_{sg}}} \tag{B.23}$$

where D is a constant. To determine the constants B and D, two equations are required. The first one is obtained by stating that the temperature along the pump is constant since, in this model, the pump does not modify the energy equation (this assumption is not true along the pressurizer). As a result:

$$\begin{aligned} T_{core}\left(x=0\right) &= T_{sg}\left(x=2L_1+L_2\right) \\ T_{wcore}+B &= T_{wsg}+De^{\frac{-(2L_1+L_2)}{l_{sg}}} \end{aligned} \tag{B.24}$$

where B and D are the constants to compute, T_{sg} and T_{core} are the temperature in the steam generator and in the core respectively, and L_1 and L_2 are the loop lengths.

The second equation is obtained by considering that the steady-state is reached when the energy put into and removed from the system equal each other:

$$\begin{aligned} Q_{in} &= -Q_{out} \\ \int_0^{L_1} h_{core}L_1\left(T_{core}\left(x\right)-T_{wcore}\right) &= -\int_{L_1+L_2}^{2L_1+L_2} h_{sg}L_1\left(T_{sg}\left(x\right)-T_{wsg}\right) \end{aligned} \tag{B.25}$$

where L_1 and L_2 are the lengths of the loop, h_{core}, h_{sg}, T_{core} and T_{sg} are the heat transfer coefficients for the core and the steam generator, and the temperature for the core and steam generator respectively. By integrating this equation, a second relation between B and D is derived. Using these two relations above, the system can be solved and the constants expressed as a function of the boundary conditions (since the system is periodic, the boundary conditions are defined as the temperature in the core and in the steam generator).

$$D = \frac{T_{wcore} - T_{wsg}}{e^{-\frac{(2L_1+L_2)}{l_{sg}}} - \frac{l_{sg}h_{sg}}{l_{core}h_{core}} \frac{e^{-\frac{(2L_1+L_2)}{l_{sg}}} - e^{-\frac{(L_1+L_2)}{l_{sg}}}}{1-e^{-\frac{L_1}{l_{core}}}}} \tag{B.26}$$

$$B = (T_{wcore} - T_{wsg}) \left(\frac{1}{1 - \frac{l_{sg}h_{sg}}{l_{core}h_{core}} \frac{1-e^{-\frac{L_1}{l_{sg}}}}{1-e^{-\frac{L_1}{l_{core}}}}} - 1 \right) \tag{B.27}$$

As it can be seen above, the constants B and D are independent of the initial conditions. As a result, the numerical solution is unique and does not depend on the initial conditions, in the case of the incompressible model (this was verified). Since the constants B and D are known, the pressure equation can be derived:

$$P(x) = \frac{\partial \rho}{\partial T} (T_{wcore} - T_{wsg}) \, g l_{core} \left(\frac{1}{1 - \frac{l_{sg}h_{sg}}{l_{core}h_{core}} \frac{1-e^{-\frac{L_1}{l_{sg}}}}{1-e^{-\frac{L_1}{l_{core}}}}} - 1 \right) \left(e^{\frac{-x}{l_{core}}} - e^{\frac{-L_1}{l_{core}}} \right) - \left[\left(\rho_0 + \frac{\rho}{T} \right) g + f_w \frac{\rho}{D_h} |u| \, u \right] (L_1 - x) + P_p \tag{B.28}$$

The same study can be done for all the other legs of the loop. The steps are not detailed but the method is similar to the above are. There is neither heat source nor sink along the horizontal legs containing the pressurizer and the pump (the temperature in the pressurizer is set to the temperature of the cells linked to it). The

temperature and the pressure profiles along the pressurizer are:

$$T_{pressurizer}(x) = T_{core}(x = L_1) \tag{B.29}$$

$$P_{pressurizer}(x) = P_p + f\frac{\rho_0}{D_h}\left|u\right|u\left(L_1 + L_3 - x\right) \text{ for } x \in [L_1; L_1 + L_3] \tag{B.30}$$

$$P_{pressurizer}(x) = P_p \text{ for } x \in [L_1 + L_3; L_1 + L_3 + L_4] \tag{B.31}$$

$$P_{pressurizer}(x) = P_p + f_w\frac{\rho_0}{D_h}\left|u\right|u\left(L_1 + L_3 + L_4 - x\right) \text{ for } x \in [L_1 + L_3 + L_4; L_1 + L_2] \tag{B.32}$$

where L_3 and L_4 are the lengths given on Fig. V-3, P_p is the pressure in the pressurizer, ρ_0 the density and D_h is the hydraulic diameter. At steady state, the pressurizer does not exchange any mass or energy with the loop. As a result, the velocity u_p, defined in a previous section is equal to zero. This condition is important since it allows computing an analytical solution.

$$T_{pump}(x) = T_{sg}(x = 2L_1 + L_2) \tag{B.33}$$

$$P_{pump}(x) = P_{sg} + f\frac{\rho_0}{D_h}\left|u\right|u\left(2L_1 + L_2 - x\right) \text{ for } x \in [2L_1 + L_2; 2L_1 + L_2 + L_5] \tag{B.34}$$

$$P_{pump}(x) = P_{sg} - L_5 f_w\frac{\rho}{D_h}\left|u\right|u + \left(\rho g h - f_w\frac{\rho}{D_h}\left|u\right|u\right)\left(2L_1 + L_2 + L_5 - x\right) \text{ for } x \in [2L_1 + L_2 + L_5; 2L_1 + L_2 + L_6] \tag{B.35}$$

$$P_{pump}(x) = P_{sg} - \left(L_5 + L_6\right) f_w\frac{\rho}{D_h}\left|u\right|u + f\frac{\rho_0}{D_h}\left|u\right|u\left(2L_1 + L_2 + L_5 - x\right) \text{ for } x \in [2L_1 + L_2 + L_6; 2L_1 + 2L_2] \tag{B.36}$$

where L_5 and L_6 are lengths given on Fig. V-4. The temperature is constant in both horizontal legs of the loop. The pressure drop is due to the friction forces and the pump and varies linearly.

We notice that the temperature profiles along the core and the steam generator are function of the parameters l_{core} and l_{sg} respectively; these also depend on the velocity. If the velocity is high (forced convection), the term $\frac{x}{l_{core}}$ is small so that the exponential function can be simplified using a Taylor series expansion:

$$e^{-x} \approx 1 - x \tag{B.37}$$

As a result, in the case of forced convection, the temperature profile is linear. If the buoyancy forces dominate (natural convection), the velocity is smaller than in the previous case. The temperature profile will not be linear since the term $\frac{x}{l_{core}}$ is no longer small compared to one.

VITA

Marc Olivier Delchini received his master's degree in physics from The National Engineering School of Grenoble (France) in 2008. He entered the graduate program at Texas A&M University in January 2009 and received his Master of Science degree in May 2010. His research interests include flow models and computing science applied to fluid flows. Mr. Delchini may be reached at 06 rue du Moulin Pinault 45800 Saint Jean de Braye, France. His email is marco.delchini@gmail.com.

The typist for this thesis was Marc-Olivier Delchini.